IN THIS JOURNAL

Great Britain Journals Press

journalspress.com

Print ISSN: 2631-8474
Online ISSN: 2631-8482
DOI: 10.17472/LJER

London Journal of Engineering Research

Volume 25 | Issue 5 | Compilation 1.0

COMPILED IN UNITED KINGDOM

ENGLISH

London Journal of Engineering Research

Volume 25 | Issue 5 | Compilation 1.0

PUBLISHER

Great Britain Journals Press
1210th, Waterside Dr, Opposite Arlington Building, Theale, Reading
Phone:+444 0118 965 4033 Pin: RG7-4TY United Kingdom

SUBSCRIPTION

Frequency: Quarterly

Print subscription
$280USD for 1 year
$500USD for 2 year
(color copies including taxes and international shipping with TSA approved)
Find more details at https://journalspress.com/journals/subscription

ENVIRONMENT

Great Britain Journals Press is intended about Protecting the environment. This journal is printed using led free environmental friendly ink and acid–free papers that are 100% recyclable.

Great Britain Journals Press Headquaters

1210th, Waterside Dr,
Opposite Arlington
Building, Theale, Reading
Phone:+444 0118 965 4033
Pin: RG7-4TY
United Kingdom

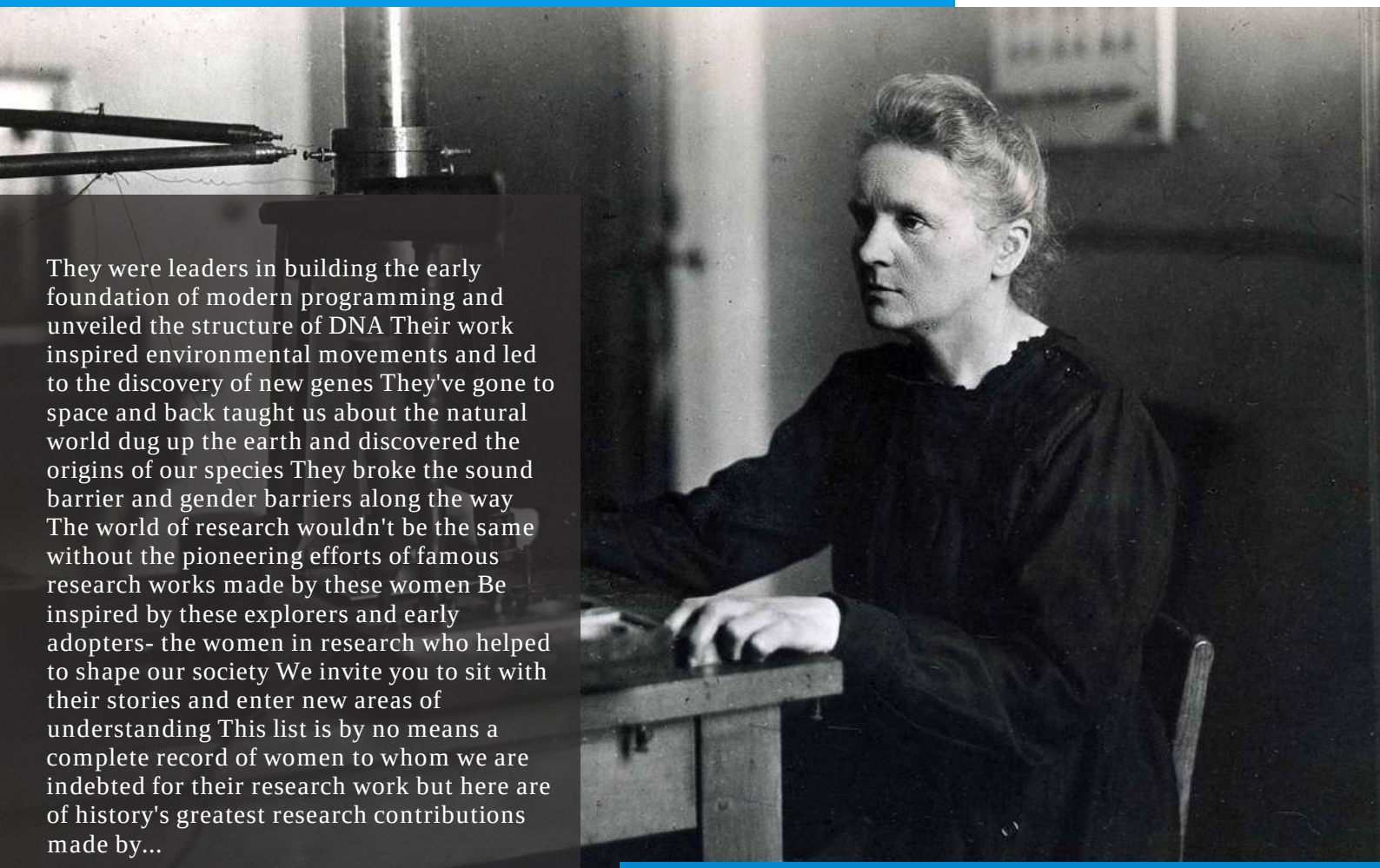

They were leaders in building the early foundation of modern programming and unveiled the structure of DNA Their work inspired environmental movements and led to the discovery of new genes They've gone to space and back taught us about the natural world dug up the earth and discovered the origins of our species They broke the sound barrier and gender barriers along the way The world of research wouldn't be the same without the pioneering efforts of famous research works made by these women Be inspired by these explorers and early adopters- the women in research who helped to shape our society We invite you to sit with their stories and enter new areas of understanding This list is by no means a complete record of women to whom we are indebted for their research work but here are of history's greatest research contributions made by...

Read complete here:
https://goo.gl/1vQ3lS

Women In Research

Computing in the cloud!

Cloud Computing is computing as a Service and not just as a Product Under Cloud Computing...

Read complete here:
https://goo.gl/VvHC72

Writing great research...

Prepare yourself before you start Before you start writing your paper or you start reading other...

Read complete here:
https://goo.gl/np73jP

Journal Content
In this Issue

Great Britain Journals Press

Editorial Board

Curated board members

Dr. Rocío Maceiras

Associate Professor for Integrated Science,
Defense University Center, Spain Ph.D., Chemical
Engineering, University of Vigo, SPAIN

Dr. Rolando Salgado Estrada

Assistant Professor,
Faculty of Engineering, Campus of Veracruz,
Civil Engineering Department, Ph D.,
Degree, University of Minho, Portugal

Dr. Abbas Moustafa

Department of Civil Engineering,
Associate Professor, Minia University, Egypt, Ph.D
Earthquake Engineering and Structural Safety,
Indian Institute of Science

Dr. Wael Salah

Faculty of Engineering,
Multimedia University Jalan Multimedia,
Cyberjaya, Selangor, Malaysia, Ph.D, Electrical and
Electronic Engineering, Power Electronics and Devices,
University Sians Malaysia

Prof. Baoping Cai

Associate Professor,
China University of Petroleum,
Ph.D Mechanical and Electronic Engineering,
China

Dr. Kao-Shing Hwang

Electrical Engineering Dept.,
Nationalsun-Yat-sen University Ph.D.,
Electrical Engineering and Computer Science,
Taiwan

Dr. Mu-Chun Su

Electronics Engineering,
National Chiao Tung University, Taiwan,
Ph.D. Degrees in Electrical Engineering,
University of Maryland, College Park

Nagy I. Elkalashy

Electrical Engineering Department,
Faculty of Engineering,
Minoufiya University, Egypt

Dr. Vitoantonio Bevilacqua

Department of Electrical and Information
Engineering Ph.D., Electrical Engineering
Polytechnic of Bari, Italy

Prof. Qingjun Liu

Professor, Zhejiang University, Ph.D.,
Biomedical Engineering,
Zhejiang University, China

Research papers and articles

Volume 25 | Issue 5 | Compilation 1.0

CFD Investigation of Turbulence Behaviour in Grooved Divergent Rocket Nozzles using the k-ε Model

Dieu-Donne Talla Elbazar Wandaogo, Christian John Etwire & Douglas Kwasi Boah

C. K. Tedam University of Technology and Applied Sciences & Bolgatanga Technical University

ABSTRACT

The adiabatic gas expansion in the divergent rocket area generally results in the generation of thrust required for propulsion by providing an environment where the gas molecules speed rapidly out the nozzle exit after traversing the nozzle area. This study investigates the impact of wall grooving in the divergent section of rocket nozzles on turbulence characteristics and flow performance using Computational Fluid Dynamics (CFD). Employing the Finite Volume Method (FVM) and the k– ε turbulence model in ANSYS Fluent, the study compares a conventional nozzle and a grooved counterpart under identical boundary conditions. Key parameters analyzed include Turbulent Kinetic Energy (TKE), Turbulent Eddy Dissipation (TED), and velocity profiles. Results reveal that while the grooved nozzle slightly reduces axial velocity, it significantly enhances turbulence dissipation and flow stability by suppressing lateral velocity fluctuations. Enhanced TED and uniform TKE distribution suggest improved mixing and thermal energy control, making grooved nozzles a promising modification for advanced propulsion systems.

Keywords: computational fluid dynamics, turbulence, divergent nozzle grooving, rocket nozzle, flow field.

Classification: DCC Code: TL565

Language: English

Great Britain Journals Press

LJP Copyright ID: 392951
Print ISSN: 2631-8474
Online ISSN: 2631-8482

London Journal of Engineering Research

Volume 25 | Issue 5 | Compilation 1.0

CFD Investigation of Turbulence Behaviour in Grooved Divergent Rocket Nozzles using the k-ε Model

Dieu-Donne Talla Elbazar Wandaogo[α], Christian John Etwire[σ] & Douglas Kwasi Boah[ρ]

ABSTRACT

The adiabatic gas expansion in the divergent rocket area generally results in the generation of thrust required for propulsion by providing an environment where the gas molecules speed rapidly out the nozzle exit after traversing the nozzle area. This study investigates the impact of wall grooving in the divergent section of rocket nozzles on turbulence characteristics and flow performance using Computational Fluid Dynamics (CFD). Employing the Finite Volume Method (FVM) and the k– ε turbulence model in ANSYS Fluent, the study compares a conventional nozzle and a grooved counterpart under identical boundary conditions. Key parameters analyzed include Turbulent Kinetic Energy (TKE), Turbulent Eddy Dissipation (TED), and velocity profiles. Results reveal that while the grooved nozzle slightly reduces axial velocity, it significantly enhances turbulence dissipation and flow stability by suppressing lateral velocity fluctuations. Enhanced TED and uniform TKE distribution suggest improved mixing and thermal energy control, making grooved nozzles a promising modification for advanced propulsion systems.

Keywords: computational fluid dynamics, turbulence, divergent nozzle grooving, rocket nozzle, flow field.

Author α: Bolgatanga Technical University, Department of Mechanical Engineering. C.K. Tedam University of Technology and Applied Sciences. School of Mathematical Sciences, Department of Mathematics.
σ: C.K. Tedam University of Technology and Applied Sciences. School of Mathematical Sciences. Department of Mathematics.
ρ: C.K. Tedam University of Technology and Applied Sciences. School of Mathematical Sciences. Department of Mathematics.

Nomenclature

a	Local speed of sound
P_o	Stagnation (total) pressure
P	Static pressure
γ	Specific Heat Capacity of fluid
h	Enthalpy
$\dot{q}$	Mass flow rate of fluid mass
$\overline{\rho}$	Mean flow density
$\overline{V}$	Mean flow velocity
$\overline{V}$	Velocity Vector
$\overline{V}_{yt}$	Flow velocity along upper wall boundary
$\overline{V}_{yb}$	Flow velocity along bottom wall boundary
l	Periodic distance / lenght scale
P_c	Constant relating to pressure
L	Lenght

London Journal of Engineering Research

$P\hat{}$	Modified pressure
$\bar{U}_i$	Mean turbulence velocity
U_i'	Fluctuating turbulence velocity
u_i	Instantaneous turbulence
k	Kinetic energy
P_ϵ	Rate of production of turbulence dissipation due to shear velocity
μ_t	Turbulent dynamic viscosity
ϵ	Turbulence Dissipation
$S_\epsilon, \sigma_\epsilon$	Source term due to dissipation and Prandtl number for turbulence dissipation
I, U, Re	Turbulence intensity, Internal velocity magnitude and Reynolds number respectively
ϕ	Viscous dissipation term
k	Thermal conductivity

I. INTRODUCTION

The convergent-divergent nozzle is mainly responsible in governing the performance and efficiency of a rocket engine or other systems incorporating "De-Laval" nozzle designs. High-pressure, High temperature adiabatic expulsion of exhaust gases out the nozzle exit from the combustion chamber get converted into reduced-temperature, reduced-pressure and high kinetic energy leading to high thrust generation required for propulsion. One of the important factors influencing this phenomenon is turbulence which significantly affects the characteristics of the fluid flow through the nozzle especially within the expansion region of the nozzle. Performance could either be impacted either positively or negatively by the phenomenon of turbulence depending on its management.

The interaction that occurs between the walls and flow of fluid in a rocket engine, the evolution of exhaust gases, velocity and pressure gradients all lead to the phenomenon of turbulence. Complex turbulent structures such as eddies, vortices and shock waves are some of the results of supersonic high energy flows. These features critically impact the flow pressure distribution, transfer of thermal energy, momentum among other turbulence features which critically influence the nozzle efficiency and performance [1]. Potential thrust loses not better controlled is capable of resulting in viscous energy dissipation from the random, chaotic turbulence due to high speed flows [2].

The main goal in the design of rocket engines is to have the adiabatic expanding gases be as efficient as possible whiles decreasing losses stemming from the phenomenon of turbulence and subsequent flow separation. Turbulence could lead to the exacerbation of flow separation where the boundary layer moves away or separates from the nozzle wall especially in the divergent nozzle section. As a result of the latter, shock waves result leading to decreased thrust efficiency, presence of unsteady fluid flow and decreased rocket stability [3]. This necessitates controlling or mitigating turbulence especially in this nozzle section in an attempt to obtain optimal performance in operational range.

Exploration of various techniques by studies in order to manage the phenomenon of tolerance in rocket engines have looked at the surface modification of nozzle walls. While surface grooving has shown to enhance aerodynamic performance in the field of aerospace engineering and in the internal combustion engine, its influence in rocket engines is not widely hence beckons further studies [4]. Grooving is also capable of influencing the intensity of turbulence either by enhancing or reducing some flow structures per their orientation or structure.

The study of the effect of wall surface modification on turbulence is made possible by the utilization of Computational Fluid Dynamics (CFD) Tool by solving the governing equations of fluid flow (Navier Stokes equations) and carrying out flow simulation which is capable of giving the behaviour and evolution of the fluid flow in the nozzle and over structures. Various turbulence models can be utilized such as $k-\epsilon$,$k-\omega$, Reynolds Averaged navier-Stokes (RANS), Large eddy Simulation to mention but a few to capture the complex behaviour of turbulence phenomenon [5]. Advancement of CFD has made it an indispensable tool capable of modelling and simulating highly intricate fluid flow phenomena with high accuracy.

Research has shown that problems resulting from the evolution of turbulence in the expanding nozzle section can be decreased through the redesigning of the surface wall boundary of the nozzle. For example, [3] shown that the variation in the geometry of the nozzle such as the incorporation of nozzle ramps and contours are capable of reducing the boundary flow separation and hence bringing about stability in the flow by reducing the turbulence. In the same analogy grooving nozzle surfaces has the potential to reduce the commencement of the separation of the boundary layer resulting to a more efficient nozzle fluid flow. Further investigation is however required on the effects on overall thrust efficiency and thermal heat transfer.

To add to the effects of flow separation, turbulence also has a critical role playing in the thermal heat properties and management of rocket engines. Due to the increased energetic turbulent flows, the rate of convective thermal transfer which can lead to elevated temperatures around the region of occurrence. This elevation in thermal load can result in increased material failure or degradation and hence the need for turbulence regulation and as such thermal heat management. [6] mentioned that there was a need to check the heat transfer since it plays a crucial role not only in performance optimization, but also in maintaining the structural integrity of the nozzle and rocket as a whole from increased thermal stresses.

This study aims to assess the effects divergent grooving has on the flow turbulence of a rocket utilizing Computational fluid Dynamics analysis. By comparing conventional (ungrooved) and grooved nozzle designs, insights into varying nozzle turbulent flow performance can be assessed.

Comprehending the effects of turbulence within a rocket nozzle plays a very critical in engine performance and as such further study and research is required to be able to utilise how surface modification can be exploited in improving the output rocket performance. This study hence seeks to also contribute to growing data and knowledge on how a rocket engine performs through the use of Computational Fluid Dynamics techniques.

II. REVIEW OF LITERATURE

Turbulence creates complex and chaotic flow characteristics and patterns which tend to make it into quiet a challenging phenomenon to study. [2] mentioned that eddies and vortices are capable of bringing about viscous dissipation of energy within the fluid resulting in reduced efficiency if not mitigated adequately.

A phenomenon intimately related to turbulence is Flow separation which is very critical in rocket nozzle design and performance. The detachment of the flow boundary layer from the nozzle wall results in unsteady flow behaviour and subsequent decrease and degradation in thrust. Turbulence and flow separation are major concerns in supersonic nozzle flows. When boundary layers detach under adverse pressure gradients, shock structures and unsteady flow can degrade thrust and nozzle efficiency [3].

Surface grooves have shown promise in delaying flow separation and enhancing wall-bound turbulence dissipation in turbomachinery and aerodynamic applications [7;8]. However, their effect in high-speed rocket nozzle flow—especially on turbulence kinetic energy (TKE) and eddy dissipation (TED)—remains largely unexplored.

CFD studies have shown that nozzle shape and wall modifications can significantly affect internal

flow structures and turbulence–shock interactions [9;10]. Groove-enhanced designs may promote mixing, suppress unsteady shocks, and control wall heat transfer—all desirable for propulsion applications.

This study aims to extend these findings by applying the k–ε model in ANSYS Fluent to compare grooved and conventional nozzles under identical flow conditions, evaluating the effect on turbulence parameters and flow stability.

III. METHODOLOGY

3.1 Governing Equations and Conditions of Flow

At high velocities within a nozzle on channel, turbulence tends to manifest especially when flow encounters wall structure geometries and hence making the nature of structural geometries playing a critical role in turbulent phenomena. The aim here is to simulate turbulence within a conventional and grooved rocket engine using $k-\epsilon$ model which is composed of a two transport equations: Kinetic energy (K) and turbulent dissipation rate (ϵ) in CFD (Analysis System) which is capable of turbulent flow characteristics capturing through the nozzle.

3.2 Computational Domain and Meshing

The Ansys Design modeler was utilized in capturing the dimensions) of both Conventional and Grooved convergent-Divergent rocket nozzles as shown in Figures 1 and 2 with the respective dimension given in Table 1. The symmetry of the rocket nozzle was conical and simulation of 2D axial flow domains. The latter leads to reduced computational power usage and the number of meshing elements required. The meshing and the domain (adiabatic) under computational consideration are shown in Fig. 4 and 5. The fundamental nozzle dimensional considerations are the combustion chamber, converging nozzle and the throat diameter linking the divergent nozzle section. These dimensions are provided in Table 1. The grooved nozzle geometry has four circumferential grooves along the wall of the divergent nozzle. The flow velocity is considered zero radially and hence perpendicular flow towards the walls are assumed no-slip. High resolution, structured and double precision mesh was generated to adequately capture turbulence effects over grooved regions along the nozzle wall. The resulting mesh obtained are seen in Figures 2 and 4. The boundary conditions for the flow inlet, outlet and wall along with the respective pressures as given in Tables 2, 3 and 4.

Table 1: Details of Design Parameters for Grooved and Conventional Rocket Engine

Nozzle Section	Grooved Nozzle Dimension, mm	Conventional Nozzle Dimension, mm
Convergent Nozzle Angle, A10	19.385^o	19.385^o
Divergent Nozzle Angle, A32	13.282^o	13.282^o
Combustion Chamber lenght, L2	10.829	10.829
Combustion Chamber width, L3	16.244	16.244
Rocket Engine Length, L5	75.000	75.000
Divergent Nozzle Axial lenght, L18	42.554	42.554
Nozzle Exist Radius, L6	19.474	19.474
Throat radius, L7	9.4303	9.430
Groove width, L19 = L26 = L27 = L29	5.9763	0.000
Groove depth	0.55991	0.000

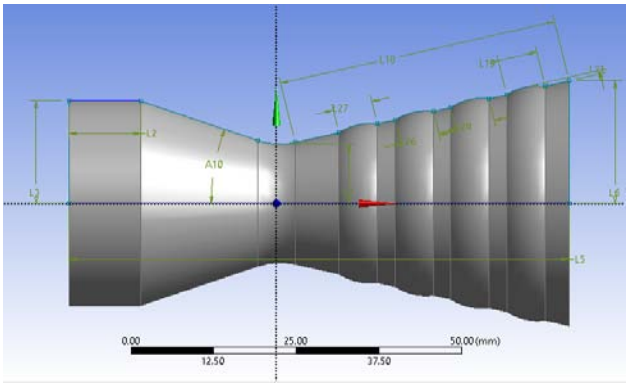

Figure 1: Grooved rocket nozzle

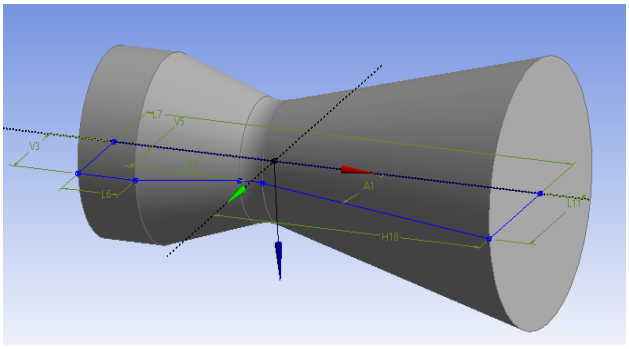

Figure 2: Conventional Rocket Nozzle Schematic Geometry

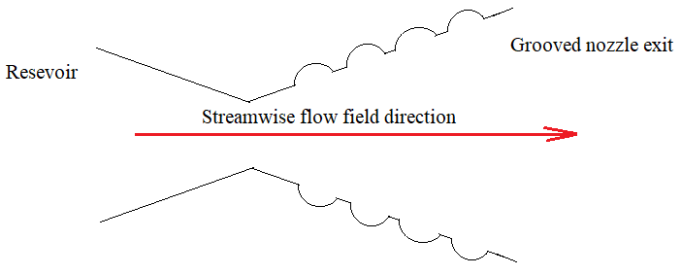

Figure 3: Geometry of flow problem

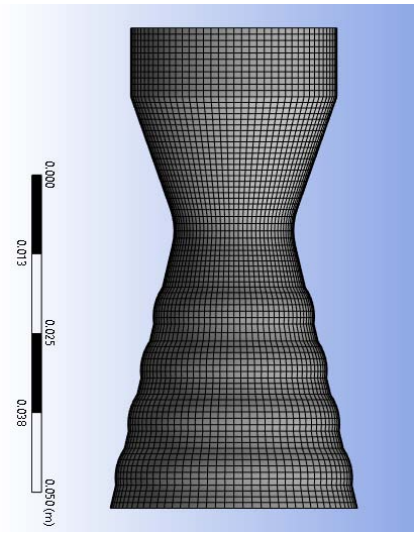

Figure 4: Grooved rocket nozzle mesh

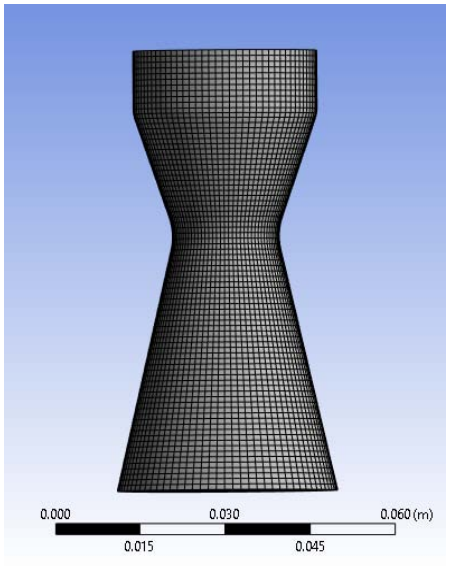

Figure 5: Conventional nozzle mesh

3.3 Selection of k–ε Turbulence Model

The Standard $k-\epsilon$ model is chosen with the CFD solver which solves the kinetic energy (k) and its accompanying dissipation rate (ϵ) along with the model constants C_1,C_2,μ,C_μ

3.4 Solver Settings

A Solver based on density and suitable for high-speed compressible fluid flow capturing is utilized. Steady state time is set for the steady simulation of rocket nozzle flow.

3.5 Turbulence Modeling

Enhanced wall function or scalable wall function is selected for the implementation of wall treatment which also depends on the resolution of the mesh near the wall boundaries.

3.6 Residual Plots

These were important in identifying the nature of the computational solution based on iteration. The local imbalances of conserved variables present in each respective control volume are measured by the residuals. The solver used for this study is Analysis System Fluent and it solves the modified governing flow equations due to wall modification and boundary conditions.

IV. RESULT GENERATION

Convergence is arrived at the end of the iterative solutions, The respective plots and data contours are obtained describing the flow velocity and turbulence through the Convergent-Divergent rocket nozzles.

4.1 Analysis Procedure and Boundary Conditions

Table 2: CFD Preprocessing Setup

Procedure	Setup
Problem Setup: General-Solver	Type: Density based
Models	Energy :On
Materials	fluid: Air($25^{o}C$)
Boundary Conditions	Inlet: Pressure Inlet, Gauge Total Pressure (Pa): , Outlet: Pressure Outlet, Gauge Pressure
Reference Values	Compute from: Inlet, Reference Zone: Solid body surface
Monitors	Create walls, Print to console and plot
Initialization	Standard initialization, Compute from inlet
Solution	Solution controls- Courant number= 5, Run calculation: Enter iteration number and initiate.

Table 3: Convergent divergent boundary conditions

Boundary	Type
Inlet	Gauge Total Pressure 90[kPa]
Static Temperature	288.1K
Outlet	Gauge Pressure
Wall	wall Function
Surface	Interior Surface

Table 4: Material Library

Quantity	Description
Material	Air at $25^{o}C$
Option	Pure substance
Thermodynamic State	Gas
Density	1.185 kgm^{-3}
Molar Mass	28.96 $kgkmol^{-1}$
Specific Heat Capacity	$1.0044*10^{03}j.kg^{-1}k^{-1}$
Reference fluid Temperature	25 C
Thermal Conductivity	$2.61*1002Wm-1K-1$
Thermal Expansivity	$3.35*10^{-3}K^{-1}$

4.2 Mathematical Formulations

4.2.1 Conservation of Mass

This is also often referred to as the "Continuity Equation". It states that mass in a system cannot be created nor destroyed but can only move from one place to the other. Having a control volume and applying the Gauss's divergence theorem in integral form, Eq. 4.1 is obtained representing the continuity equation [11].

$$\frac{\partial}{\partial t}\oint_{\Omega}\rho d\Omega + \oint_{\Omega}\nabla\bullet(\rho\mathbf{V})d\Omega = 0 \qquad (4.1)$$

$\Omega,\rho,\nabla\bullet$ stand for the control volume, density and the divergence of vector $\nabla\bullet \mathrm{V} = ui+vj+wk$ with u, v, and w are the velocity components in the i, j and k directions.

4.2.2 Boundary Conditions

- Inlet

  $u \quad = 1, v = 0$
- Outlet

  $\frac{\partial u}{\partial x} = 0$

  $\frac{\partial v}{\partial y} = 0$
- Wall

  No-Slip and isothemal boundary conditions (u=v=0; θ = 0)

  $u \quad = 0$

  $v \quad \neq 0$ only on flat wall

  $w \quad \phi = u,v,\bar{P}$ or θ

  Reference frame = Absolute Gauge total pressure = 101325 Pa Supersonic / Initial gauge pressure = 100000 Pa Temperature = 300 K

  Reference Values

  Density = 1.165636 kg/m^3 Enthalpy = 301020 J/kg Ratio of Specific heat = 1.4

From the Continuity equation in divergence form below, a fluid particle moving from left to right under the due to pressure gradient within the fluid stream in order to satisfy the law of the conservation of mass, diverges whenever it impacts a bod, reconstitutes behind the body and hence maintaining the total fluid mass at the right side of the fluid path. The above statement is represented by the equation below:

The fluid velocity vector, $\bar{V}$ = (u,v) for flow in two-dimensions and x and y are the streamwise and normal coordinates respectively.

$$\nabla\cdot\bar{V} = 0 \qquad (4.2)$$

Bounding the fluid flow field equations are two non-permeating and non-slip boundaries/wall identical in shape and area represented by

$\bar{V}_{yt} = \bar{V}_{yb}$ where $\bar{V}_{yt}$ is the velocity experienced by the upper wall boundary and $\bar{V}_{yb}$ is the velocity of the lower boundary. Beyond the upper and lower walls or boundaries, it is assumed that flow is zero for normal flow through a duct as seen below.

$$Ytx \leq y \geq Ybx$$

(y_t) and (y_b) stands for the upper and lower wall shape of the convergent divergent nozzle shape.

$$\bar{V}ytx = \bar{V}ybx = 0$$

4.2.3 Periodic Conditionality of Flow Through Repeating Grooves

4.2.3.1 Wall Condition

With regards to the flow through a hollow duct with periodically repeating structures or grooves, the mathematically repeating or changing cross-sectional area is represented as below [12].

$$Y_{tx} = Y_t(x+l) = Y_t(x+2l) = Y_t(x+3l) = Y_t(x+4l) \qquad (4.3)$$

$$Y_{bx} = Y_b(x+l) = Y_b(x+2l) = Y_b(x+3l) = Y_b(x+4l) \qquad (4.4)$$

l, x and (x+l) are the period of change which is a characteristic dimension, horizontal positions present within the grooves.

4.2.3.2 Evolution of Fluid Flow Cyclic/Periodic Velocity, Pressure and Temperature

Let the two-dimensional flow velocity be $u(x,y) and v(x,y)$.

$$u(x,y) = u(x + l,y) = u(x + 2l,y) = u(x + 3l,y) = u(x + 4l,y) \tag{4.5}$$

$$v(x,y) = v(x + l,y) = v(x + 2l,y) = v(x + 3l,y) = v(x + 4l,y) \tag{4.6}$$

4.2.3.3 Governing Flow Equations and Boundary Condition

The fundamental governing equations of flow are the Navier-Stokes equations and when incorporated with the periodic fully developed flow and the heat transfer equation:

4.2.3.4 Mass Conservation Equation

$$\frac{\partial \rho}{\partial t} + \nabla.u = 0 \tag{4.7}$$

4.2.3.5 Momentum Equation

$$\frac{\partial u}{\partial t} = u.\nabla u = -\frac{\hat{P}}{\rho} + \nu\nabla^2 u + \frac{\beta}{\rho} \tag{4.8}$$

Where $\hat{P}$, ρ and μ are the reduced pressure due to flow over grooves, fluid density and dynamic flow viscosity respectively. the modified pressure and actual flow pressure is given by [14].

$$P_a(x,y) = -\beta x + \hat{P}(x,y) \tag{4.9}$$

β and P_a stands for the linear constant for pressure for a definite mass flow rate and the actual or corrected pressure respectively.

$$\begin{aligned} p(x,y) - p(x + l,y) &= p(x + l,y - p(x + 2l,y) \\ &= p(x + 2l,y) - p(x + 3l,y) = \\ p(x + 3l,y &- p(x + 4l,y) \end{aligned} \tag{4.10}$$

The above relation in Eq. (4.10) shows that the flow pressure decreases axially along the nozzle with each successive groove presence or occurrence. This differential pressure also accounts for the fluid mass flow from right to left of the flow wall boundary along the horizontal x-direction.

4.3 Governing Equation For Turbulent Flow

The component of the transport equation coupled with the compressible turbulence flow field equation are:

4.3.1 Continuity Equation

$$\frac{\partial \rho}{\partial t} + \nabla.(\rho U) \tag{4.11}$$

4.3.1 Mass Transport

$$\frac{\partial \rho\phi}{\partial t} + \Delta.(\rho U\phi) \tag{4.12}$$

where ϕ standing for the type of fluid component, air.

$$\frac{\partial \rho U}{\partial t} + \nabla.(\rho U \otimes U) = \nabla\hat{p} + \nabla.[\mu_{eff}(\nabla U + (\nabla U)^T)] \tag{4.13}$$

Above equation is eddy viscosity based with $\hat{P}$ being the modified pressure.

4.4 Two-Equation Turbulence Models: k-ϵ of RANS

[13] proposed a computational fluid dynamics two-part equation Eq. (4.14) and (4.15)to help account and describe the turbulence in a fluid flow. These are the Turbulence Kinetic Energy (TKE) and the Turbulence Dissipation Rate (TDR) or the Turbulence Eddy Dissipation (TED).

4.4.1 Turbulence kinetic Energy

$$\frac{\partial(\rho k)}{\partial t} + \frac{\partial(\rho U_i k)}{\partial x_i} = \frac{\partial}{\partial x_j}\left[\left(\mu + \frac{\mu_t}{\sigma_k}\right)\frac{\partial k}{\partial x_j}\right] + p_k + P_b - \rho\epsilon + S_k \tag{4.14}$$

p_k = Production of turbulence kinetic energy (TKE)due to mean velocity shear

P_b = Production of TKE due to buoyancy

S_k = User defined source, σ_k = Turbulence Prandtl number for k.

4.4.2 Turbulence Eddy Dissipation

$$\frac{\partial(\rho\epsilon)}{\partial t}+\frac{\partial(\rho U_i\epsilon)}{\partial x_i}=\frac{\partial}{\partial x_j}\left[\left(\mu+\frac{\mu_t}{\sigma_\epsilon}\right)\frac{\partial\epsilon}{\partial x_j}\right]+C_1\frac{\epsilon}{k}(P_k+C_3P_b)-C_2\rho\frac{\epsilon}{k}+S_\epsilon \tag{4.15}$$

C_1,C_2,C_3,C_μ = model coefficients varying in $K-\epsilon$ turbulence models S_ϵ = User-defined source
σ_ϵ = Turbulent Prandtl number for ϵ

V. EVOLUTION OF TURBULENCE WITHIN A CONVERGENT-DIVERGENT NOZZLE

High Kinetic energy gas entities are generated in a rocket nozzle when high pressure and high temperature gases undergo rapid expansion adiabatically. It is assumed that all thermal energy is used to propel the molecular gaseous species. Figure 6 shows a directly proportional relationship existing between TKE and TED in a nozzle with grooves. As flow speeds towards the exit nozzle area where the presence of wall structural geometries are dominant, there is an increased "fluid-structure" interaction leading to increased TKE and its subsequent dissipation (TED).

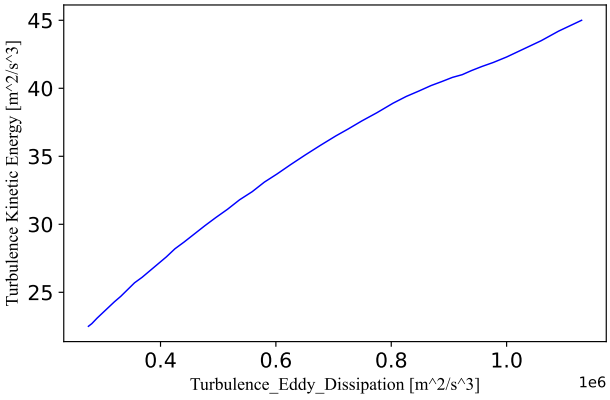

Figure 6: Turbulence Kinetic Energy versus Turbulence Eddy Dissipation

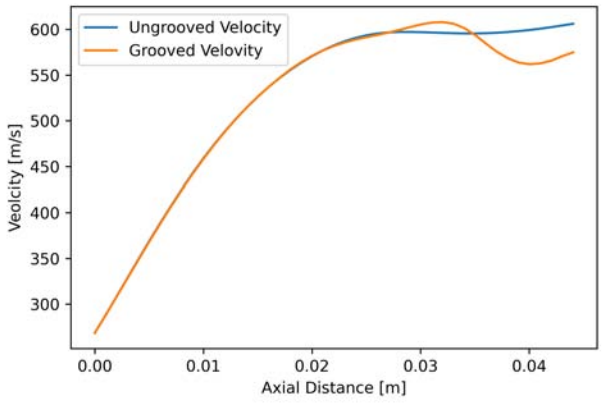

Figure 7: Comparative axial velocities for conventional and grooved nozzles

It is depicted in a comparison plot in Figure 7 that both conventional and grooved rocket nozzles have similar axial-velocity flow pattern but this is observed to change streamwisely after the nozzle-throat area some velocity perturbation is noticed for both nozzle with that of the grooved nozzle experiencing major velocity change but finally increasing. The major deferring flow feature is observed to occur about a fourth (1/4) of the axial distance aft the exit nozzle area.

Figures 8 and 9 show the behaviour of TED and TKE respectively for both conventional and grooved nozzles axially in their respective nozzles. In both figures, there is a direct performance correlation for both TKE and TED suggesting that irrespective of the nozzle type, both TKE and TED will be directly proportional. In Figure 8, TED for both nozzle types have relatively wide range whereas looking at TKE for both nozzles, the range much closer but for the combustion chamber and towards the exit nozzle area.

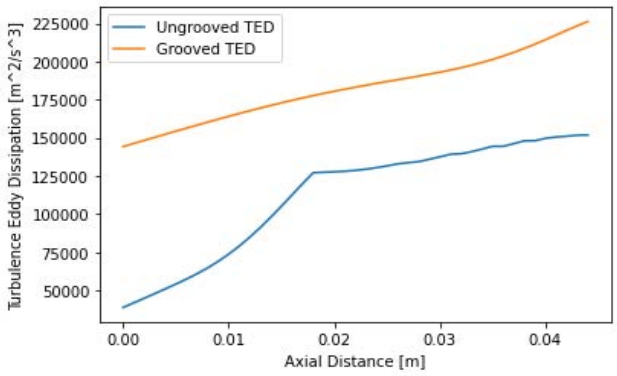

Figure 8: Axial comparison between conventional(ungrooved) and grooved nozzle Turbulence Eddy Dissipation

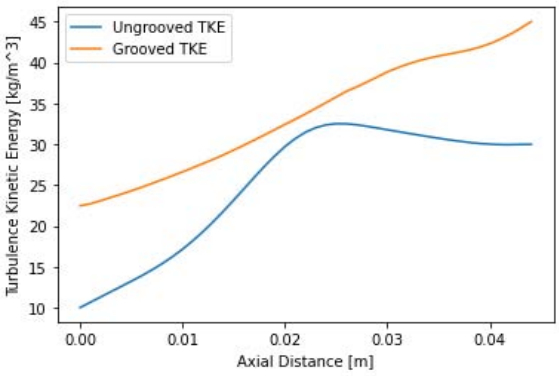

Figure 9: Axial comparison between conventional(ungrooved) and grooved nozzle Turbulence Kinetic Energy

In Figures 10 and 11, the effect of velocity on turbulence on a conventional and grooved convergent-divergent nozzle geometries is presented. Figure 10 shows the effect of TED for both nozzle geometries where it is seen that the general rate of occurrence is relatively wide but tapers to as both increase gradually with increase in axial velocity with some perturbation between $550m/s$ to $600m/s$. In the case of the effect of axial-velocity on TKE from Figure 11, the rate range of occurrence is much closer as compare to that of TED, there is also a gradual increase with increase in velocity but perturbation only begins to manifest when velocity is nearly $600m/s$.

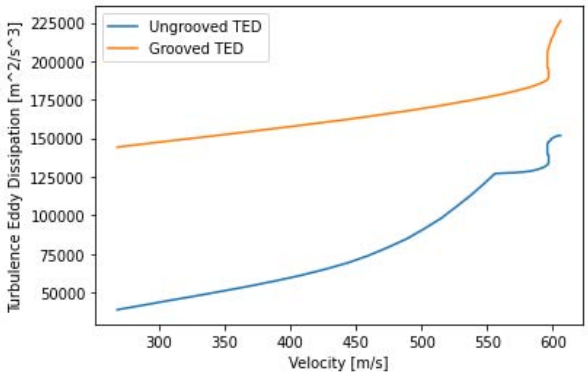

Figure 10: Comparison of the effect of velocity on Turbulence Eddy Dissipation for conventional(ungrooved) and grooved Nozzles

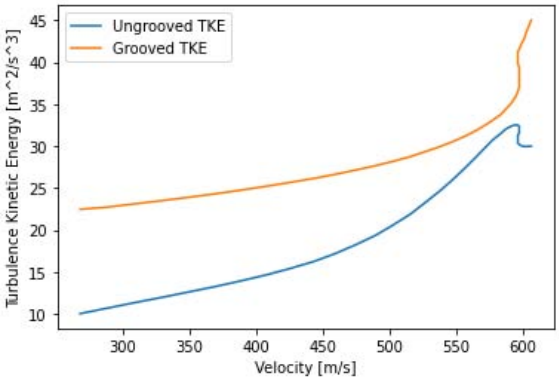

Figure 11: Comparison of the effect of velocity on Turbulence Kinetic Energy for conventional(ungrooved) and grooved nozzles

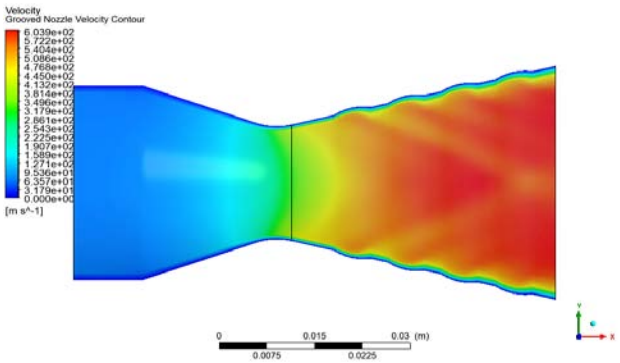

Figure 12: Grooved nozzle velocity contours

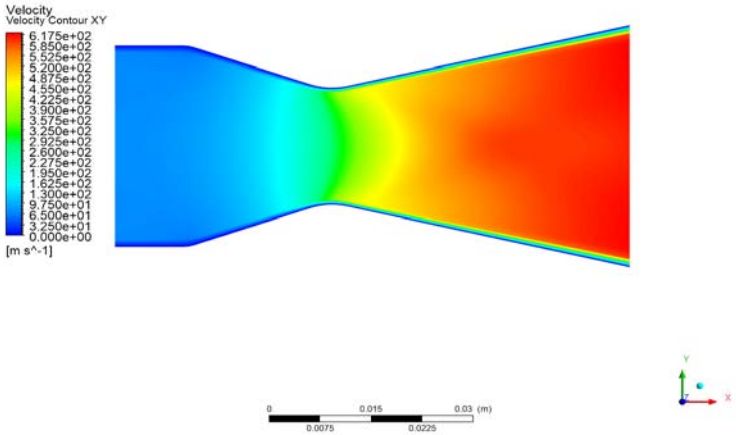

Figure 13: Conventional nozzle velocity contours

Figures (12 and 13) show the contours of velocity increasing axially within the nozzles of the grooved and conventional nozzle geometries respectively. However, it is further observed in Figure 12 that, due to the grooves on the wall surface of the grooved nozzle, there is the formation of backward facing patterns which are absent in the conventional nozzle. The "diamond" patterns can be attributed to the interaction between the geometry of the groove and the gas flow within and out of them.

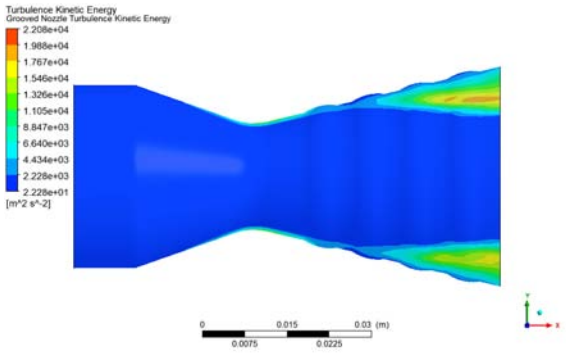

Figure 14: Contours of grooved nozzle Turbulence Kinetic Energy

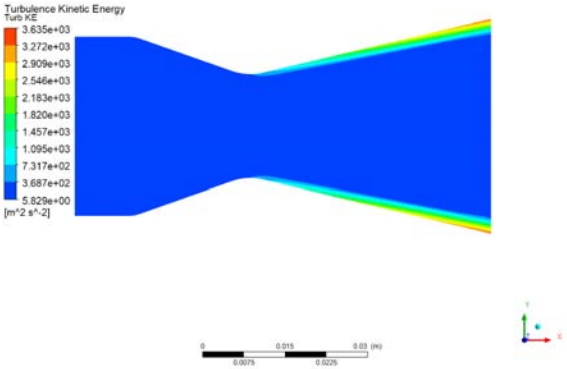

Figure 15: Contours of conventional nozzle Turbulence Eddy Dissipation

Figures 14 and 15 show the TKE contours occurring within the grooved and conventional nozzles respectively and it is observed that, TKE for the grooved nozzle is much more pronounced with a maximum energy $1.767 * 10^4$ to $1.988 * 10^4$ represented a orange contour between the last nozzle groove and the nozzle exit area. The energy range present within the grooved nozzle was between $2.228*10^1$ to $1.988*10^4$. Present in the conventional nozzle was an energy range between $5.829 * 10$ to $3.272 * 10^3$ with a greater energy seen around the region nearest to the divergent nozzle area. It is how ever noticed that, the commencement of TKE was delayed within the grooved nozzle whiles within the conventional nozzle, the occurrence of TKE was much more pronounced immediately aft the nozzle throat area.

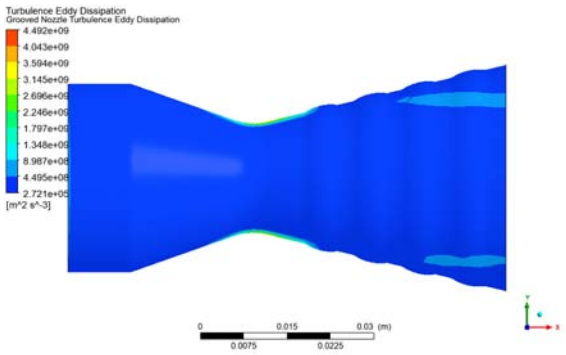

Figure 16: Contours of grooved nozzle Turbulence Eddy Dissipation

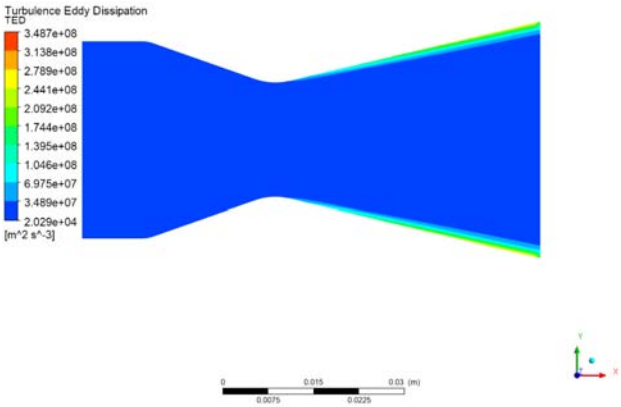

Figure 17: Contours of conventional nozzle Turbulence Eddy Dissipation

Figures 16 and 17 are depictions of the contours for the TED in occurring within the grooved and conventional nozzle area geometries. The dissipation energy observed in the grooved nozzle was between $2.721 * 10^5$ to $8.987 * 10^8$ with the greater part dominant around the latter nozzle exit wall area.

Table 5: Variable Range Information for Conventional and Grooved Rocket Nozzle

Parameter	Min (Conv.)	Max (Conv.)	Min–Max (Grooved)	Comments
U-Vel (ms^{-1})	146	2070	152–1650	Reduced maximum axial velocity ensures smoother flow acceleration and minimizes shock formation risks.
V-Vel (ms^{-1})	616	638	382–385	Narrower lateral velocity range indicates improved flow stability and reduced side thrust forces.
TKE (m^2/s^2)	3.910	33400	22.3–22100	Higher minimum and lower peak TKE promotes efficient, stable turbulence without energy waste.
TED (m^2/s^3)	14400	164000	272000–449000	Lower TED peak values ensure more uniform energy dissipation and smoother combustion stability.

In Table 5 are the minimum and maximum Variable Range summary values for the velocity, TKE and TED respectively. It is observed that, The grooved nozzle has a lower maximum TKE and a greater maximum TED respectively. A higher TED denotes that the system is capable of dissipation TKE as they form or occur as Compared to that of their ungrooved or conventional counterpart. U-velocity for the conventional nozzle showed lower minimum and maximum velocities as compared with that of the grooved nozzle, however the V-velocities for the conventional nozzle showed higher values as compared with the grooved V-velocity values.

U-Velocity (Axial): The grooved nozzle has a slightly lower maximum axial velocity (1.65×10^3) compared to the conventional nozzle (2.07×10^3), indicating potential energy loss or flow resistance due to groove structures.

V-Velocity (Lateral): Grooved nozzles exhibit reduced lateral velocity fluctuations, with a smaller range (-3.82×10^2 to 3.85×10^2) than conventional nozzles. This suggests a more stable flow with less swirl or cross-stream mixing.

Turbulent Kinetic Energy (TKE): Although the maximum TKE in grooved nozzles is lower, the minimum is higher than in the conventional nozzle. This may reflect a more uniform but less intense turbulence field.

Turbulent Energy Dissipation (TED): The grooved nozzle shows higher minimum TED (2.72×10^5) and lower maximum TED (4.49×10^9), indicating a more consistent rate of turbulence dissipation, which may enhance controlled mixing without extreme energy losses.

Overall Insight: Grooved nozzles provide a potentially more stable and uniform turbulent flow field, which could be beneficial in reducing flow separation or structural vibrations, albeit at the expense of slightly reduced flow velocities and turbulence intensities.

VI. TURBULENT KINETIC ENERGY (TKE)

Table 6: Comparison of TKE Across Studies

Source	TKE (m^2/s^2)
Grooved Nozzle (Present Study)	22.3
Conventional Nozzle (Present Study)	3.91
[15]	12.5
[16]	12.0
[17]	11.29
[18]	11.5

The grooved nozzle shows the highest TKE, indicating superior turbulence generation and energy transfer. From Table 6, TKE in the grooved nozzle is nearly double the highest reported in literature. This confirms the superior turbulence generation, which is essential for vortex breakup, flame holding, and improved heat transfer.

VII. TURBULENT DISSIPATION ENERGY (TDE)

Table 7: Comparison of TED Across Studies

Source	TDE (m^2/s^3)
Grooved Nozzle (Present Study)	272000
Conventional Nozzle (Present Study)	14400
[15]	0.015
[16]	0.041
[17]	0.013
[18]	0.013

TDE for the grooved nozzle is significantly higher, ensuring effective breakdown of turbulent structures and uniform energy distribution. Table 7 hence shows that TDE from the grooved nozzle in orders of magnitude is higher than both conventional and prior studies. This indicates more energy is dissipated through turbulence, leading to efficient mixing and reduced coherent structures. It also enhances thermal energy distribution downstream.

7.1 Observed Improved Grooved Divergent Rocket Nozzle Performance

7.1.1 Enhanced Shear and Mixing (High TKE & v-Momentum)

- The grooved nozzle shows a turbulent kinetic energy (TKE) of 22.3 m^2s^{-3}, significantly greater than the conventional nozzle's TKE of 3.91 m^2s^{-3}.
- The v-momentum is 1442 kg·m/s compared to just 78 kg·m/s for the conventional nozzle.
- These values indicate superior radial thrust and turbulence—critical for fuel-air mixing, energy distribution, and flame stability in combustion systems such as rocket engines.

7.1.2 Greater Energy Dissipation (TDE)

- The grooved nozzle exhibits a total dissipation energy (TDE) of 272000 m^2s^{-3}, much higher than the conventional nozzle's TDE of 14400 m^2s^{-3}.
- This higher dissipation helps reduce large turbulent structures, promoting finer-scale mixing and more efficient combustion.

7.1.3 Directionally Efficient Flow

- Although the grooved nozzle has a lower v-velocity (383 m/s) compared to the conventional nozzle (616 m/s), it achieves higher directional control through greater radial momentum.
- This suggests the grooved design effectively redirects flow energy into turbulence and mixing, rather than just raw lateral velocity.

7.1.4 Balanced Axial Velocity

- The u-velocity for the grooved nozzle is 152 m/s, slightly higher than the conventional nozzle's 146 m/s.
- This indicates no compromise in axial thrust while achieving significantly higher radial mixing and turbulence.

The grooved nozzle offers clear advantages in turbulent mixing, momentum control, and energy dissipation. These qualities are critical for applications requiring improved combustion efficiency, flame stability, and heat transfer performance. The performance metrics (TKE, TDE, v-momentum) make a compelling case for favoring the grooved nozzle design over conventional configurations since the grooved nozzle demonstrates superior performance in

nearly all critical parameters when compared to the conventional nozzle and referenced studies. Its high TKE, exceptional radial momentum, and elevated TDE establish it as the most effective design for enhancing mixing, combustion stability, and thermal efficiency. Therefore, the grooved nozzle is highly recommended for advanced propulsion and energy systems.

VIII. CONCLUSION

The comparative CFD analysis of grooved and conventional rocket nozzles reveals that wall grooving has a profound effect on turbulent flow behavior. The grooved nozzle demonstrates enhanced turbulence energy dissipation and more uniform TKE distribution, resulting in better flow stability and reduced risk of flow separation. Although there is a modest reduction in maximum axial velocity, the overall aerodynamic performance benefits from improved radial mixing and momentum control. These findings underscore the potential of wall-surface modifications, particularly grooving, as an effective strategy for optimizing rocket nozzle performance in high-speed propulsion applications. Future work could explore groove pattern optimization and three-dimensional effects for further performance enhancement.

Limitations and Future Work

This study focuses on two-dimensional, steady-state simulations using the standard k–ε turbulence model. While informative, this approach may not capture three-dimensional or transient effects such as swirl or pulsation. Future research should include 3D simulations, alternative turbulence models (e.g., k–ω SST or LES), and experimental validation to further substantiate the findings.

Data Availability Statement: Data are contained within the article

REFERENCES

1. Pope, S. B. (2000). Turbulent Flows. Cambridge university Press.
2. Deere, K. (2003). Summary of Fluidic Thrust Vectoring Research at NASA Langley Research Center. In Proceedings of The 21st AIAA APPlied Aerodynamics Conference, Orlando, FL, USA, 23-26 June 2003; P.3800. DOI:10.2514/6.2003-3800.
3. Vladislav Emelyanov, Konstantin Volkov, Mikhail Yakovchuk. (2022). Unsteady Flow Simulation Of Compressible Turbulent Flow In Dual-Bell Nozzle With Movement Of Extensible Section Fromm Its Initial To Working Position. Acta Astronautica. 194, 514-523. ISSN 0094-5765. https://doi.org/10.1016/j.actaastro.2021.10.007.
4. Bejan, A. (2013). Convection Heat Transfer (4th ed.). Wiley. ISBN: 9780470900376 DOI:10.1002/9781118671627.ch12.
5. Jiyuan tu, Guan-Heng Yeoh and Chaoqun Liu. (2008). Computational Fluid Dynamics, A practical approach. third edition. https://doi.org/10.1016/B978-0-08-101127-0.00001-5.
6. Ali, A., Rodriguez, C., Neely A., Young, J. (2012). Combination of Fluidic Thrust modulation and vectoring in a 2D Nozzle. In Proceedings of the 48th AIAA/ASME/SAE/ASEE. Joint Propulsion Conference & Exhibit. Atlanta, GA, USA. P.3780. DOI:10.2514/6.2012-3780.
7. Deng, W., Zhang, R.R., Xu, G., Li, L.L., Tang, Q. and Xu, M. (2019). The Influences of the Nozzle Throat Length and the Orifice Grooving Degree on Internal Flow Field for a Multi-Entry Fan Nozzle Based on FLUENT4. Engineering. 11. 777-790. https://doi.org/10.4236/eng.2019.1111052.
8. Shi, N., Gu, Y., Wu, T., Zhou, Y., Wang, Y., Deng, S. (2023). An Optimized Pressure-Based Method for Thrust Vectoring Angle Estimation. Aerospace. 10(12), 978. https://doi.org/10.3390/aerospace10120978.
9. Guo, C., Wei, Z., Xie, K., Wang, N. (2017). Thrust Control By Fluidic Injection In Solid Rocket Motors. Journal of Propulsion and Power. 33, 815-829. DOI: 10.2514/1.B36264.
10. Anderson, J.D. (2017). Fundamentals of Aerodynamics, McGraw-Hill Education, New York.
11. Schmidt, D. P., et al. (2009). Riblet Surfaces For Turbulence Suppression in High-Speed Flows. Journal of Fluid Mechanics, 629(1), 273-299.

12. S. V. Patankar, C. H. Liu and E. M. Sparrow. (1977). Fully Developed Flow and Heat Transfer in Ducts Having Streamwise-Periodic Variations of Cross- Sectional Area. ASME Journal of Heat Transfer. 99 pp. 180-186. http://dx.doi.org/10.1115/1.3450666.
13. B.E. Launder, D.B. Spalding. (1974). The numerical computation of turbulent flows. Computer Methods in Applied Mechanics and Engineering. 3. SSN 0045-7825. https://doi.org/10.1016/0045-7825(74)90029-2.
14. Y. Wang, Y. Lin, Q. Eri and B. Kong. (2022). Flow and Thrust Characteristics of An Expansion-Deflection Dual-Bell Nozzle, Aerospace Science And Technology, 123.
15. Sharma, A., & Sinha, D. (2017). CFD Analysis of Supersonic Nozzle Flow Using Different Turbulence Models. *International Journal of Engineering Research and Applications*, 7(5), 38–43.
16. Wang, Y., & Zhao, X. (2020). Optimization of Rocket Nozzle Design for Enhanced Thrust Performance Using CFD. *AIAA Journal of Propulsion and Power*, 36(4), 623–633.
17. Yadav, P., & Singh, R. (2018). Numerical Analysis of Rocket Nozzle Flow at Various Mach Numbers. *International Journal of Fluid Dynamics*, 23, 59–69.
18. Martelli, F., et al. (2021). Numerical Analysis of Side-loads Reduction in a Sub-scale Dual-bell Rocket Nozzle. *Flow, Turbulence and Combustion*, 107(3), 789–812.

This page is intentionally left blank

Polyphenol-Rich Collas-Co™: A Study on Antioxidant Activity and Cellular Safety

Chanin Leksahakhun & Laichheang Yort

ABSTRACT

Polyphenols, known for their strong antioxidant properties, combat oxidative stress, enhance cell viability, and protect against free radical damage. These bioactive compounds hold immense potential for functional food and cosmetic innovations, supporting overall health and promoting skin resilience, offering exciting opportunities in nutraceutical and cosmetic product development. This study evaluates the bioactive properties and potential applications of Collas-Co™, a high-polyphenol ingredient with promising antioxidant activity. The total phenolic content (TPC) of Collas-Co™ was determined to be 58.05 ± 0.33 mg GAE/g. Its antioxidant capacity, assessed via ORAC assay, revealed a remarkably high scavenging activity of 15,221 ± 409 µmol TE/100g. Furthermore, the DPPH assay demonstrated superior radical scavenging activity, with Collas-Co™ achieving 85.67% inhibition at 2.5 mg/mL, outperforming gallic acid by approximately 15%. Cytotoxicity studies using primary human dermal fibroblasts indicated that Collas-Co™ exhibited dose-dependent effects. At lower concentrations (0.39 mg/mL), it enhanced cell viability to 112.94%, suggesting potential protective or stimulatory properties.

Keywords: polyphenol, antioxidant, cytotoxicity, cellular.

Classification: DCC Code: QD431

Language: English

Great Britain Journals Press

LJP Copyright ID: 392952
Print ISSN: 2631-8474
Online ISSN: 2631-8482

London Journal of Engineering Research

Volume 25 | Issue 5 | Compilation 1.0

Polyphenol-Rich Collas-Co™: A Study on Antioxidant Activity and Cellular Safety

Chanin Leksahakhun[α] & Laichheang Yort[σ]

ABSTRACT

Polyphenols, known for their strong antioxidant properties, combat oxidative stress, enhance cell viability, and protect against free radical damage. These bioactive compounds hold immense potential for functional food and cosmetic innovations, supporting overall health and promoting skin resilience, offering exciting opportunities in nutraceutical and cosmetic product development. This study evaluates the bioactive properties and potential applications of Collas-Co™, a high-polyphenol ingredient with promising antioxidant activity. The total phenolic content (TPC) of Collas-Co™ was determined to be 58.05 ± 0.33 mg GAE/g. Its antioxidant capacity, assessed via ORAC assay, revealed a remarkably high scavenging activity of 15,221 ± 409 µmol TE/100g. Furthermore, the DPPH assay demonstrated superior radical scavenging activity, with Collas-Co™ achieving 85.67% inhibition at 2.5 mg/mL, outperforming gallic acid by approximately 15%. Cytotoxicity studies using primary human dermal fibroblasts indicated that Collas-Co™ exhibited dose-dependent effects. At lower concentrations (0.39 mg/mL), it enhanced cell viability to 112.94%, suggesting potential protective or stimulatory properties. Moderate concentrations (0.78–6.25 mg/mL) showed tolerability, while higher concentrations (>12.50 mg/mL) resulted in cytotoxicity, with an IC50 of 50.50 ± 2.07 mg/mL. These findings highlight Collas-Co™ as a potent antioxidant with moderate cytotoxicity, suitable for functional foods and cosmetic applications.

Keywords: polyphenol, antioxidant, cytotoxicity, cellular.

Author α σ: Beyond Laboratory (Thailand) Co., Ltd. 555/121 B Avenue, Sukhapiban 5 road, Sai Mai, Bangkok, Thailand.

I. INTRODUCTION

The increasing global prevalence of oxidative stress-related conditions, such as cardiovascular diseases, neurodegenerative disorders, diabetes, and certain cancers, highlights the critical need for effective antioxidant strategies. Oxidative stress results from an imbalance between reactive oxygen species (ROS) production and the body's ability to neutralize these harmful molecules, leading to cellular damage, inflammation, and aging [1]. Polyphenols, a class of naturally occurring bioactive compounds, have garnered significant attention due to their potent antioxidant properties. These compounds act as free radical scavengers, protect cellular structures, and inhibit oxidative damage, making them valuable in addressing chronic diseases and promoting overall health [2-3].

Collas-Co™, a novel polyphenol-rich ingredient, has demonstrated exceptional potential for health applications due to its high total polyphenol content (TPC). Polyphenols are not only indicators of antioxidant potential but are also associated with cellular protective mechanisms that support skin health, delay aging, and mitigate oxidative damage. While TPC provides preliminary insights into bioactivity, comprehensive evaluations of antioxidant capacity and cellular safety are crucial to validate its efficacy and safety for human applications. Techniques such as the Oxygen Radical Absorbance Capacity (ORAC) and DPPH radical scavenging assays are widely regarded as robust methods to assess the radical-scavenging ability of antioxidants [4-5].

Furthermore, cytotoxicity studies are essential to determine the safety of polyphenol-rich ingredients, particularly when intended for nutraceuticals, functional foods, or cosmetics. Fibroblasts, key cellular components of the skin, play a crucial role in maintaining extracellular matrix integrity and repairing oxidative damage. Investigating the impact of Collas-Co™ on fibroblast viability provides valuable insights into its cytotoxicity profile, cellular safety, and potential for regenerative applications. This is particularly important as cellular health is directly linked to skin vitality and anti-aging benefits [6].

This study focuses on evaluating the antioxidant activity and cellular safety of Collas-Co™, with a specific emphasis on its polyphenol-rich composition and radical-scavenging efficacy. Additionally, a comparative analysis with gallic acid, a well-known antioxidant, highlights Collas-Co™'s relative effectiveness. The findings aim to establish Collas-Co™ as a safe, multifunctional ingredient suitable for addressing oxidative stress, promoting cellular health, and supporting its application in functional food, nutraceutical, and cosmetic industries.

II. MATERIALS AND METHODS

2.1 Materials

Collas-Co™ was procured from Beyond Laboratory (Thailand) Co., Ltd., Bangkok, Thailand, while all chemicals used in the analysis were of analytical reagent (AR) grade.

2.2 Total Polyphenol Content Analysis

The total polyphenol content (TPC) was modified according to Singleton [7].A 1000 ppm gallic acid solution was prepared by dissolving 0.25 g of gallic acid (Sigma–Aldrich, Seelze, Germany) in 1.5 mL of ethanol, followed by dilution to a final volume of 250 mL with deionized water. From this stock solution, standard solutions were prepared at concentrations of 10, 25, 50, 100, 200, and 250 ppm. Separately, 25 g of sodium carbonate (Sigma–Aldrich, Seelze, Germany) was dissolved in 100 mL of warmed deionized water, stirred until fully dissolved, filtered, and cooled to room temperature. Additional sodium carbonate was added incrementally to encourage crystallization; if crystallization did not occur, the solution was stored in a refrigerator for future use. For the Collas-Co™ solution, 1.00 g of sample was dissolved in 100 mL of boiling deionized water with stirring for approximately 10 minutes. The solution was filtered, and the residue was re-extracted with an additional 100 mL of boiling deionized water. The filtrates from both extractions were combined and diluted to a final volume of 250 mL in a volumetric flask.

For the assay, 0.5 mL of each gallic acid standard, sample solution, and a deionized water blank were transferred to separate tubes. To each tube, 4.3 mL of deionized water, 0.2 mL of Folin-Ciocalteu's phenol reagent, and 0.5 mL of saturated sodium carbonate were added sequentially. The mixture was vortexed, followed by the addition of another 4.3 mL of deionized water, and vortexed again. The tubes were incubated in the dark at room temperature for 45 minutes, and the absorbance was measured at 765 nm to determine phenolic content. TPC was calculated using the equation of the standard curve: $y = 0.0048x + 0.0111$, with a coefficient of determination ($R^2 = 0.9986$). Results were expressed as mg GAE/g (milligrams of gallic acid equivalents per gram).

2.3 Antioxidant Activities Analysis

2.3.1 Oxygen Radical Absorbance Capacity (ORAC)

The ORAC value was measured following the procedure outlined by Kuti [8], with slight modifications. The reaction mixture consisted of 1.7 mL of 75 mM phosphate buffer (pH 7.0), 100 µL of R-phycoerythrin (R-PE, 3.4 mg/L), 100 µL of 320 mM 2,2′-azobis(2-amidinopropane) dihydrochloride (AAPH), and 100 µL of the extract. Phosphate buffer served as the blank, and Trolox was used as the standard. The total volume of the mixture was 2 mL, placed in a 10 mm fluorometer cuvette, and preincubated at 37 °C for 15 minutes. The reaction was initiated by adding AAPH, and fluorescence was recorded every 5 minutes at 570 nm (emission) and 540 nm (excitation) using a fluorometer (Sequoia-Turner

model 450, USA), until fluorescence decreased to less than 5% of the initial value. Each sample was tested in triplicate.

The ORAC values, expressed as Trolox equivalents (TE) per 100 gram, were calculated based on the area under the fluorescence decay curve. ORAC was determined using the standard curve equation C= K × A, where K = 203.65 µ/mL, A = absorbance, and the coefficient of determination was R^2 = 0.9993.

2.3.2 DPPH Radical Scavenging Activity

DPPH radical scavenging assay was conducted following the procedure outlined by Sadeer &Siddeega [9-10]. The DPPH (2,2-diphenyl-1-picrylhydrazyl) radical scavenging assay was conducted to assess the antioxidant activity of Collas-Co™ and the standard gallic acid. A 0.1 mM DPPH solution was prepared in methanol, while test samples (Collas-Co™) were diluted to final concentrations of 1.0, 0.5, 0.25, 0.125, 0.063, 0.031, 0.016, and 0.008 mg/mL using 0.5 M acetic acid. Similarly, gallic acid was prepared at concentrations ranging from 10 to 0.078 mg/mL in methanol. In a 96-well plate, 100 µL of DPPH solution was added to each well, followed by 100 µL of the sample or standard solution. Methanol and DPPH alone served as control (A0) and blank (A2), respectively. The plate was incubated at room temperature for 20 minutes in the dark to allow the reaction between the antioxidants and DPPH radicals. Absorbance was measured at 517 nm using a microplate reader. The percentage of DPPH radical inhibition was calculated using the formula: Inhibition (%) = $[1-(A_1-A_2)/A_0] \times 100$

where

A_0 = absorbance of control (without of sample)

A_1 = absorbance of test (Sample+DPPH)

A_2 = absorbance of DPPH

The IC_{50} value, indicating the concentration required to inhibit 50% of DPPH radicals, was determined from the dose-response curve plotting inhibition percentage against concentration. This approach effectively quantified the antioxidant potential of the samples.

2.4 Cytotoxicity Test On Primary Human Dermal Fibroblast By WST-1 Assay

2.4.1 Cell Cultivation

Human dermal fibroblast cells (HDFn) were cultured in Dulbecco's Modified Eagle Medium (DMEM) supplemented with 10% Fetal Bovine Serum (FBS) and 1% Antibiotic/Antimycotic solution. Cells were seeded at an initial density of 2×10^5 cells per well in a 96-well culture plate and incubated at 37°C in a CO_2 incubator with 5% CO_2 for 24 hours. After incubation, cell growth and morphology were observed under an inverted microscope to ensure optimal conditions for subsequent testing or assays.

2.4.2 Cytotoxicity Test

Cytotoxicity test assay was conducted following the procedure outlined by Kamiloglu& Yin [11-12]. Sample solutions were incubated with cells in a 96-well culture plate, with the test sample Collas-Co™ applied at various concentrations. The negative control group consisted of cell culture media (DMEM), while the positive control group used 0.10% sodium dodecyl sulfate (SDS). Cells were incubated at 37°C with 5% CO_2 in a cell culture incubator for 24 hours.

After incubation, the cells were washed with phosphate-buffered saline (PBS), and 10 µL of WST-1 solution was added to 100 µL of DMEM in each well. The plates were re-incubated under the same conditions for an additional 30 minutes, after which absorbance was measured at a wavelength of 450 nm. The resulting color intensity correlated with the number of viable cells.

The absorbance values (OD) were used to calculate the percentage of cell viability using the equation:

Cell viability (%) = (Absorbance (OD) of cells in the test group x 100)/Absorbance (OD) of cells in the negative control group)

This method provided a quantitative assessment of cell viability under different treatment conditions.

III. RESULT AND DISCUSSION

3.1 Total Polyphenol Content

The total phenolic content (TPC) of Collas-Co™ is summarized in Table 1. The TPC of Collas-Co™ was determined to be 58.05 ± 0.33 mg GAE/g. This value indicates that Collas-Co™ contains significantly higher TPC compared to medium and dark roasted coffee from Colombia, which contain 24.28 mg GAE/g and 21.41 mg GAE/g, respectively, as well as strawberry, which contains 22.37 mg GAE/g [13-14].

Although the relatively high TPC of Collas-Co™ suggests the presence of active compounds, this measure alone provides only preliminary insights into its biochemical potential. Phenolic content is a useful indicator of bioactive components; however, further investigation into its antioxidant activity is crucial to assess the functional benefits of Collas-Co™. Antioxidant activity, such as that measured through ORAC and DPPH provides a more comprehensive understanding of the compound's potential to neutralize oxidative stress and its applicability in various health-promoting contexts.

Table 1: Total polyphenol content and ORAC scavenging activity of Collas-Co™

Sample	Total Polyphenol Content (mg GAE/g)	ORAC Scavenging Activity (µmol TE/100g)
Collas-Co™	58.05 ± 0.33	15221 ± 409

** GAE: Galic acid equivalent, TE: Trolox equivalent*

3.2 Antioxidant Activities

3.2.1 Oxygen Radical Absorbance Capacity (Orac)

The Oxygen Radical Absorbance Capacity (ORAC) assay is a widely used method to evaluate the antioxidant capacity of foods and other substances. This assay measures the scavenging activity of antioxidants against free radicals, particularly peroxyl radicals, by assessing the inhibition of oxidation of a fluorescent probe such as fluorescein. The ORAC method provides insight into the radical scavenging potential of compounds, using parameters such as the area under the fluorescein decay curve (AUC) and lag time to quantify antioxidant capacity effectively [15]. Furthermore, the proper selection of calibrator compounds is critical to ensure unbiased estimation of antioxidant activity, as highlighted by Carvalho [15].

For *Collas-Co™*, the ORAC scavenging activity was determined to be *15,221 ± 409 µmol TE/100g* (Table 1). This value represents a remarkably high antioxidant activity when compared to several well-known antioxidant-rich foods, including elderberries (10,655 µmol TE/100g), red apple (7,781 µmol TE/100g), pomegranate (5,923 µmol TE/100g), and plum (5,700 µmol TE/100g) [16].

These findings highlight the significant potential of Collas-Co™ to combat oxidative stress through its high radical scavenging capacity. This exceptional antioxidant performance suggests its promising application in nutraceuticals and functional foods, where oxidative stress inhibition is essential for health benefits. Further studies exploring the specific bioactive compounds responsible for this activity could provide a deeper understanding of its mechanism and potential health applications.

3.2.2 DPPH Radical Scavenging Activity

The DPPH (2,2-diphenyl-1-picrylhydrazyl) assay is a commonly used method to evaluate antioxidant capacity [5]. It measures the ability of antioxidants to neutralize the stable DPPH radical, which has a deep violet color. When antioxidants donate electrons or hydrogen atoms, the DPPH radical is reduced to a pale-yellow or colorless compound, resulting in a measurable decrease in absorbance at 517 nm. This assay is valued for its simplicity, speed, and cost-effectiveness, making it widely used for screening antioxidant properties in natural products, foods, and supplements.

The DPPH radical scavenging activity of Gallic acid and Collas-Co™ is presented in Fig. 1. Gallic

acid exhibits moderate scavenging activity at lower concentrations, which increases steadily with higher concentrations. In contrast, Collas-Co™ shows relatively lower scavenging activity at lower concentrations but surpasses Gallic acid at higher concentrations. Notably, at the highest concentration (2.5 mg/mL), Collas-Co™ achieves a superior DPPH radical scavenging activity of 85.67%, outperforming Gallic acid, which achieves 70.66%, by approximately 15%.

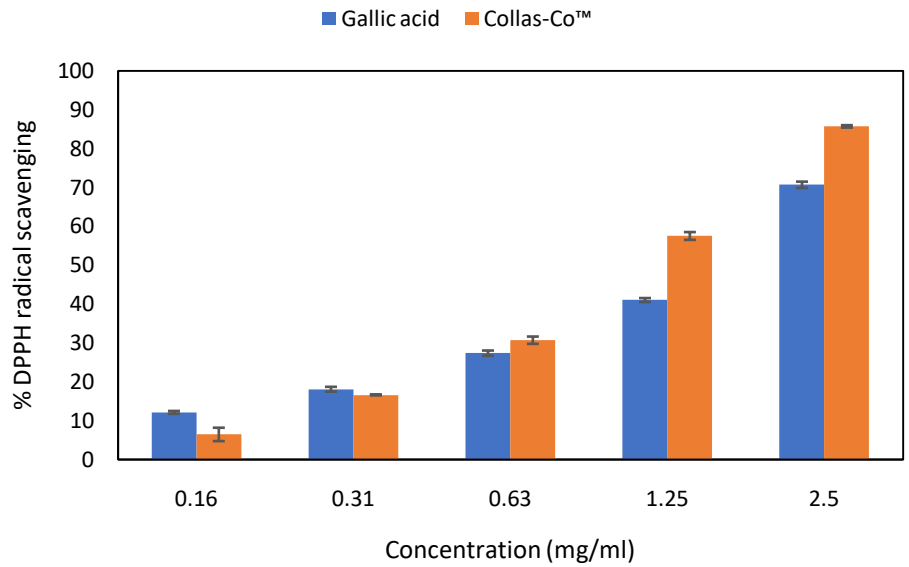

Fig. 1: DPPH radical scavenging activity of gallic acid and Collas-Co™

The IC50 value, a critical parameter for assessing the potency of a compound in inhibiting a specific biological or chemical process [17], is shown in Fig. 2 for the DPPH radical scavenging activity of Collas-Co™ and Gallic acid. The IC_{50} of Collas-Co™ is lower than that of Gallic acid, indicating that Collas-Co™ is approximately 21.8% more effective in achieving 50% inhibition of DPPH radical activity.

Although Gallic acid demonstrates higher radical scavenging activity at lower concentrations (as shown in Fig. 1), Collas-Co™ surpasses it in overall potency by requiring a lower concentration to reach the critical threshold of 50% inhibition. This highlights Collas-Co™ as a more efficient scavenger at moderate to high concentrations. This result suggests that Collas-Co™ is better suited for applications requiring high efficacy at lower doses, making it ideal for products with concentration constraints. In contrast, Gallic acid remains a reliable and effective antioxidant option for formulations where higher concentrations are feasible and practical [18].

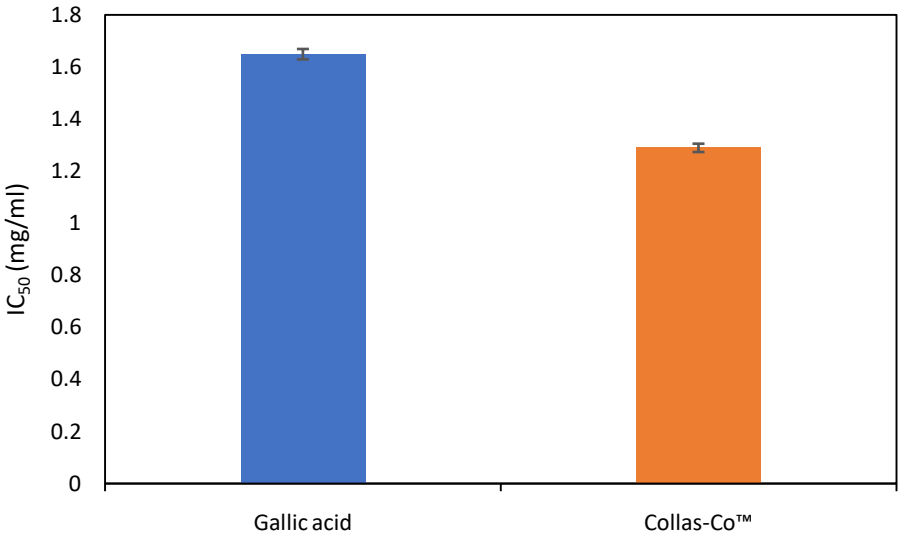

Fig. 2: Inhibition DPPH of gallic acid and Collas-Co™

3.3 Cytotoxicity Screening of Collas-Co™ on Primary Human Dermal Fibroblast

Fig. 3 presents an image of cultured human fibroblast cells observed under an inverted microscope. The inverted microscope offers a clear visualization of cell structures, allowing detailed assessment of cell health and morphology during experimental studies. Fibroblast cells exhibit a characteristic spindle shape with elongated, stretched-out bodies and occasional branching processes.

In the image, the cells grow in a monolayer formation, aligning parallel to one another, a hallmark of fibroblast behavior in vitro after 24 hours of culture. The parallel alignment and density of the cells suggest a confluent or semi-confluent layer, indicative of active growth and division under well-maintained culture conditions. The observed morphology and arrangement confirm that the fibroblast cells are healthy and thriving in optimal culture conditions, ensuring reliability for further experimental applications. This observation aligns with findings by D'Urso [6] in this study, which highlights the importance of mechanical and physical factors in maintaining fibroblast morphology and function under in vitro conditions.

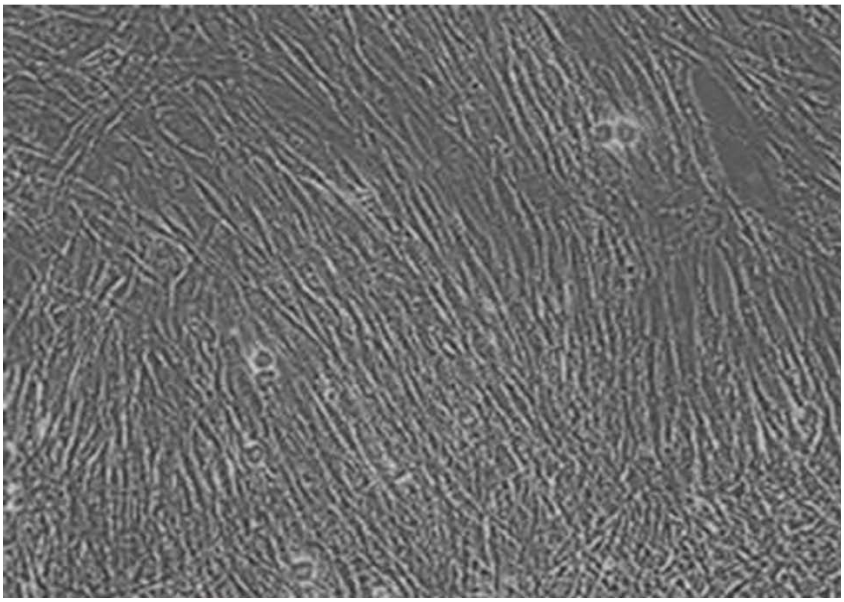

Fig. 3: Primary human Dermal Fibroblasts normal after aging for 24 hours

The cell viability of fibroblasts after 24 hours of exposure to various concentrations of Collas-Co™ and SDS is summarized in Table 2. Untreated fibroblasts in the control group maintained 100% viability, providing a baseline for comparison. Exposure to 0.1% Sodium Dodecyl Sulfate (SDS), a known cytotoxic agent, drastically reduced cell viability to 45.05 ± 2.29%, confirming its harmful effects. In contrast, Collas-Co™ showed a dose-dependent impact on fibroblast viability. At a low concentration of 0.39 mg/mL, cell viability increased to 112.94 ± 2.20%, indicating a protective or stimulatory effect. Moderate concentrations (0.78–6.25 mg/mL) led to a gradual decline in viability, although cells remained viable, suggesting tolerability within this range. At higher concentrations (12.50–50.00 mg/mL), cell viability significantly decreased, reaching 50.63 ± 1.68% at the highest concentration, highlighting dose-dependent cytotoxicity.

The IC_{50} value for Collas-Co™, calculated as 50.50 ± 2.07 mg/mL, indicates the concentration required to reduce cell viability by 50%. This relatively high IC_{50} reflects moderate cytotoxicity, with stimulatory effects at lower concentrations and tolerability at moderate doses. The IC_{50} value, a critical parameter for assessing the potency of compounds, represents the concentration needed to inhibit 50% of cell growth, with lower values indicating higher cytotoxicity. For comparison, a study revealed that the triple antibiotic paste (TAP)–cysteamine combination exhibited the lowest cytotoxicity (highest IC_{50} of 12.86%), indicating greater safety compared to other combinations such as chlorhexidine–cysteamine, which demonstrated the highest cytotoxicity with the lowest IC_{50} of 0.12% [19].

Table 2: Cell viability of fibroblast after aging for 24 hours

Sample	Concentration	% Cell viability
Control	-	100.00 ± 0.00
SDS	0.1%	45.05 ± 2.29
Collas-Co™ (mg/ml)	0.39	112.94 ± 2.20
	0.78	98.85 ± 2.62
	1.56	93.31 ± 2.42
	3.13	83.19 ± 2.70
	6.25	75.56 ± 1.64
	12.50	69.49 ± 2.77
	25.00	61.38 ± 0.24
	50.00	50.63 ± 1.68
IC_{50} (mg/ml)		50.50 ± 2.07

** SDS: Sodium Dodecyl Sulfate use for positive control*

IV. CONCLUSION

The study on Collas-Co™ reveals several significant findings regarding its bioactive properties and potential applications. First, it demonstrates a remarkably high total polyphenol content (TPC) and antioxidant activity, surpassing various foods renowned for their health benefits. This highlights its capability to combat oxidative stress effectively. Second, the DPPH assay confirms that Collas-Co™ has superior radical scavenging activity at higher concentrations compared to gallic acid, emphasizing its efficacy in antioxidant applications. Third, cytotoxicity testing on fibroblast cells shows that Collas-Co™ enhances cell viability at lower concentrations and exhibits tolerable effects at moderate doses, suggesting potential for safe use in nutraceuticals or cosmetic formulations. Additionally, its IC50 value indicates moderate cytotoxicity, with stimulatory effects at appropriate dosages. Overall, Collas-Co™ demonstrates significant promise as an ingredient in health-promoting

products, warranting further exploration of its specific bioactive compounds and mechanisms.

ACKNOWLEDGE

The authors would like to express their sincere gratitude to the Central Laboratory (Thailand) Co., Ltd., for their invaluable support in providing advanced analytical services. Additionally, we extend our heartfelt thanks to the Expert Center of Innovative Herbal Products, Thailand Institute of Scientific and Technological Research (TISTR), for their expert assistance and state-of-the-art facilities that greatly contributed to the success of this research. Your contributions have been integral to achieving the objectives of this study.

REFERENCE

1. I. Liguori, G. Russo, F. Curcio, et al., "Oxidative stress, aging, and diseases," *Clinical Interventions in Aging*, vol. 13, pp. 757–772, 2018.
2. K. B. Pandey and S. I. Rizvi, "Plant polyphenols as dietary antioxidants in human health and disease," *Oxidative Medicine and Cellular Longevity*, vol. 2, no. 5, pp. 270–278, 2009.
3. A. Scalbert, C. Manach, C. Morand, et al., "Dietary polyphenols and the prevention of diseases," *Critical Reviews in Food Science and Nutrition*, vol. 45, no. 4, pp. 287–306, 2005.
4. R. L. Prior, X. Wu, and K. Schaich, "Standardized methods for the determination of antioxidant capacity and phenolics in foods and dietary supplements," *Journal of Agricultural and Food Chemistry*, vol. 53, no. 10, pp. 4290–4302, 2005.
5. M. Yamauchi, Y. Kitamura, H. Nagano, et al., "DPPH measurements and structure-activity relationship studies on the antioxidant capacity of phenols," *Antioxidants*, vol. 13, no. 3, p. 309, 2024.
6. M. D'Urso and N. A. Kurniawan, "Mechanical and physical regulation of fibroblast–myofibroblast transition: From cellular mechanoresponse to tissue pathology," *Frontiers in Bioengineering and Biotechnology*, vol. 8, p. 609653, 2020.
7. V. L. Singleton and J. A. J. Rossi, "Colorimetry of total phenolics with phosphomolybdic-phosphotungstic acid reagents," *Am. J. Enol. Vitic.*, vol. 16, pp. 144–158, 1965.
8. J. O. Kuti and H. B. Konuru, "Antioxidant capacity and phenolic content in leaf extracts of tree spinach (Cnidoscolus spp.)," *J. Agric. Food Chem.*, vol. 52, no. 1, pp. 117–121, 2004.
9. N. B. Sadeer, D. Montesano, M. F. Mahomoodally, et al., "The versatility of antioxidant assays in food science and safety—Chemistry, applications, strengths, and limitations," *Antioxidants*, vol. 9, p. 709, 2020.
10. A. Siddeega, N. M. AlKehayez, H. A. Abu-Hiamed, et al., "Mode of action and determination of antioxidant activity in the dietary sources: An overview," *Saudi Journal of Biological Sciences*, vol. 28, pp. 1633–1644, 2021.
11. S. Kamiloglu, G. Sari, T. Ozdal, and E. Capanoglu, "Guidelines for cell viability assays," *Food Frontiers*, vol. 1, no. 3, pp. 332–349, 2020.
12. L. M. Yin, Y. Wei, Y. Wang, et al., "Long term and standard incubations of WST-1 reagent reflect the same inhibitory trend of cell viability in rat airway smooth muscle cells," *International Journal of Medical Sciences*, vol. 10, no. 1, pp. 68–72, 2013.
13. M. D. S. Ribeiro, N. Sebastià, A. Montoro, et al., "Strawberry (Fragaria× Ananassa) and Kiwifruit (Actinidia Deliciosa) extracts as potential radioprotective agents: Relation to their phytochemical composition and antioxidant capacity," *Applied Sciences*, vol. 13, no. 15, p. 8996, 2023.
14. L. Alnsour, R. Issa, S. Awwad, et al., "Quantification of total phenols and antioxidants in coffee samples of different origins and evaluation of the effect of degree of roasting on their levels," *Molecules*, vol. 27, no. 5, p. 1591, 2022.
15. J. R. B. Carvalho, A. N. Meireles, S. S. Marques, et al., "Exploiting kinetic features of ORAC assay for evaluation of radical scavenging capacity," *Antioxidants*, vol. 12, no. 2, p. 505, 2023.

16. S. Bhagwat, D. B. Haytowitz, and J. M. Holden, "USDA database for the oxygen radical absorbance capacity (ORAC) of selected foods," *American Institute for Cancer Research Launch Conference*, Washington, DC, pp. 1–2, Nov. 2007.
17. F. Martinez-Morales, A. J. Alonso-Castro, J. R. Zapata-Morales, et al., "Use of standardized units for a correct interpretation of IC50 values obtained from the inhibition of the DPPH radical by natural antioxidants," *Chemical Papers*, vol. 74, pp. 3325–3334, 2020.
18. M. Hadidi, R. Liñán-Atero, M. Tarahi, et al., "The potential health benefits of gallic acid: therapeutic and food applications," *Antioxidants*, vol. 13, no. 8, p. 1001, 2024.
19. E. A. M. A. E. Mohamed, A. H. Mahran, S. H. E. Ashry, et al., "The cytotoxic effect of cysteamine and its combinations with various endodontic intracanal medications on fibroblast cells: in vitro study," *Bulletin of the National Research Centre*, vol. 47, no. 1, p. 74, 2023.

This page is intentionally left blank

A Novel Detail-Enhancement Method for Industrial Digital Radiography via Gaussian-Free Multiscale Laplacian Adaptive Fusion

Guancheng Lu, Zhen Dong, Jin Wei, Guiqing Li, Jihua Guan & Wei Wei

Guangxi University

ABSTRACT

This study introduces a concise framework for detail enhancement in industrial digital radiography based on the mathematical integration of logarithmic transformation and multiscale Laplacian analysis. The proposed method utilizes multiscale adaptive pixel-level fusion with hyperbolic tangent-based coefficients to preserve microscale defects while enhancing subtle features throughout the dynamic range. Quantitative evaluations of diverse industrial welds, including ship plates, boilers, and oil pipelines, demonstrated substantial improvements. In oil pipeline weld inspections, the Peak Signal-to-Noise Ratio of the method based on Histogram Equalization increased by 133.82%, whereas the Structural Similarity Index Measure and Spatial Frequency metrics exhibited gains of up to 127.27% and 85.81%, respectively. The framework's consistent, albeit moderate, performance gains over state-of-the-art deep learning methods across all benchmarks confirm its value not only as a robust and widely applicable tool but also as a superior preprocessing or integrated solution within nondestructive testing pipelines.

Keywords: digital radiography, multiscale analysis, pixel-level fusion, image detail enhancement, nondestructive testing.

Classification: FoR Code: 460205

Language: English

Great Britain Journals Press

LJP Copyright ID: 392953
Print ISSN: 2631-8474
Online ISSN: 2631-8482

London Journal of Engineering Research

Volume 25 | Issue 5 | Compilation 1.0

A Novel Detail-Enhancement Method for Industrial Digital Radiography via Gaussian-Free Multiscale Laplacian Adaptive Fusion

Guancheng Lu[α], Zhen Dong[σ], Jin Wei[ρ], Guiqing Li[ↀ], Jihua Guan[¥] & Wei Wei[§]

ABSTRACT

This study introduces a concise framework for detail enhancement in industrial digital radiography based on the mathematical integration of logarithmic transformation and multiscale Laplacian analysis. The proposed method utilizes multiscale adaptive pixel-level fusion with hyperbolic tangent-based coefficients to preserve microscale defects while enhancing subtle features throughout the dynamic range. Quantitative evaluations of diverse industrial welds, including ship plates, boilers, and oil pipelines, demonstrated substantial improvements. In oil pipeline weld inspections, the Peak Signal-to-Noise Ratio of the method based on Histogram Equalization increased by 133.82%, whereas the Structural Similarity Index Measure and Spatial Frequency metrics exhibited gains of up to 127.27% and 85.81%, respectively. The framework's consistent, albeit moderate, performance gains over state-of-the-art deep learning methods across all benchmarks confirm its value not only as a robust and widely applicable tool but also as a superior preprocessing or integrated solution within nondestructive testing pipelines.

Keywords: digital radiography, multiscale analysis, pixel-level fusion, image detail enhancement, nondestructive testing.

Author α σ ρ §: School of Mechanical Engineering, Guangxi University, Nanning 530004, China.
ↀ ¥: Guangxi Laboratory of Forestry, Guangxi Forestry Research Institute, Nanning 530002, China.

Table 1: List of Notations and Symbols

Symbol	Comment
a	Logarithm base
c	Center position index of Laplacian kernel
d	Manhattan distance from the center
$f(x,y)$	Continuous image intensity function at spatial coordinates (x,y)
f_c	Cutoff frequency in cycles per pixel
$F_{final}(x,y)$	Final fusion result of the pixel at coordinates (x,y)
f_k	A proportionality constant typically ranging from 0.6 to 0.8
$F_k(x,y)$	Enhanced image at scale k
F_{min}	Minimum value of the fusion result across the entire image
F_{max}	Maximum value of the fusion result across the entire image
$G(i,j,\sigma)$	Value of Gaussian kernel at scale σ and position (i,j)
H	Image height
$H(x,y)$	Mean curvature of the intensity surface at pixel (x,y)
$H_G(E)$	Horizontal gradient of the image E between the adjacent pixels in the same row
$I(x,y)$	Discrete image intensity at pixel coordinates (x,y)
$I_{enhanced}(x,y)$	Enhanced image pixel value in grayscale levels at position (x,y)
$I_{log}(x,y)$	Pixel value at position (x,y) after the logarithmic transformation
$I_{orig}(x,y)$	Original pixel value at position (x,y)
$I_{smooth}(x,y,\sigma)$	Smoothed image at scale σ and position (x,y)

Symbol	Comment
$K_{3\times3}$	A standard 3×3 discrete Laplacian kernel
$K_{5\times5}(i,j)$	Value of the 5×5 Laplacian kernel at position (i,j)
$K_{\text{Laplace},k}$	Laplacian kernel of size $(3+2k)\times(3+2k)$ at scale k
$L(x,y)$	Discrete Laplacian response at position (x,y)
N	Total number of scales
$PSNR(E,S)$	Peak signal-to-noise ratio of image E relative to image S
round(·)	Rounding function to the nearest integer
$R_{\text{base}}(x,y)$	Benchmark for Laplacian response differential analysis that is initialized with zeros and becomes the convolution result of the minimal Laplacian kernel once the Laplacian operation is performed.
$R_k(x,y)$	Laplacian response at scale k and position (x,y), which uses the kth Laplacian kernel to convolve the image
size	Laplacian kernel size
$SF(E)$	Spatial frequency of image E
$SSIM(E,S)$	Structural similarity index measure of the image E relative to the image S
tanh (·)	Hyperbolic tangent function
$V_{\text{grayscale}}$	Grayscale value of DR image
$V_G(E)$	Compute the vertical gradient of the image E
V_{display}	Display value
W	Image width
WL	Window level
WW	Window width
$\nabla^2 f(x,y)$	Laplacian operator at spatial coordinates (x,y)
$\partial^2 f(x,y)/\partial x^2$	Second-order partial derivatives in the respective spatial direction X
$\partial^2 f(x,y)/\partial y^2$	Second-order partial derivatives in the respective spatial direction Y
$\nabla^2 G(x,y)$	the Laplacian of the intensity function at pixel (x,y)
$\nabla G(x,y)$	the gradient vector field at pixel (x,y)
$\lvert\nabla G(x,y)\rvert$	the magnitude of the gradient vector at pixel (x,y)
*	Convolution operation
$\lvert\nabla^2 R(x,y)\rvert$	Magnitude of the Laplacian response at pixel coordinates (x,y)
$\mathrm{d}^2R(x,y)/\mathrm{d}s^2$	Second directional derivative along the gradient direction
$\Delta_k(x,y)$	Differences in details between scale k and the benchmark for Laplacian response
a	Logarithm base
δ	A small offset to avoid mathematical singularity at zero
$\mathrm{d}I\log(x,y)/\mathrm{d}I_{\text{orig}}(x,y)$	Derivative of the logarithmic transformation at position (x,y)
$\alpha_k(x,y)$	Importance coefficient of the pixel at position (x,y) and scale k
λ	A factor that controls the detail enhancement sensitivity
$F\{\cdot\}$	Fourier transform operator
(u,v)	Spatial frequency coordinates

I. INTRODUCTION

Industrial digital radiography (DR) has emerged as a critical technology for nondestructive evaluation in precision manufacturing sectors, including the aerospace, automotive, and nuclear power industries[1-3]. DR images characterized by pixel values spanning 0 to 65535 provide an extensive dynamic range for capturing subtle material variations while simultaneously presenting significant challenges for defect detection and characterization[3, 4]. Conventional image enhancement techniques often encounter difficulties in balancing the competing requirements of noise suppression and detail preservation, particularly when addressing micron-scale defects that manifest as minimal intensity variations within complex industrial components[5-7].

The current landscape of industrial DR image enhancement reveals fundamental limitations in

several methodological approaches[3, 8, 9]. Gaussian-dependent multiscale analysis, while effective for noise reduction, intrinsically compromises fine structural details through the systematic attenuation of high-frequency components that are essential for defect characterization[3, 10]. Methods based on discrete wavelet transform (DWT) encounter challenges in optimal basis selection and often introduce reconstruction artifacts when processing complex defect morphologies[11-13]. Histogram equalization (HE) and contrast-limited adaptive histogram equalization (CLAHE) techniques, despite their computational simplicity, frequently produce unnatural contrast amplification and fail to preserve subtle intensity gradients that are critical for accurate defect assessment[14-16]. Although deep learning (DL) approaches, such as methods based on convolutional neural network (CNN), are promising in certain domains, they face substantial limitations, including extensive data requirements, limited interpretability, poor generalization across diverse industrial scenarios, and a lack of physical interpretability[9, 10, 17, 18]. Furthermore, these methods collectively exhibit significant computational complexity, and their parameter sensitivity necessitates extensive manual optimization, undermining operational efficiency in industrial environments[3, 10, 19, 20]. These multifaceted challenges underscore the critical need for a fundamentally new paradigm that can simultaneously address the competing demands of computational efficiency, physical interpretability, and uncompromised detail preservation[6, 21, 22].

To address these challenges, this study introduces a paradigm-shifting framework characterized by a Gaussian-free architecture and pixel-level fusion technology. The proposed method establishes a novel integration of perceptually aligned logarithmic transformation with direct multiscale Laplacian analysis, achieving unprecedented detail preservation while maintaining computational tractability. The framework incorporates an adaptive fusion mechanism governed by hyperbolic tangent importance coefficients, enabling the selective enhancement of defect regions while preserving structural integrity through physically interpretable operations. This approach ensures complete mathematical transparency and eliminates the black-box characteristics that impede the industrial adoption of many contemporary techniques. The principal contributions of this study encompass three key innovations: (1) a comprehensive Gaussian-free mathematical framework that fundamentally redefines multiscale enhancement while preserving computational efficiency; (2) an adaptive pixel-level fusion technology with precise control mechanisms for defect-specific enhancement; and (3) a rigorous theoretical foundation with complete mathematical derivations validated across diverse industrial applications. These advances collectively provide an engineering-friendly solution that balances the enhancement efficacy with the ease of implementation while maintaining full physical interpretability throughout the enhancement pipeline.

This paper is systematically organized to present a novel detail-enhancement method for industrial DR images using multiscale pixel-level fusion techniques. Section 2 establishes the theoretical foundation by reviewing the fundamental concepts of Laplacian transform theory, differential geometric interpretations, discrete implementations, logarithmic transformation principles, and industrial DR imaging characteristics. Section 3 introduces the proposed methodology in detail, beginning with the fundamental principles, followed by the mathematical formulation of the pixel-level adaptive fusion coefficient, construction of multiscale space using Laplacian convolution operator, multiscale pixel-level fusion methodology, enhanced image reconstruction procedures, and strategic avoidance of Gaussian-induced detail destruction. Section 4 presents the experimental setup and analytical methodologies employed for the validation. Section 5 discusses the experimental results and provides a comprehensive analysis of the method's performance, limitations, and potential improvements. Finally, Section 6 concludes the

paper by summarizing the key findings and outlining future research directions.

II. RELATED WORK

2.1 Laplacian Transform Theory

The Laplacian transform is a fundamental mathematical construct in image processing that serves as a second-order differential operator that characterizes local intensity variations through the divergence measurement of the gradient field[23-25]. The continuous two-dimensional equation expresses this relationship as follows:

$$\nabla^2 f(x,y) = \frac{\partial^2 f(x,y)}{\partial x^2} + \frac{\partial^2 f(x,y)}{\partial\ ^2}\# \quad (1)$$

$$\frac{\partial^2 I(x,y)}{\partial x^2} \approx I(x+1,y) - 2I(x,y) + I(x-1,y)\# \quad (2)$$

$$\frac{\partial^2 I(x,y)}{\partial y^2} \approx I(x,y+1) - 2I(x,y) + I(x,y-1)\# \quad (3)$$

where $I(x,y)$ represents the discrete image intensity at pixel coordinates (x,y), and $I(x+1,y)$, $I(x-1,y)$, $I(x,y+1)$, and $I(x,y-1)$ denote the intensity values at adjacent pixel positions. The composite discrete Laplacian operator combines these approximations as follows:

$$L(x,y) = I(x+1,y) + I(x-1,y) + I(x,y+1) + I(x,y-1) - 4I(x,y)\# \quad (4)$$

where $L(x,y)$ represents the discrete Laplacian response at position (x,y).

The Laplacian transform effectively computes the difference between each pixel and its local neighborhood average, functioning as a high-pass filter that amplifies regions with significant intensity variations and suppresses homogeneous areas. It captures the essence of the local curvature in intensity surfaces by quantifying how the average value of a function in the neighborhood of a point differs from its value at the point.

The geometric interpretation of the Laplacian operator reveals its profound connection to surface curvature characteristics [26, 27]. This relationship is formalized by the mean curvature equation:

$$H(x,y) = \frac{\nabla^2 G(x,y)}{2(1+|\nabla G(x,y)|^2)^{3/2}}\# \quad (5)$$

where $\nabla^2 f(x,y)$ denotes the Laplacian operator at spatial coordinates (x,y), $f(x,y)$ represents the continuous image intensity function at spatial coordinates (x,y), $\partial^2 f(x,y)/\partial x^2$ indicates the second-order partial derivatives in the respective spatial direction X, and $\partial^2 f(x,y)/\partial y^2$ indicates the second-order partial derivatives in the respective spatial direction Y.

The discrete implementation employs central difference approximations to achieve computational efficiency while maintaining the mathematical accuracy:

where $H(x,y)$ represents the mean curvature of the intensity surface at pixel (x,y), $\nabla^2 G(x,y)$ denotes the Laplacian of the intensity function at pixel (x,y), $\nabla G(x,y)$ represents the gradient vector field at pixel (x,y), and $|\nabla G(x,y)|$ indicates the magnitude of the gradient vector at pixel (x,y). This mathematical relationship demonstrates that Laplacian responses correlate directly with the local curvature of the intensity landscape, generating strong outputs in regions with high curvature, such as edges, corners, and fine details, while producing minimal responses in relatively flat homogeneous areas.

2.2 Logarithmic Transformation Theory

The logarithmic transformation addresses the fundamental challenge of a high dynamic range in industrial DR images through nonlinear mapping, which compresses the extensive intensity range while preserving the relative contrast

relationships. The mathematical equation defining this transformation is as follows:

$$I_{\log}(x,y) = \log_a(I_{\text{orig}}(x,y) + \delta) \quad (6)$$

where $I_{\text{orig}}(x, y)$ is the original pixel value at position (x, y), $I_{\log}(x, y)$ represents the pixel value at position (x, y) after the logarithmic transformation, a denotes the logarithm base, *and* δ provides a small offset to avoid mathematical singularity at zero.

The transformation employs a compressive nonlinearity to enhance contrast in dark regions and prevent saturation in bright areas, thereby directly addressing the challenge of defects distributed across the full intensity spectrum in industrial DR imaging[28, 29]. Furthermore, derivative analysis confirms that this process intrinsically converts multiplicative noise into an additive form. This critical transformation, which simplifies subsequent denoising while preserving structural integrity, is mathematically expressed as

$$\frac{dI_{\log}(x,y)}{dI_{\text{orig}(x,y)}} = \frac{1}{(I_{\text{orig}}(x,y) + \delta)\ln a} \quad (7)$$

where $dI\log(x,y)/dI_{\text{orig}}(x,y)$ represents the derivative of the logarithmic transformation at position (x,y), indicating the local gain applied during mapping.

$$V_{\text{display}} = \begin{cases} 0 & V_{\text{grayscale}} \le WL - \frac{WW}{2} \\ 255\,\frac{V_{\text{grayscale}} - (WL - \frac{WW}{2})}{WW} & WL - \frac{WW}{2} < V_{\text{grayscale}} < WL + \frac{WW}{2} \\ 255 & V_{\text{grayscale}} \ge WL + \frac{WW}{2} \end{cases} \quad (8)$$

where V_{display} is the display value, WL represents the window level that determines the dynamic range centered for display, and WW denotes the window width that controls the contrast by determining the width of the range of values mapped to the display range. This essential visualization technique enables inspectors to navigate the vast intensity space by dynamically adjusting the displayed contrast and brightness, effectively isolating regions of interest within the 16-bit data for detailed examination[20, 31].

By applying a high gain to the dark regions and a low gain to the bright regions, this derivative enables adaptive enhancement across the dynamic range, directly overcoming the limitations of the uniform linear gain. Moreover, the logarithmic operation renders the noise additive, allowing for its effective removal while protecting critical spatial details from the blurring effects of spatial smoothing. Together, these properties establish a robust method for reducing the influence of noise in DR-image-detail enhancement.

2.3 DR Image Display Principles

DR images are often stored in Digital Imaging and Communications in Medicine (DICOM) files with a 16-bit grayscale[4, 30]. The 16-bit grayscale depth of DR images far exceeds the 256 levels available in standard 8-bit displays. This fundamental disparity creates a critical visualization bottleneck that can obscure subtle defect signatures and material variations essential for an accurate nondestructive evaluation. Practical visualization of DR images employs window-level adjustments to accommodate conventional display systems using the following equation:

III. PROPOSED METHOD

3.1 Methodological Principles

Fig. 1 depicts the overall architecture of the proposed framework, which addresses the fundamental challenges of industrial DR image enhancement by integrating logarithmic transformation with a multiscale Laplacian analysis. The proposed framework is initiated with a logarithmic transformation of the input image to compress its dynamic range and

attenuate noise interference. A multiscale representation is then constructed by convolving the transformed image with Laplacian kernels of progressively increasing sizes, generating a series of response maps that capture the edge and detail information across distinct spatial frequencies. Subsequently, a pixel-importance coefficient map is derived at each scale by comparing its Laplacian response to a designated benchmark. These comparative measurements are processed through a nonlinear activation function to ensure numerical stability. The resulting coefficients subsequently orchestrate a pixel-level fusion process, wherein multiscale detail components are adaptively and proportionally integrated into the logarithmically transformed image. The procedure culminates in a reconstruction phase accompanied by dynamic range normalization, ultimately yielding an enhanced DR image with fused pixels.

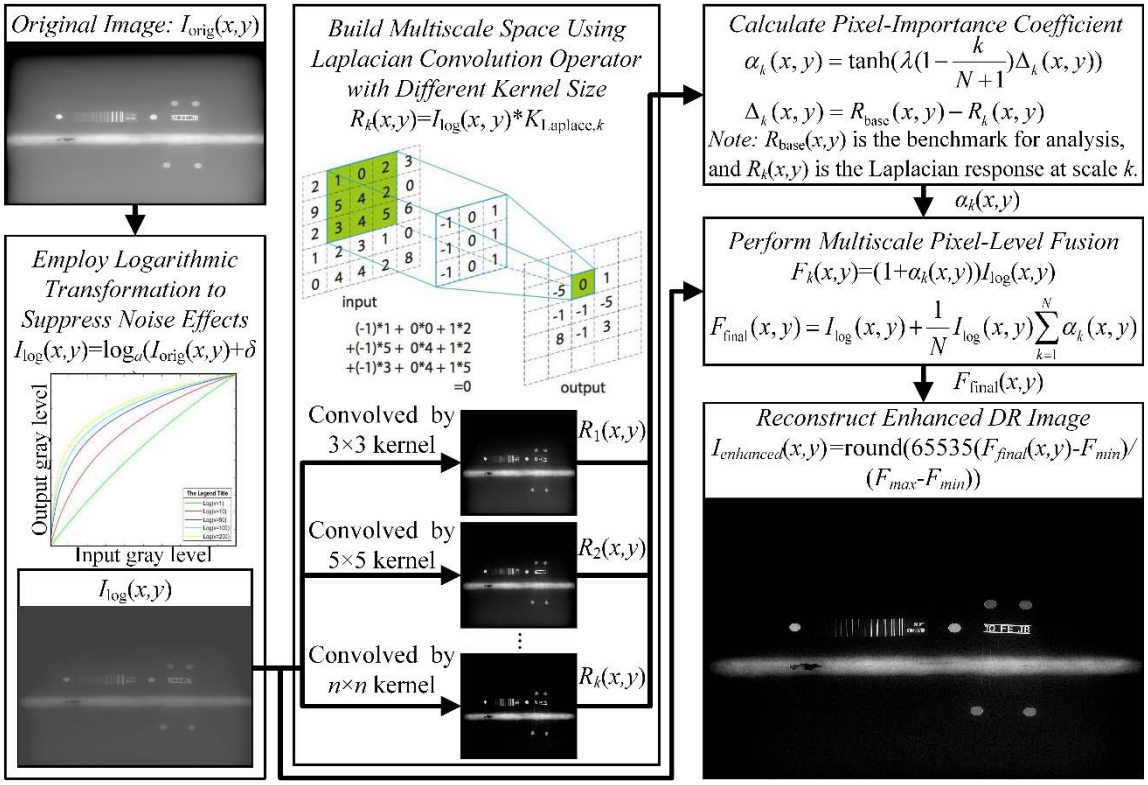

Fig. 1: Principle of Proposed Method

The key idea is to develop a mathematical formulation that entirely obviates Gaussian convolution while preserving the effective enhancement performance. The detail detection mechanism is derived from the fundamental relationship between the Laplacian response and the second-order directional derivative:

$$|\nabla^2 R(x,y)| \propto \left|\frac{\mathrm{d}^2 R(x,y)}{\mathrm{d}s^2}\right| \# \qquad (9)$$

where $|\nabla^2 R(x,y)|$ represents the magnitude of the Laplacian response at pixel coordinates (x,y), $\mathrm{d}^2R(x,y)/\mathrm{d}s^2$ denotes the second directional derivative along the gradient direction, and the proportionality indicates that the Laplacian magnitude corresponds directly to the acceleration of intensity change along the gradient directions, responding most strongly to locations where intensity transitions occur rapidly, such as at edges, corners, and fine texture patterns.

The Laplacian operator capitalizes on its second-order nature to identify fine defects in industrial DR images by highlighting localized intensity transitions. This enables a detailed enhancement scheme that performs pixel-level adaptive fusion using importance coefficients from multiscale Laplacian responses, as follows:

$$F_{\text{final}}(x,y) = \frac{1}{N}\sum_{k=1}^{N}(1+\alpha_k(x,y))\, I_{\log}(x,y) \qquad (10)$$

where $F_{final}(x,y)$ represents the final pixel-level fusion result at position (x,y), N denotes the total number of scales, and $\alpha_k(x,y)$ signifies the pixel-importance coefficient at position (x,y) and scale k. This formulation represents a sophisticated blending of multiscale information, in which the term $(1+\alpha_k(x,y))$ functions as an adaptive gain factor that varies spatially and across different scales. When $\alpha_k(x,y)$ assumes positive values, indicating the presence of significant details at scale k, the gain increases to enhance these details. Conversely, when $\alpha_k(x,y)$ takes negative values, suggesting the absence of meaningful details, the gain decreases to suppress the noise or irrelevant variations.

3.2 Method for Calculating Pixel-Level Adaptive Fusion Coefficient

The pixel-importance coefficient serves as the pixel-level adaptive fusion coefficient. It plays a pivotal role in determining the appropriate enhancement strength at each pixel location across different scales, with the calculation employing the hyperbolic tangent function for adaptive coefficient generation as follows:

$$\alpha_k(x,y) = \tanh(\lambda(1-\frac{k}{N+1})\Delta_k(x,y))\# \quad (11)$$

where $\tanh(\cdot)$ denotes the hyperbolic tangent function, $\Delta_k(x,y)$ represents the differences in details between scale k and the benchmark for the Laplacian response differential analysis at position (x,y), λ is a factor that controls the detail enhancement sensitivity because $\Delta_k(x,y)$ is often a small value, and the term $\lambda(1-k/(N+1))$ adaptively tunes $\Delta_k(x,y)$ based on the fact that the convolution result of a smaller Laplacian kernel contains more important information than a larger one. A higher λ enhances the contrast but loses some extremely fine features. Empirical evidence suggests that λ typically ranges from $3N$ to $7N$.

According to Laplace theory, larger Laplace kernels preserve global textures, whereas smaller Laplace kernels retain local details. Based on this principle, the physical implication of Equation (11) is that the greater the deviation of the convolutional responses using Laplace kernels of different sizes relative to the Laplacian response analytical baseline, the more detailed the information contained in the pixel, and the more critical it becomes for enhancing details.

In Equation (11), the hyperbolic tangent function serves as a smooth, bounded activation function that converts raw detail differences into normalized importance coefficients within the range (-1,1). The characteristic S-shaped curve of this function provides several advantageous properties: (1) for small detail differences, it operates in an approximately linear region, delivering a proportional response to subtle variations; (2) for large differences, it saturates to ±1, preventing over-enhancement that could introduce artificial artifacts or unnatural appearances. This saturation behavior is crucial for maintaining visually coherent results while providing a robust enhancement. The parameter λ controls the steepness of the transition between the linear and saturated regions, effectively determining the sensitivity to detail variations and allowing adjustment based on specific image characteristics and enhancement requirements.

Based on the principle of Laplacian response, the method for calculating the differences in details is as follows:

$$\Delta_k(x,y) = R_{\text{base}}(x,y) - R_k(x,y)\# \quad (12)$$

where $R_{base}(x,y)$ is the benchmark for the Laplacian response differential analysis, which is initialized with zeros and becomes the convolution result of the minimal Laplacian kernel once the Laplacian operation is performed, and $R_k(x,y)$ represents the Laplacian response at scale k and position (x,y), obtained by convolving the image with the kth Laplacian kernel.

Based on Equation (12), positive values of $\Delta_k(x,y)$ indicate that the finest-scale kernel detects details that are not captured by the larger kernel, suggesting the presence of fine-scale features such as small defects or sharp edges, whereas negative values of $\Delta_k(x,y)$ suggest that the larger kernel responds more strongly, indicating the presence of larger-scale structures or more gradual variations in the intensity. This multiscale difference approach effectively separates the

details of different spatial extents, enabling the targeted enhancement of specific feature sizes without affecting others and providing comprehensive coverage across the spectrum of defect scales present in DR images.

3.3 Method for Building Multiscale Space using Laplacian Convolution Operator

Multiscale analysis employs direct Laplacian kernels of varying sizes applied to the logarithmically transformed image, completely avoiding the Gaussian convolution operations that characterize traditional approaches.

$$R_k(x,y) = I_{\log}(x,y) * K_{\text{Laplace},k}, k = 1,2,\ldots,N\# \tag{13}$$

where $*$ denotes the convolution operation, and $K_{\text{Laplace},k}$ signifies the Laplacian kernel of size $(3+2k)\times(3+2k)$ at scale k. This multiscale methodology represents a fundamental departure from Gaussian-based methods by applying Laplacian kernels of different sizes directly to the image, thereby preserving the high-frequency information that would otherwise be attenuated by the Gaussian smoothing. Each kernel size responds preferentially to features of particular spatial extents: smaller kernels capture fine details and sharp edges, whereas larger kernels respond to broader structures and more gradual intensity variations. This comprehensive representation across feature scales is essential for detecting the diverse range of defects encountered in industrial DR applications.

The kernel design follows a systematic expansion methodology based on the Manhattan distance weighting. For the standard 3×3 kernel:

$$K_{3\times3} = \begin{bmatrix} 0 & 1 & 0 \\ 1 & -4 & 1 \\ 0 & 1 & 0 \end{bmatrix}\# \tag{14}$$

where $K_{3\times3}$ represents the 3×3 Laplacian kernel with elements arranged to approximate the discrete second-derivative operation. For 5×5 or larger kernels, weights are assigned according to the Manhattan distance d = $|i - c| + |j - c|$, where c is half the kernel size. The 5×5 kernel design exemplifies this approach.

$$K_{5\times5}(i,j) = \begin{cases} -20 & d = 0 \\ 4 & d = 1 \\ 1 & d = 2 \wedge |i-c| = |j-c| = 1 \\ 0 & \text{otherwise} \end{cases}\# \tag{15}$$

where $K_{5\times5}(i,j)$ represents the value of the 5×5 Laplacian kernel at position (i,j), d denotes the Manhattan distance from the center, and c is the center position index of the Laplacian kernel. All kernels maintain the zero-sum property essential for the Laplacian operation:

$$\sum_{i=0}^{size-1}\sum_{j=0}^{size-1} K_{\text{Laplace},k}(i,j) = 0\# \tag{16}$$

where the summation covers all kernel positions (i,j), the symbol *size* represents the Laplacian kernel size, and the zero result ensures that the kernels respond only to intensity variations in the image and produce zero response in regions of constant intensity, preventing unnecessary enhancement of homogeneous areas while amplifying variations associated with defects and structural features.

The relationship between the kernel size and spatial frequency response follows the approximate equation:

$$f_c \approx \frac{f_k}{size}\# \tag{17}$$

where f_c represents the cutoff frequency in cycles per pixel and f_k denotes a proportionality constant typically ranging from 0.6 to 0.8. This relationship reveals the fundamental connection between the kernel size and the spatial frequencies to which the kernel responds: smaller

kernels with higher cutoff frequencies capture finer details and sharper edges, whereas larger kernels with lower cutoff frequencies respond to broader features and more gradual intensity variations. This frequency-space interpretation provides a comprehensive framework for understanding how different kernel sizes capture distinct aspects of the image content, ensuring that defects of various scales, from microscopic cracks to larger structural anomalies, are appropriately detected and enhanced.

3.4 Method for Performing Pixel-Level Multiscale Adaptive Fusion

The pixel-level fusion process integrates enhanced representations from all scales through a weighted combination that adapts to the local detail characteristics. The enhancement at each individual scale follows the equation:

$$F_k(x,y) = (1 + \alpha_k(x,y))I_{\log}(x,y)\# \quad (18)$$

where $F_k(x,y)$ represents an enhanced image at scale k. This equation embodies the core enhancement mechanism at each scale, with the term $(1+\alpha_k(x,y))$ functioning as a spatially varying gain that amplifies or attenuates the pixel value based on the coefficient importance. When significant details are detected at a particular scale ($\alpha_k(x,y) > 0$), the pixel value is amplified, enhancing the visibility of these details. When no significant details are present ($\alpha_k(x,y) \le 0$), minimal or no enhancement is applied, preventing the artificial amplification of noise or irrelevant variations. This scale-specific approach enables the targeted enhancement of features based on their size characteristics, ensuring that small defects receive appropriate enhancement without adversely affecting larger structures.

Multiscale fusion combines all scales through equal-weight averaging as follows:

$$F_{\text{final}}(x,y) = \frac{1}{N}\sum_{k=1}^{N} F_k(x,y)\# \quad (19)$$

This equation can be algebraically expanded to reveal the underlying enhancement mechanism as follows:

$$F_{\text{final}}(x,y) = I_{\log}(x,y) + \frac{1}{N} I_{\log}(x,y)\sum_{k=1}^{N} \alpha_k(x,y)\# \quad (20)$$

where the expanded form clearly separates the original image content $I_{\log}(x,y)$ from the enhancement component $\frac{1}{N} I_{log}(x,y)\sum_{k=1}^{N} \alpha_k(x,y)$.

This separation has significant implications: the enhancement is proportional to both the local intensity value and the cumulative importance across all scales. Multiplication by $I_{\log}(x,y)$ ensures that the enhancement respects the local intensity context: brighter regions receive stronger absolute enhancement, whereas darker regions receive more modest enhancement, maintaining a natural appearance and preventing artificial-looking results. The summation over the importance coefficients ensures that the details detected at multiple scales contribute collectively to the final enhancement, providing comprehensive detail amplification across the entire spectrum of feature sizes present in the image.

3.5 Method for Reconstructing Enhanced DR Image

The final enhanced image requires transformation back to the conventional 16-bit grayscale representation to ensure compatibility with standard display systems and analysis tools. The method used to reconstruct the final enhanced DR Image is as follows:

$$I_{\text{enhanced}}(x,y) = \text{round}\left(65535\frac{F_{\text{final}}(x,y) - F_{\min}}{F_{\max} - F_{\min}}\right)\# \quad (21)$$

where $I_{\text{enhanced}}(x,y)$ represents the enhanced image pixel value in grayscale levels at position (x,y), round$(\cdot)$ signifies the rounding function to the nearest integer, $F_{\text{final}}(x,y)$ denotes the final fusion result, $F_{\min}=\min(F_{\text{final}})$ represents the minimum value of the fusion result across the entire image, $F_{\max}=\max(F_{\text{final}})$ indicates the maximum value of the fusion result across the entire image, and 65535 corresponds to the maximum value in the

65535 corresponds to the maximum value in the 16-bit representation.

This normalization process serves two crucial purposes in the enhancement pipeline: first, it maps the processed floating-point values back to the standard 16-bit integer format required for display, storage, and subsequent analysis; second, it preserves the relative contrast relationships established during the multiscale fusion. This mapping preserves the proportional differences between pixel values, ensuring both enhanced visibility of details and maintained fidelity of image intensity relationships. This preservation is crucial for quantitative analysis, where absolute or relative intensities have physical significance pertaining to material properties, thickness variations, or defect characteristics.

3.6 Gaussian Blurring Induced Detail Destruction and Avoidance Strategy

Traditional multiscale analysis methods employ Gaussian convolution for scale-space representation, with the convolution operation mathematically expressed as

$$I_{\text{smooth}}(x, y, \sigma) = I(x, y) * G(i, j, \sigma)\# \quad (22)$$

where $I_{\text{smooth}}(x,y,\sigma)$ represents the result of the smoothed image at scale σ and position (x,y), * denotes the convolution operation, and $G(i,j,\sigma)$ denotes the value of the Gaussian kernel at scale σ and position (i,j). The Gaussian kernel is defined as follows:

$$G(i, j, \sigma) = \frac{1}{2\pi\sigma^2} e^{-\frac{i^2+j^2}{2\sigma^2}}\# \quad (23)$$

where the term $1/(2\pi\sigma^2)$ serves as a normalization constant. The frequency response of this operation reveals its fundamental limitation:

$$\mathcal{F}\{G(i, j, \sigma)\} = e^{-2\pi^2\sigma^2(u^2+v^2)}\# \quad (24)$$

where $F\{\cdot\}$ denotes the Fourier transform, and (u,v) represents the spatial frequency coordinates. This exponential decay demonstrates that the Gaussian convolution systematically attenuates the high-frequency components in the image, with the degree of attenuation increasing with both the spatial frequency and scale parameter σ.

While this smoothing behavior is beneficial for noise reduction, it fundamentally damages the most critical information for industrial DR image enhancement: fine details, sharp edges, and high-frequency textures that correspond to defect signatures and material discontinuities. This creates an inherent trade-off in traditional approaches—the same operation that reduces noise also destroys important details, severely limiting the effectiveness for industrial inspection applications where preserving fine features is essential for reliable defect detection.

The proposed method addresses this limitation by eliminating Gaussian convolution operations and employing a three-pronged alternative strategy: (1) this comprehensive approach preserves the high-frequency components containing critical defect signatures while providing robust enhancement through complementary processing stages; (2) the logarithmic transformation handles dynamic range issues without spatial averaging, thereby maintaining finer detail integrity than Gaussian convolution; and (3) the direct multiscale Laplacian methodology extracts the information of details across the spatial frequencies without the blurring inherent using Gaussian operations. The adaptive fusion process achieves noise robustness through selective enhancement rather than spatial smoothing, representing a fundamentally different paradigm for handling image quality challenges while preserving the essential structural information.

IV. RESULTS

4.1 Experimental Setup

The experimental study employed DR images obtained from nondestructive welding quality inspections to comprehensively validate the proposed method. These DR images were sourced from nondestructive testing across three welding scenarios and were stored in DICOM format with a dynamic range of 0-65535.

To rigorously assess the efficacy of the proposed method, a comparative analysis was performed using several DR image detail-enhancement techniques. These benchmark methods included a method based on histogram equalization (HE)

[32], a method based on contrast-limited adaptive histogram equalization (CLAHE) [33], a method based on discrete wavelet transform (DWT) [34], and a CNN-based detail enhancement method (CNN-DEMD) [35]. It should be specifically noted that the dataset employed for training the CNN-DEMD benchmark comprised 1202 original DR images sourced from nondestructive testing results of weld quality. Following data augmentation, the dataset used to train the CNN-DEMD comprised 3606 samples.

The experiment utilized 30 DR images of weld nondestructive testing sourced from different industrial sectors (10 DR images from each sector) for comprehensive testing. All DR images were acquired using the system shown in Fig. 2. A brief summary of the 20 DR images is presented in Table 2.

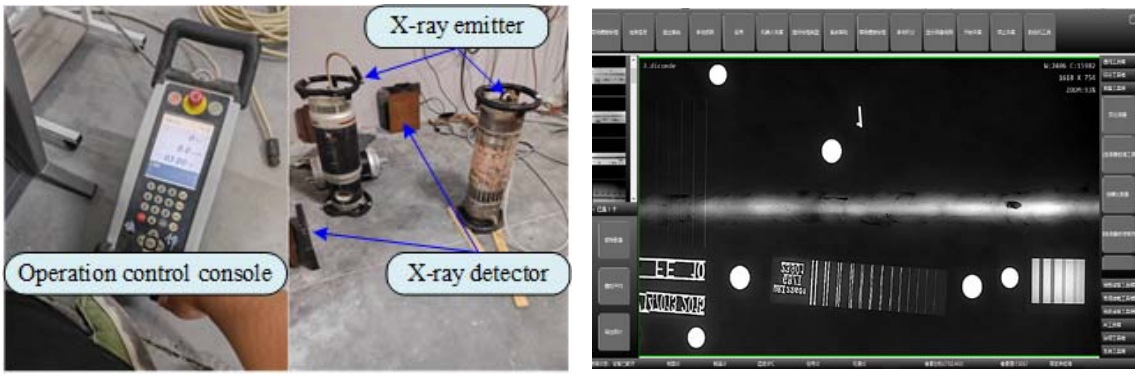

(a) (b)

Fig. 2: Experimental platform: (a) hardware and (b) software

Table 2: A Brief Summary of the 30 DR Images

Source	Resolution	Major Defects	Average Thickness/mm	Total
Weld in ship plate	2048 x 1800	Linear defects and pores	33	10
Weld in boiler	1820 x 768	Linear defects and pores	38	10
Weld in oil pipeline	1280 x 1024	Linear defects and pores	26	10

Three metrics were employed for the quantitative assessment of detail-enhancement performance. The Peak Signal-to-Noise Ratio (PSNR) functions as a statistical metric for evaluating the ratio between the maximum possible signal power and the power of the corrupting noise, and is commonly used for image quality assessment. The Structural Similarity Index Measure (SSIM) quantifies the perceived structural fidelity between a processed image and its original, unprocessed counterpart. The Spatial Frequency (SF), which indicates the overall activity level in an image, is used to measure the change rate of intensity across pixels. Elevated SF values are associated with sharper edge definitions and richer textural details, correlating with superior perceptual quality. The computations for PSNR, SSIM, and SF are defined by Equations (25), (26), and (27), respectively, as follows:

$$PSNR(\boldsymbol{E},\boldsymbol{S}) = 10\log_{10}\left\{\frac{65535^2}{\frac{\sum_{x=1}^{H}\sum_{y=1}^{W}[\boldsymbol{E}(x,y)-\boldsymbol{S}(x,y)]^2}{W\times H}}\right\}\# \tag{25}$$

$$SSIM(\boldsymbol{E},\boldsymbol{S}) = \frac{(2\mu_E\mu_S + c_1)(2\sigma_{ES} + c_2)}{(\mu_E{}^2 + \mu_S{}^2 + c_1)(\sigma_E{}^2 + \sigma_S{}^2 + c_2)}\# \tag{26}$$

$$\begin{cases} SF(\boldsymbol{E}) = \sqrt{H_G(\boldsymbol{E})^2 + V_G(\boldsymbol{E})^2} \\ H_G(\boldsymbol{E}) = \sqrt{\dfrac{1}{W \times H} \sum_{x=1}^{W} \sum_{y=1}^{H-1} [\boldsymbol{E}(x,y) - \boldsymbol{E}(x,y+1)]^2} \\ V_G(\boldsymbol{E}) = \sqrt{\dfrac{1}{W \times H} \sum_{x=1}^{W-1} \sum_{y=1}^{H} [\boldsymbol{E}(x,y) - \boldsymbol{E}(x+1,y)]^2} \end{cases} \#$$

where $PSNR(E,S)$ is the peak signal-to-noise ratio of the image E relative to the image S, $SSIM(E,S)$ is the structural similarity index measure of the image E relative to the image S, $SF(E)$ is the spatial frequency of the image E, $H_G(E)$ computes the horizontal gradient of the image E, $V_G(E)$ computes the vertical gradient of the image E, W is the image width, H is the image height, μ_E is the mean of the image E, c_1 and c_2 are two constants, μ_S is the mean of the image S, σ_E is the variance of the image $\boldsymbol{E}$, σ_S is the variance of the image S, and σ_{ES} is the covariance of the images $\boldsymbol{E}$ and S.

The parameter configuration for the proposed method utilized N=4 scales with kernel sizes progressively increasing from 3×3 to 9×9, enhancement factor λ=5N=20 controlling detail enhancement sensitivity, and logarithm base a=10 compressing the DR image grayscale. This parameter set was determined through systematic optimization of the experimental dataset to achieve a balanced performance across different image types and defect characteristics.

4.2 Objective Analysis

After applying several distinct methodologies for detail enhancement to the DR images obtained from three different sources, the processed results are presented in Figs. 3–5. It should be noted that the red-marked areas in these figures indicate defect regions. For reference, although the entire experiment comprised 30 images, only representative samples from each source are displayed here.

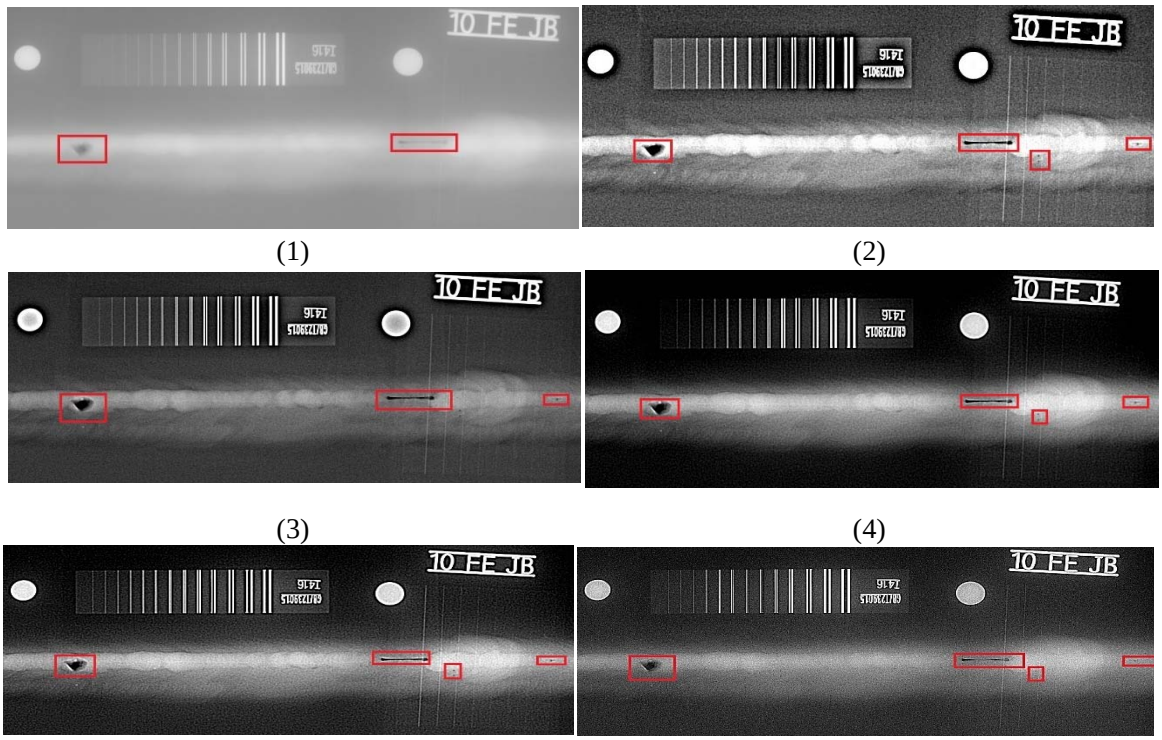

Fig. 3: Performance of different methods on a ship plate weld image: (1) original, (2) HE, (3) CLAHE, (4) DWT, (5) CNN-DEMD, and (6) proposed method

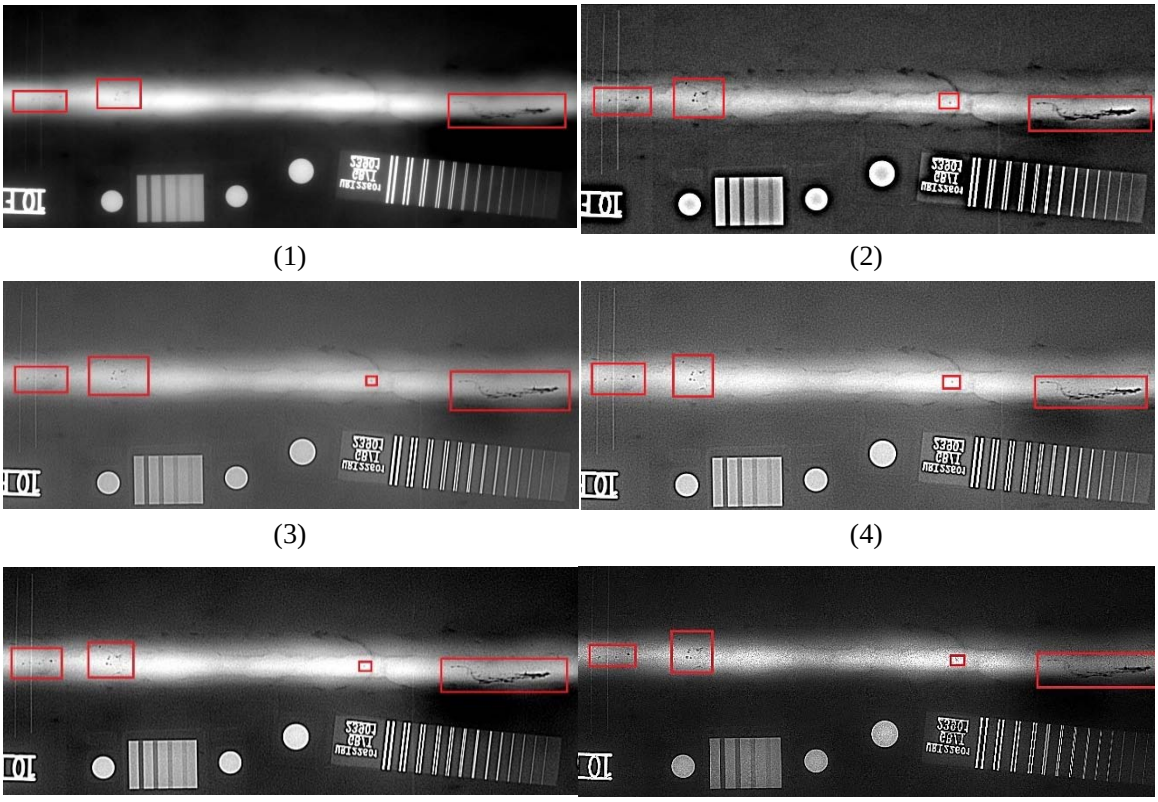

Fig. 4: Performance of proposed method against existing methods on a boiler weld image: (1) original, (2) HE, (3) CLAHE, (4) DWT, (5) CNN-DEMD, and (6) proposed method

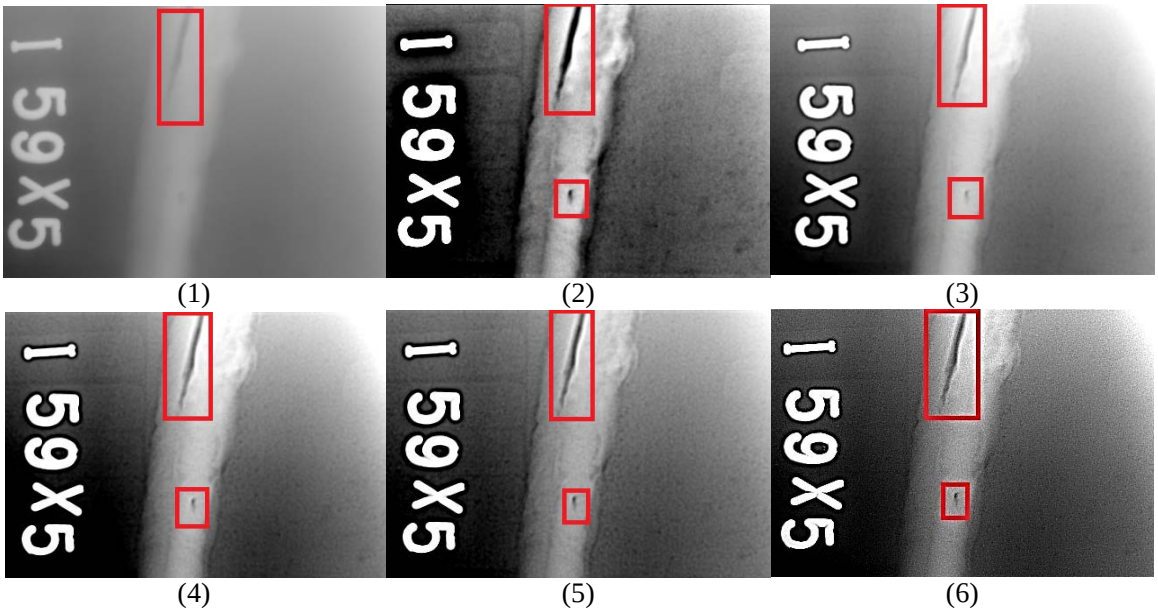

Fig. 5: Performance of the proposed method against existing algorithms on an oil-pipeline weld image: (1) original, (2) HE, (3) CLAHE, (4) DWT, (5) CNN-DEMD, and (6) proposed method

A visual examination of Figs. 2–4 reveals that the proposed method achieves superior performance compared with other algorithms, exhibiting enhanced clarity, sharpness, fidelity, delicacy, and artifact reduction compared with other algorithms. This method effectively enhances images via pixel-level adaptive fusion, leveraging logarithmic transformation and a multiscale Laplacian transform.

4.3 Result Analysis

Notably, the proposed method achieved superior performance, attaining the highest mean PSNR across all three industrial weld inspection scenarios—ship plates, boilers, and oil pipelines—with values of 26.12, 25.17, and 26.96, respectively (Table 3). This reflects a statistically significant and consistent enhancement over existing techniques.

As illustrated in Table 3, performance escalates progressively from conventional approaches such as HE and CLAHE (PSNR: 11–15), through moderate gains with DWT (~17–20), to a marked improvement via CNN-DEMD (23–26). The proposed method builds upon this trajectory, delivering further gains.

Moreover, the proposed approach demonstrates enhanced statistical robustness, exhibiting the lowest standard deviation in PSNR across test cases (0.68, 0.74, 0.71), as shown in Table 4. This trend of declining variability—from traditional to advanced techniques—culminates in the proposed method, underscoring its stability and reliability.

Table 3: Average PSNR Across Different Enhancement Methods

DR Image Source	HE	CLAHE	DWT	CNN-DEMD	Proposed Method
Weld in ship plate	13.68	14.29	19.33	24.89	26.12
Weld in boiler	12.86	14.35	17.87	23.38	25.17
Weld in oil pipeline	11.53	15.18	20.12	25.57	26.96

Table 4: Standard Deviation of PSNR across different enhancement methods

DR Image Source	HE	CLAHE	DWT	CNN-DEMD	Proposed Method
Weld in ship plate	1.53	1.37	1.15	0.82	0.68
Weld in boiler	1.68	1.42	1.23	0.87	0.74
Weld in oil pipeline	1.71	1.29	1.08	0.93	0.71

A comparative analysis of the experimental results (Tables 5 and 6) demonstrates the consistent superiority of the proposed method in terms of structural fidelity and robustness across all test scenarios. As indicated in Table 5, the proposed technique attained the highest mean Structural Similarity Index Measure (SSIM) for welds from ship plates (0.75), boilers (0.73), and oil pipelines (0.76), reflecting more effective structural preservation relative to the benchmark approaches. The performance hierarchy remains stable: the proposed method surpasses CNN-DEMD, which in turn exceeds the Discrete Wavelet Transform (DWT) method, whereas conventional techniques such as Histogram Equalization (HE) and CLAHE yield markedly lower SSIM values.

This performance advantage is complemented by enhanced robustness, quantified by the SSIM standard deviations in Table 6. For the challenging "Weld in ship plate" dataset, the proposed method achieved the highest mean SSIM and the lowest deviation (0.062), indicating superior stability. A comparable trend was observed for the boiler welds. Although the deviation for oil pipeline welds (0.069) slightly exceeded that of the DWT method (0.061), this marginal trade-off was substantially offset by a significant advantage in the mean SSIM (0.76 vs. 0.61). Collectively, the high mean SSIM and generally low variance underscore the efficacy and reliability of the proposed method in delivering structurally faithful enhancements across various industrial radiography contexts.

Table 5: Average SSIM across different enhancement methods

DR Image Source	HE	CLAHE	DWT	CNN-DEMD	Proposed method
Weld in ship plate	0.33	0.47	0.68	0.72	0.75
Weld in boiler	0.42	0.56	0.63	0.68	0.73
Weld in oil pipeline	0.38	0.49	0.61	0.73	0.76

Table 6: Standard Deviation of SSIM across different enhancement methods

DR Image Source	HE	CLAHE	DWT	CNN-DEMD	Proposed method
Weld in ship plate	0.084	0.081	0.076	0.072	0.062
Weld in boiler	0.075	0.077	0.069	0.069	0.067
Weld in oil pipeline	0.073	0.068	0.061	0.064	0.069

As shown in Table 7, the proposed image enhancement method consistently achieved the highest average Spatial Frequency (SF) across all three industrial weld inspection scenarios. For welds in ship plates, boilers, and oil pipelines, SF values of 18.86, 18.27, and 19.18 were attained, respectively, indicating superior image clarity and textural enhancement. A clear performance hierarchy is observable: conventional techniques like HE and CLAHE yield the lowest SF values (9.84-13.76), followed by a moderate improvement with DWT (14.82-15.26). A significant leap is realized by the CNN-DEMD method (17.33-18.42), which the proposed method subsequently surpasses.

The superior performance of the proposed method is coupled with its exceptional stability. The standard deviation data presented in Table 8 consistently demonstrate the lowest or nearly lowest variance in the SF output. With standard deviations of 0.24, 0.21, and 0.23 for the respective test cases, the method exhibited remarkable robustness. This trend of decreasing standard deviation from traditional to advanced methods culminates in the proposed algorithm, confirming its reliability in minimizing performance fluctuations while maximizing spatial frequency.

Table 7: Average SF across different enhancement methods

DR Image Source	HE	CLAHE	DWT	CNN-DEMD	Proposed method
Weld in ship plate	10.15	12.15	15.14	18.19	18.86
Weld in boiler	9.84	11.83	15.26	17.33	18.27
Weld in oil pipeline	11.33	13.76	14.82	18.42	19.18

Table 8: Standard Deviation of SF across different enhancement methods

DR Image Source	HE	CLAHE	DWT	CNN-DEMD	Proposed method
Weld in ship plate	0.53	0.43	0.33	0.23	0.24
Weld in boiler	0.55	0.41	0.31	0.26	0.21
Weld in oil pipeline	0.52	0.44	0.32	0.22	0.23

As quantified in Table 9, the proposed method yields substantial PSNR enhancements across all benchmarked image-enhancement techniques in three welding inspection scenarios. Two principal findings emerged: first, traditional methods, notably HE and CLAHE, exhibited the most marked relative gains, with PSNR increases exceeding 75% and, in one case, surpassing 130%, underscoring a pronounced performance gap relative to the proposed technique. Second, and more significantly, the method demonstrates universal applicability, consistently refining even advanced approaches, such as CNN-DEMD. The modest yet consistent gains (approximately 4–8%) observed here are paradoxically indicative of CNN-DEMD's strong baseline performance, thereby highlighting the proposed method's efficacy as a robust post-processing or integration module. In summary, the results systematically affirm the method's capacity to markedly augment conventional algorithms while delivering measurable improvements to the state-of-the-art deep learning models.

Table 9: The proposed method's enhancement of the PSNR for other methods

Compared Method	Weld in Ship Plate /%	Weld in Boiler /%	Weld in Oil Pipeline /%
HE	90.94	95.72	133.82
CLAHE	82.79	75.40	77.60
DWT	35.13	40.85	34.00
CNN-DEMD	4.94	7.66	5.44

As evidenced by the SSIM enhancement metrics in Table 10, the proposed method consistently improves the structural similarity across a spectrum of benchmark techniques, following a distinct and interpretable trend. The most pronounced gains were observed with traditional algorithms: HE achieved a remarkable 127.27% improvement in "Weld in ship plate" and 100.00% in "Weld in oil pipeline," culminating in a total improvement of 100.36%, whereas CLAHE exhibited a 48.34% total gain. These results indicate a strong compensatory effect on the structural distortions inherent to conventional approaches.

In contrast, enhancements for advanced methods, such as DWT and CNN-DEMD, although consistent, were more moderate (16.92% and 5.21%, respectively). This inverse correlation between methodological sophistication and improvement magnitude underscores the proposed method's capacity to deliver substantial benefits for weaker algorithms while still providing statistically meaningful refinements to the state-of-the-art techniques.

In summary, the consistent positive improvements validate the robustness and general applicability of the proposed method as a universal enhancer of structural fidelity in welding inspection imagery.

Table 10: The proposed method's enhancement of the SSIM for other methods

Compared Method	Weld in Ship Plate /%	Weld in Boiler /%	Weld in Oil Pipeline /%
HE	127.27	73.81	100.00
CLAHE	59.57	30.36	55.10
DWT	10.29	15.87	24.59
CNN-DEMD	4.17	7.35	4.11

As demonstrated in Table 11, the proposed method significantly enhanced the performance of various techniques across multiple welding inspection scenarios. Notably, the most substantial improvement was observed for the HE method, with a total improvement of 80.26%, reflecting considerable gains in weld detection accuracy for ship plates (85.81%), boilers (85.67%), and oil pipelines (69.29%).

Conversely, CLAHE exhibited moderate enhancement, achieving a 49.69% overall improvement, although its absolute performance remained lower, particularly in oil pipeline contexts (39.39%). The DWT-based method showed more limited gains, with a total improvement of 24.57%, whereas CNN-DEMD demonstrated the least improvement (4.41%), indicating its inherent robustness and lower susceptibility to further enhancement under the proposed framework.

These results collectively underscore the versatility and efficacy of the proposed method in augmenting both traditional and advanced techniques, with the degree of improvement being inversely related to the baseline sophistication of each compared method.

Table 11: The proposed method's enhancement of the SF for other methods

Compared Method	Weld in Ship Plate /%	Weld in Boiler /%	Weld in Oil Pipeline /%
HE	85.81	85.67	69.29
CLAHE	55.23	54.44	39.39
DWT	24.57	19.72	29.42
CNN-DEMD	3.68	5.42	4.13

V. DISCUSSION

A Gaussian-free multiscale detail-enhancement framework is proposed for industrial DR images that fundamentally addresses the inherent limitation of detail destruction in conventional approaches using Gaussian convolution. The core innovation lies in the integration of logarithmic transformation with direct multiscale Laplacian analysis, the development of adaptive importance coefficients using hyperbolic tangent functions, a systematic methodology for generating Laplacian kernels, and achieving multiscale pixel-level adaptive fusion. Collectively, these elements establish a rigorous and mathematically coherent framework for detail-preserving DR-image-detail enhancement.

The experimental results demonstrate the efficacy and general applicability of our method. The proposed framework universally enhances the established techniques—HE, CLAHE, DWT, and CNN-DEMD—across diverse industrial weld inspection scenarios (ship plate, boiler, and oil pipeline). Most strikingly, it elevates the PSNR of HE by 133.82% for the oil pipeline welds. Substantial gains were also observed in the SSIM (HE improved by 127.27% for ship plate welds) and SF (HE enhanced by 85.81% for the same application). Although the performance uplift over more sophisticated methods, such as CNN-DEMD, is more modest (e.g., 4.94–7.66% for PSNR), the consistent positive enhancement across all benchmarks underscores its robustness as a superior preprocessing or integrated solution for nondestructive testing.

The significant results achieved through experimental validation include demonstrated superiority in micron-scale defect detection, robust performance across diverse industrial applications and image characteristics, and practical implementation feasibility for real-time inspection systems. The method's ability to enhance detail visibility while preserving structural integrity addresses a critical need in industrial nondestructive testing, where reliable defect detection must be balanced with maintaining an accurate structural representation for subsequent analysis and decision-making.

This study had several limitations that warrant consideration. First, the proposed framework was developed and validated specifically on DR images of weld defects; its efficacy on DR images from other industrial sources (e.g., castings or composite materials) remains unverified. Second, despite its performance gains, the computational complexity of the multiscale analysis requires further optimization for real-time deployment in resource-constrained environments. Finally, the experimental validation, while demonstrating robust results, was conducted on a limited dataset, and large-scale comprehensive testing is required to fully ascertain its generalizability.

Future research should prioritize three principal avenues of investigation. First, efforts should be directed toward broadening the scope of application of the method to encompass a wider array of industrial nondestructive testing (NDT) scenarios, with a rigorous assessment of its cross-domain robustness. Concurrently, dedicated efforts will be channeled into algorithmic refinement and implementation optimization to improve the computational efficiency. Furthermore, a more comprehensive evaluation using large-scale, multi-source datasets will be undertaken to thoroughly validate the performance of the proposed method. This may be supplemented by the development of adaptive parameter strategies and their integration with deep learning models to augment feature learning capabilities.

VI. CONCLUSION

To address the limitations inherent in existing detail-enhancement techniques for industrial DR images, this study introduces a novel Gaussian-free detail-enhancement framework by integrating logarithmic transformation and multiscale Laplacian analysis. This method fundamentally departs from traditional Gaussian-based approaches by eliminating the blur-inducing convolution operations. This study establishes a new detail-enhancement paradigm for industrial DR images through a multiscale, pixel-level adaptive fusion mechanism that directly and faithfully preserves critical image details.

The superior performance and generalizability of the framework were demonstrated through rigorous quantitative evaluations. It achieves unprecedented enhancement across diverse weld inspection scenarios, elevating the PSNR of a basic HE method by 133.82% for oil pipeline-welds. Substantial gains in the SSIM (up to 127.27%) and SF (up to 85.81%) further confirmed its efficacy. Critically, it delivers consistent, albeit more modest, improvements over sophisticated benchmarks such as CLAHE, DWT, and CNN-DEMD, underscoring its robustness as a premier preprocessing or integrated solution for nondestructive testing.

This study makes three pivotal contributions: (1) it provides a highly effective technical foundation with significant potential to transform quality assurance in manufacturing; (2) it inaugurates a Gaussian-free paradigm that prioritizes structural fidelity, which is a critical requirement for high-precision industrial applications; and (3) it provides an adaptive pixel-level fusion technology with precise control mechanisms for defect-specific enhancements.

ACKNOWLEDGEMENT

This study was funded by the Guangxi Science and Technology Program, China (Grant No. 2025LTLT02001).

REFERENCES

1. Grigorchenko, S.A. and V.I. Kapustin, *Enhancing the Efficiency of Defect Image Identification in Computer Decoding of Digital Radiographic Images of Welded Joints in Hazardous Industrial Facilities*. Russian Journal of Nondestructive Testing, 2024, 60(12): 1387-1395. https://www.doi.org/10.1134/s1061830924602836.
2. Kenderian, S., et al., *Contrast-based notch-to-crack transfer function for digital radiography*. Insight, 2024, 66(7): 400-408. https://www.doi.org/10.1784/insi.2024.66.7.400.
3. Xue, W.J., Y.M. Wang, and Z. Qin, *Multiscale Feature Attention Module Based Pyramid Network for Medical Digital Radiography*

Image Enhancement. Ieee Access, 2024, 12: 53686-53697. https://www.doi.org/10.1109/access.2024.3387413.
4. Yoo, S., et al., *Analysis of absorption signal and noise in thin phosphor detectors for high-energy transmission radiography*. Journal of Instrumentation, 2023, 18(10). https://www.doi.org/10.1088/1748-0221/18/10/c10017.
5. García-Pérez, A., M.J. Gómez-Silva, and A. de la Escalera-hueso, *Improving automatic defect recognition on GDXRay castings dataset by introducing GenAI synthetic training data*. Ndt & E International, 2025, 151. https://www.doi.org/10.1016/j.ndteint.2024.103303.
6. Ma, M.L., et al., *Nondestructive classification of internal defects in camellia seeds and chestnuts using X-ray imaging: optimization and comparison of deep learning classifiers*. Food Control, 2025, 176. https://www.doi.org/10.1016/j.foodcont.2025.111367.
7. 7. Wilson, F., et al., *An Analysis of Input Parameters for Film-Based Flash X-Ray Radiography*. Experimental Techniques, 2025. https://www.doi.org/10.1007/s40799-025-00836-y.
8. Sun, S.L., et al., *Tibia-YOLO: An Assisted Detection System Combined with Industrial CT Equipment for Leg Diseases in Broilers*. Applied Sciences-Basel, 2024, 14(3). https://www.doi.org/10.3390/app14031005.
9. Zhang, H.X., et al., *Industrial digital radiographic image denoising based on improved KBNet*. Journal of X-Ray Science and Technology, 2024, 32(6): 1521-1534. https://www.doi.org/10.3233/xst-240125.
10. Son, J. and J. Park, *Recent Trends in Computed Tomography(CT) in Industry*. Journal of the Korean Society for Nondestructive Testing, 2023, 43(5): 417-430. https://www.doi.org/10.7779/jksnt.2023.43.5.417.
11. Wang, Z.B., et al., *Underwater Image Enhancement via Adaptive Color Correction and Stationary Wavelet Detail Enhancement*. Ieee Access, 2024, 12: 11066-11082. https://www.doi.org/10.1109/access.2024.3354169.
12. Zhang, X.Y., et al. *A Wavelet-based Diffusion Model for Low-light Image Enhancement in Raw Space*. in *16th International Conference on Graphics and Image Processing-ICGIP-Annual*. 2024. Nanjing University of Science and Technology School of Computer Science an, Nanjing, PEOPLES R CHINA. https://www.doi.org/10.1117/12.3057717.
13. Ai, X., G.X. Ni, and T.Y. Zeng, *A sharpening median filter for Cauchy noise with wavelet based regularization*. Journal of Computational and Applied Mathematics, 2025, 467. https://www.doi.org/10.1016/j.cam.2025.116625.
14. Zhang, F.F., et al., *Brightness segmentation-based plateau histogram equalization algorithm for displaying high dynamic range infrared images*. Infrared Physics & Technology 2023. 134. https://www.doi.org/10.1016/j.infrared.2023.104894.
15. Kong, T.R., W.P. Rey and M. Assoc Computing. *Self-supervised Low-light Image Enhancement Based on Retinex and Histogram Equalization Prior*. in *1st International Conference on Image Processing Machine Learning and Pattern Recognition*. 2024. Guangzhou, PEOPLES R CHINA. https://www.doi.org/10.1145/3700906.3700929.
16. Du, Z.M., H.A. Li, and F.L. Han, *Dynamic Fusion for Generating High-Quality Labels in Low-Light Image Enhancement*. IEEE Signal Processing Letters, 2025, 32: 2324-2328. https://www.doi.org/10.1109/lsp.2025.3575608.
17. Xiang, Y.J. and G.S. Hu. *SFT-Net: low-light image enhancement network based on spatial feature transformation*. in *2025 International Conference on Remote Sensing, Mapping, and Image Processing-RSMIP*. 2025. Sanya, PEOPLES R CHINA. https://www.doi.org/10.1117/12.3067585.
18. Zhou, L.Q., et al., *WDFN: Wavelet-Based Decomposition-Fusion Network for Low-Light Underwater Image Enhancement*. IEEE Transactions on Geoscience and Remote Sensing, 2025. 63. https://www.doi.org/10.1109/tgrs.2025.3578662.

19. Dennison, M., et al., *Image Quality Indicator Localization Using Mask R-Cnn*. Materials Evaluation 2025. 83(3).
20. Liang, Z.H., X.Y. Wu, and W. Wu, *Latent Space Diffusion Model Digital Radiography Image Super-Resolution Enhancement Algorithm*. Laser & Optoelectronics Progress, 2025, 62(16). https://www.doi.org/10.3788/lop250503.
21. Hena, B., et al., *Towards Enhancing Automated Defect Recognition (ADR) in Digital X-ray Radiography Applications: Synthesizing Training Data through X-ray Intensity Distribution Modeling for Deep Learning Algorithms*. Information, 2024, 15(1). https://www.doi.org/10.3390/info15010016.
22. Aytekin, E.K., M. Dikmen, and Ieee. *An Approach with Effective Guided Filter and Lipschitz Constraint Based CLAHE for Improving X-Ray Image Details*. in *7th International Congress on Human-Computer Interaction, Optimization and Robotic Applications-ICHORA*, 2025, Ankara, TURKIYE. https://www.doi.org/10.1109/ichora65333.2025.11017217.
23. Azad, R., et al. *Laplacian-Former: Overcoming the Limitations of Vision Transformers in Local Texture Detection*. in *26th International Conference on Medical Image Computing and Computer-Assisted Intervention (MICCAI)*, 2023, Vancouver, CANADA. https://www.doi.org/10.1007/978-3-031-43898-1_70.
24. Pal, M., et al., *A novel parallel mammogram sharpening framework using modified Laplacian filter for lumps identification on GPU*. Innovations in Systems and Software Engineering, 2024. 20(3): p. 329-345. https://www.doi.org/10.1007/s11334-024-00562-5.
25. Sari, I.N. and W.W. Du, *Weighted Similarity-Confidence Laplacian Synthesis for High-Resolution Art Painting Completion*. Applied Sciences-Basel, 2024, 14(6). https://www.doi.org/10.3390/app14062397.
26. Lin, J.C., et al., *DdeNet: A dual-domain end-to-end network combining Pale-T ransformer and Laplacian convolution for sparse view CT reconstruction*. Biomedical Signal Processing and Control 2024. 96. https://www.doi.org/10.1016/j.bspc.2024.106593.
27. Liu, Z.B., et al., *Low-light image enhancement via multistage Laplacian feature fusion*. Journal of Electronic Imaging, 2024, 33(2). https://www.doi.org/10.1117/1.Jei.33.2.023020.
28. Yuan, S.Z., et al., *Quantum image edge detection based on Laplacian of Gaussian operator*. Quantum Information Processing 2024, 23(5). https://www.doi.org/10.1007/s11128-024-04392-z.
29. Zhao, K.H., et al., *Hyper-Laplacian Prior for Remote Sensing Image Super-Resolution*. IEEE Transactions on Geoscience and Remote Sensing, 2024. 62. https://www.doi.org/10.1109/tgrs.2024.3434998.
30. Shi, Y., et al. *Study On Industrial Computed Tomography Detection And Identification Of Inclusion Defects In Thick-Wall Polyethylene Pipe Butt Fusion Joint Within Nuclear Power Plant*. in *2024 Pressure Vessels and Piping Conference*. 2024. Bellevue, WA.
31. Iuso, D., et al., *PACS: Projection-driven with Adaptive CADs X-ray Scatter compensation for additive manufacturing inspection*. Precision Engineering-Journal of the International Societies for Precision Engineering and Nanotechnology, 2024. 90: p. 108-121. https://www.doi.org/10.1016/j.precisioneng.2024.08.006.
32. Mulyana D., et al., *Application of Gaussian Filter and Histogram Equalization for Repair x-ray Image*. Digital Zone: Jurnal Teknologi Informasi Dan Komunikasi, 2022, 13(1): 34-43. https://doi.org/10.31849/digitalzone.v13i1.9770.
33. Sun, A, et al, *Welding Image Enhancement Based on CLAHE and Guided Filter*. 2024 10th International Conference on Electrical Engineering, Control, and Robotics (EECR), Guangzhou, China, 2024: 285–290. https://doi.org/10.1109/EECR60807.2024.10607276.
34. Rajeswari, P., et al, *Denoising X-Ray Image Using Discrete Wavelet Transform and Thresholding*. In: Sivasubramanian, A., Shastry, P.N., Hong, P.C. (eds) Futuristic Communication and Network Technologies.

VICFCNT 2020. Lecture Notes in Electrical Engineering, 2022, 792, Springer, Singapore. https://doi.org/10.1007/978-981-16-4625-6_19.

35. Madmad, T., et al., *CNN-based morphological decomposition of X-ray images for details and defects contrast enhancement*. 2021 IEEE/CVF Conference on Computer Vision and Pattern Recognition Workshops (CVPRW), Nashville, TN, USA, 2021: 2170–2180. https://doi.org/10.1109/CVPRW53098.2021.00246.

This page is intentionally left blank

Implementation of Generative Artificial Intelligence in a Virtual Reality Exhibition

P.M. Winarno, Wirawan Istiono, Kristina Nurhayati & Rajendra Abhinaya

Universitas Multimedia Nusantara

ABSTRACT

Background: Exhibitions are an activity that is often attended by many companies around the world because of its benefits as a promotional event. Companies can build the image of their company and products and interact directly with buyers through an exhibition. With recent advances in technology, virtual exhibitions have begun being created as an alternative to conventional face-to-face exhibitions. This presents an opportunity to implement other technologies within these new type of exhibition, namely generative artificial intelligence.

Methods: This research involved the use of the Unity game engine to create a virtual environment resembling an exhibition space. Within this environment users can navigate their surroundings and view the products displayed at the exhibition. Generative artificial intelligence was then implemented to generate content based on the products available in the exhibition. A head mounted display and virtual reality controllers were used to view and control the application. Participants were instructed to test the application. Once done, they then filled out a user acceptance test in order to evaluate their experience of using the application and how the use of generative artificial intelligence impacted that experience.

Keywords: generative artificial intelligence, unity, virtual exhibitions, virtual reality.

Classification: DCC Code: 006.3, 006.802

Language: English

Great Britain Journals Press

LJP Copyright ID: 392954
Print ISSN: 2631-8474
Online ISSN: 2631-8482

London Journal of Engineering Research

Volume 25 | Issue 5 | Compilation 1.0

Implementation of Generative Artificial Intelligence in a Virtual Reality Exhibition

P.M. Winarno[α], Wirawan Istiono[σ], Kristina Nurhayati[ρ] & Rajendra Abhinaya[Ꞷ]

ABSTRACT

Background: Exhibitions are an activity that is often attended by many companies around the world because of its benefits as a promotional event. Companies can build the image of their company and products and interact directly with buyers through an exhibition. With recent advances in technology, virtual exhibitions have begun being created as an alternative to conventional face-to-face exhibitions. This presents an opportunity to implement other technologies within these new type of exhibition, namely generative artificial intelligence.

Methods: This research involved the use of the Unity game engine to create a virtual environment resembling an exhibition space. Within this environment users can navigate their surroundings and view the products displayed at the exhibition. Generative artificial intelligence was then implemented to generate content based on the products available in the exhibition. A head mounted display and virtual reality controllers were used to view and control the application. Participants were instructed to test the application. Once done, they then filled out a user acceptance test in order to evaluate their experience of using the application and how the use of generative artificial intelligence impacted that experience.

Results: Five participants tested and evaluated the application. The implementation of generative artificial intelligence had a positive impact on the quality of the information provided by the application. In addition, it did not impact the immersion of the experience.

Conclusions: Generative artificial intelligence can be used in a virtual exhibition setting to dynamically generate content regarding available products.

Keywords: generative artificial intelligence, unity, virtual exhibitions, virtual reality.

Author α σ Ꞷ: Department of Informatics, Universitas Multimedia Nusantara, Tangerang 15810, IDN.
ρ: Department of Communication, Universitas Multimedia Nusantara, Tangerang 15810, IDN.

I. INTRODUCTION

Exhibition activities are a promotional event that is often followed by many companies and visited by many visitors all over the world. This activity is where companies can display products and services offered directly to exhibition visitors. There have been many exhibitions that have been held and new exhibitions continue to be held until now. There are several factors behind why many companies are willing to participate in exhibitions. Exhibitions provide opportunities for companies to build and improve the image of the company and products with consumers [1]. In addition, exhibitions provide an opportunity for companies to meet and interact directly with visitors in promoting them. Visitors can also interact with the products they are interested in and ask about the products [2].

However, there are some drawbacks experienced by companies and visitors when participating in exhibition activities. For companies, participating in exhibitions is something that requires significant expenditure. Capital will need to be spent to pay for things like exhibition employee salaries, venue rental prices, exhibition stand construction, and other promotional materials [3]. All of these costs make exhibition activities one of the largest expenses in many companies' promotional strategies [4]. Large exhibitions are also often crowded and crowded, which can make the experience confusing for both companies and visitors [5]. And, visitors will be limited in which

exhibitions they can attend due to factors such as exhibition capacity, exhibition location, and exhibition operating hours.

Seeing the drawbacks of conventional exhibitions, the idea came up to build a virtual exhibition system using virtual reality technology. This system can bring a number of advantages for companies compared to conventional exhibitions. The costs spent will be cheaper [6]. This is because building stands or paying exhibition staff is no longer required. The benefits received for the costs incurred will also be valid for a longer period of time. They will not be limited to just a few days as with conventional exhibition periods. Products and services can also be updated according to company needs. In addition, a virtual exhibition can be offered throughout the world in countries that are initially difficult to reach using conventional exhibitions [6].

The use of virtual reality and artificial intelligence technology will also enhance the virtual exhibition experience with its own advantages. Virtual reality does this by allowing users to interact with the information in the application more naturally [7]. The use of virtual reality can create an experience as if the user is visiting a real exhibition. Artificial intelligence can be used to generate high-quality content [8]. This can be used to help fill the application content and provide the information that users want.

However, virtual exhibitions have their own drawbacks. Companies that participate in virtual exhibitions find it difficult to measure the effectiveness of their marketing activities. Companies also find that interaction with visitors is more difficult to do in a virtual exhibition. It was found that direct interaction and follow-up contact with visitors is not as easy as compared to conventional exhibitions. And, the experience of visitors to virtual exhibitions also depends on the quality of the technology used such as hardware or visitor bandwidth [6]. Although virtual exhibitions have several drawbacks, the creation of a virtual exhibition system will give companies and visitors additional choices in how to participate in exhibition activities. These additional choices can help facilitate participants based on their individual needs.

Similar research regarding virtual exhibitions has been carried out previously by a research paper titled "Evaluation of virtual tour in an online museum: Exhibition of Architecture of the Forbidden City" [9]. In it, a virtual tour of an online museum exhibition was constructed where users can move to pre-determined locations using movement buttons. User evaluation done in this research found that although the application was able to create a good sense of reality, the interactivity and methods of navigation in the application were found to be lacking. Another research paper titled “Efficacy of Virtual Reality in Painting Art Exhibitions Appreciation” created a virtual art gallery using virtual reality technology which was then also evaluated by user testing [10]. This research found that the use of virtual reality can be suitable for creating virtual art exhibitions. One more research paper titled “Virtual Reality Exhibition Platform” created virtual environments to represent a virtual exhibition which was done with the implementation of virtual reality [11].

However, the research papers previously mentioned are lacking in some areas. The first research paper did not implement virtual reality technologies in its virtual exhibition. There is also a difference in the type of exhibitions being made. The first research paper created a virtual museum tour whilke the second created a virtual art gallery. These are different from the type of exhbition that this reasearch paper would like to explore, namely the ones in which companies can market their products and services. The third research paper successfully created this type of exhibition. However, it did not conduct any user testing and evaluation to see the efficacy and levels of user satisfaction of the application.

As such, this research aims to design and build a virtual exhibition system which uses virtual reality and artificial intelligence technology. This research also aims to measure the level of user satisfaction towards the virtual exhibition application. This paper will first discuss a literature review regarding topics related to the

research. The methodology of the research and how it was carried out will then be laid out. The results and findings of this research will be discussed next followed by conclusions that can be taken from this research.

II. LITERATURE REVIEW

2.1. Virtual Exhibitions

Virtual exhibitions are often referred to as digital exhibitions, online exhibitions, online galleries, exhibitions in cyberspace. By using virtual exhibitions, exhibitors can develop the material presented in a broader and more lasting manner to attract the interest of exhibition visitors. In addition, the use of virtual exhibitions can save production costs, such as saving on insurance, shipping and installation costs [12]. And, virtual exhibitions can reach more people than conventional exhibitions. This is because everyone can access the information they need, as long as they have a computer or another device. Virtual exhibitions are also not limited by exhibition opening or closing times and can be available 24 hours unlike conventional exhibitions [13].

In the current era, conventional exhibitions that are usually held by museums, libraries and other cultural organizations have now begun to switch to virtual exhibitions. This is because there are many benefits that can be obtained, such as convenience and cost savings. Virtual exhibitions can also be carried out via online video, streaming, social media, or via online chat. Each virtual exhibition method has its own advantages and disadvantages [14].

2.2. Virtual Reality

Virtual reality is a technology that implements a virtual 3D environment that users can navigate and interact with [15]. The nature of virtual reality makes it different compared to other forms of digital media. Users are more involved in the virtual reality experience and can interact with information more naturally in the virtual world [7]. This is because virtual reality can provide an experience that feels more real [16]. Several different types of hardware are required to be able to use virtual reality. This includes stereoscopic displays, input devices, motion tracking hardware, and desktop/mobile platforms [17].

Virtual reality is often used by developers in various fields such as education, health and entertainment [18]. The adoption of virtual reality technology occurs because of a number of benefits obtained from its use. For example, the use of virtual reality can have a positive impact on students' ability to absorb learning materials [19]. The main advantage that virtual reality has is the freedom it gives users in the way they interact and navigate their virtual environment. This helps create a more realistic and natural experience for users [20].

2.3. Non-Player Character

A non-player character is an interactive agent that is not controlled by the user. Instead, they are controlled by the AI system in the application or system where they are implemented. The behavior and actions of a non-player character can be determined rigidly or created dynamically as the application progresses based on the design and algorithms used[21]. There are several functions that can be fulfilled using non-player characters. They can be used to teach users about features or mechanics in a game or application. They can act as allies who can help the user or enemies who will fight the user. They can also be neutral characters in virtual environments that can help contribute to atmosphere and realism [22].

A non-player character is an interactive agent that is not controlled by the user. Instead, they are controlled by the AI system in the application or system where they are implemented. The behavior and actions of a non-player character can be determined rigidly or created dynamically as the application progresses based on the design and algorithms used[21]. There are several functions that can be fulfilled using non-player characters. They can be used to teach users about features or mechanics in a game or application. They can act as allies who can help the user or enemies who will fight the user. They can also be neutral characters in virtual environments that can help contribute to atmosphere and realism [22].

One popular way that is often used to control non-player characters is to use finite state machines [23]. In a finite state machine, non-player characters will have several predetermined actions or behaviors that are represented as a state. The non-player character will then transition from one state to another when an input is received or a condition is met. Another way to implement non-player characters is to use behavior trees. A behavior tree consists of nodes that are connected in one direction to each other. Behavior trees start their execution from the root node which acts as the first node. After that there are several different nodes that can be used to model the desired behavior such as fallback, sequence, parallel, decorator, action, and condition nodes [24].

2.4. Generative Artificial Intelligence

Generative artificial intelligence refers to artificial intelligence systems that have the ability to create new pieces of media through the use of generative models [25]. Generative artificial intelligence is a section of AI that has been gaining widespread use over recent years. One example of its use is the implementation of generative artificial intelligence in natural language processing. With this generative artificial intelligence can be used to process, interpret, as well as generate text [26]. Another way generative artificial intelligence is commonly used is in the creation of images. Text-to image generative models have made it possible to create images by entering a text prompt describing what image should be generated [27].

There are many different types of generative artificial intelligence that have been developed. One popular example of these different types are generative adversarial networks. Generative adversarial networks involve two competing neural networks, a generator and a discriminator. The generator is used to generate new samples while the discriminator judge samples to determine whether they are real or fake. These networks compete with each other in order to keep improving the samples generated by the generator until eventually it can no longer be distinguished from real samples by the discriminator [28].

III. METHOD

In this research, virtual reality and artificial intelligence technologies were used to create a virtual exhibition application. The initial stage in creating this application was conducting a literature review to gather information on subjects related to the study. Virtual reality, non-player characters, virtual exhibitions, and generative artificial intelligence were among the subjects covered in the literature review. The information gathered was then utilized to guide the research.

Flowcharts were then used to design the application. The primary purpose of flowcharts was to define the functionality of the application and its features, as well as the methods in which users would interact with them. The application was designed with the use of six flowcharts. These include flowcharts for the main application, main gate, choice category, car search, non-player character, and chatbot features within the application.

The main application flowchart explains the flow the application operates and how the user will interact with the application. It describes which features of the application that the user can engage with and in what sequence including the main gate, choose category and car search features. The main application flowchart can be seen in figure 1.

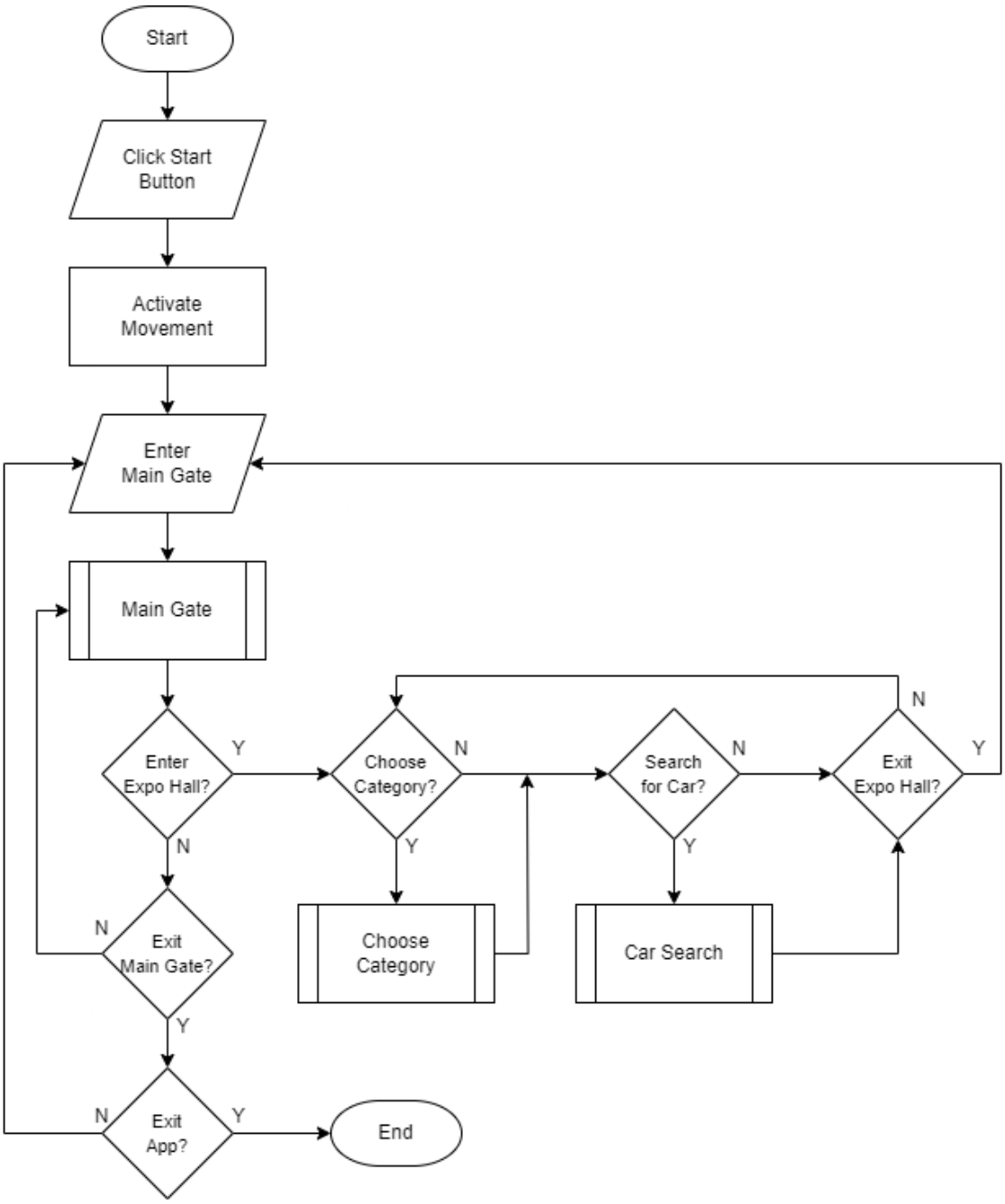

Figure 1: Main Application Flowchart

What the user can accomplish in the application's main gate area is explained in the main gate flowchart. The primary function of the main gate is to allow visitors to select the exhibition they wish to view. Following the selection of an exhibition, the application will determine whether or not it is open for visits. The credits section is an additional part of the main gate where list of all the resources used to create the application is displayed for users to view. Figure 2 shows the flowchart for the main gate.

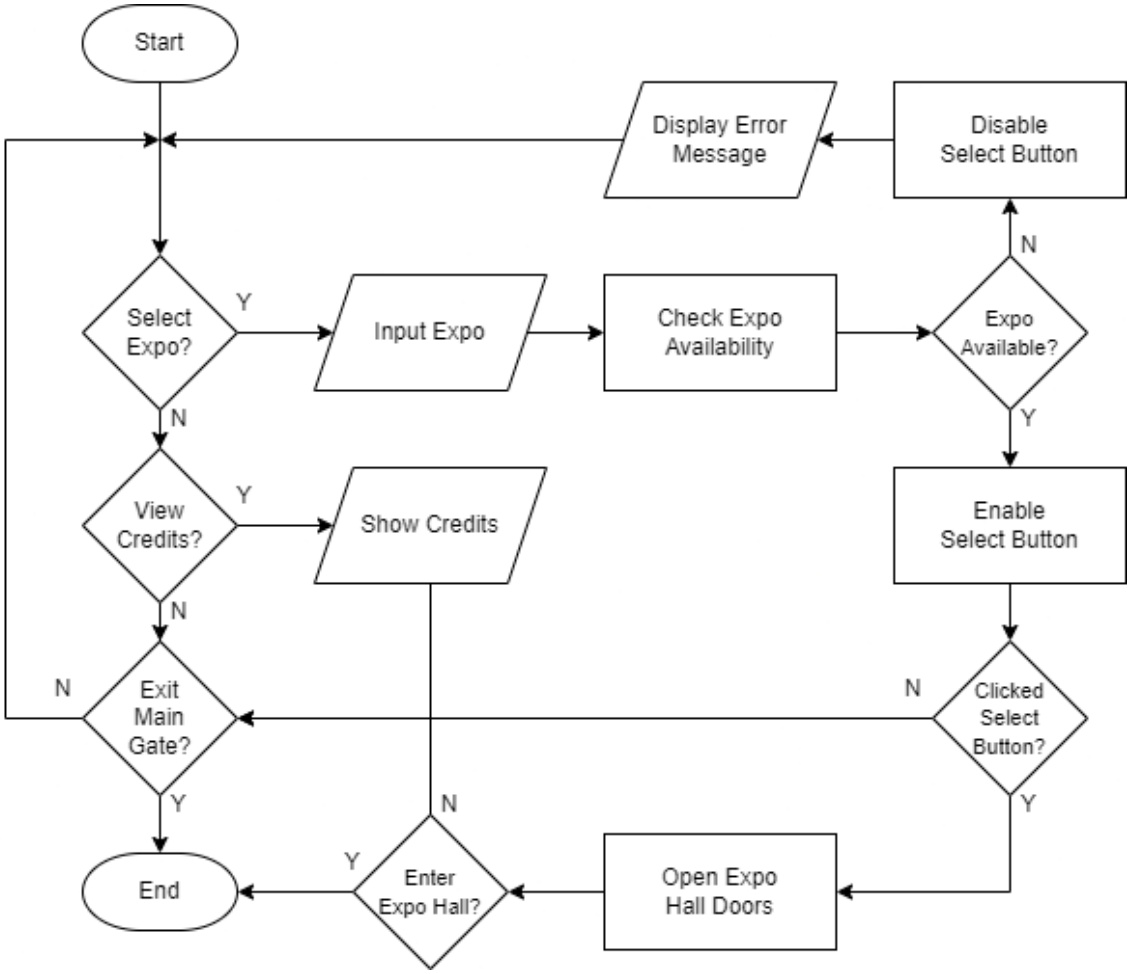

Figure 2: Main Gate Flowchart

For the category selection function, the choose category flowchart was created. Users can alter the products on display in the exhibition hall here. There will be a variety of products linked to each category, which in this case are countries. The exhibition hall will use the display stands to showcase its items after a category has been chosen. Depending on how many display stands there are at the show, the products in a category will be divided into separate halls. For instance, a category with 13 products will be divided into two halls: one for the first eight products and another for the last five. After then, users can switch between the halls in a category by pressing the previous and next buttons. The choose category flowchart can be seen in figure 3.

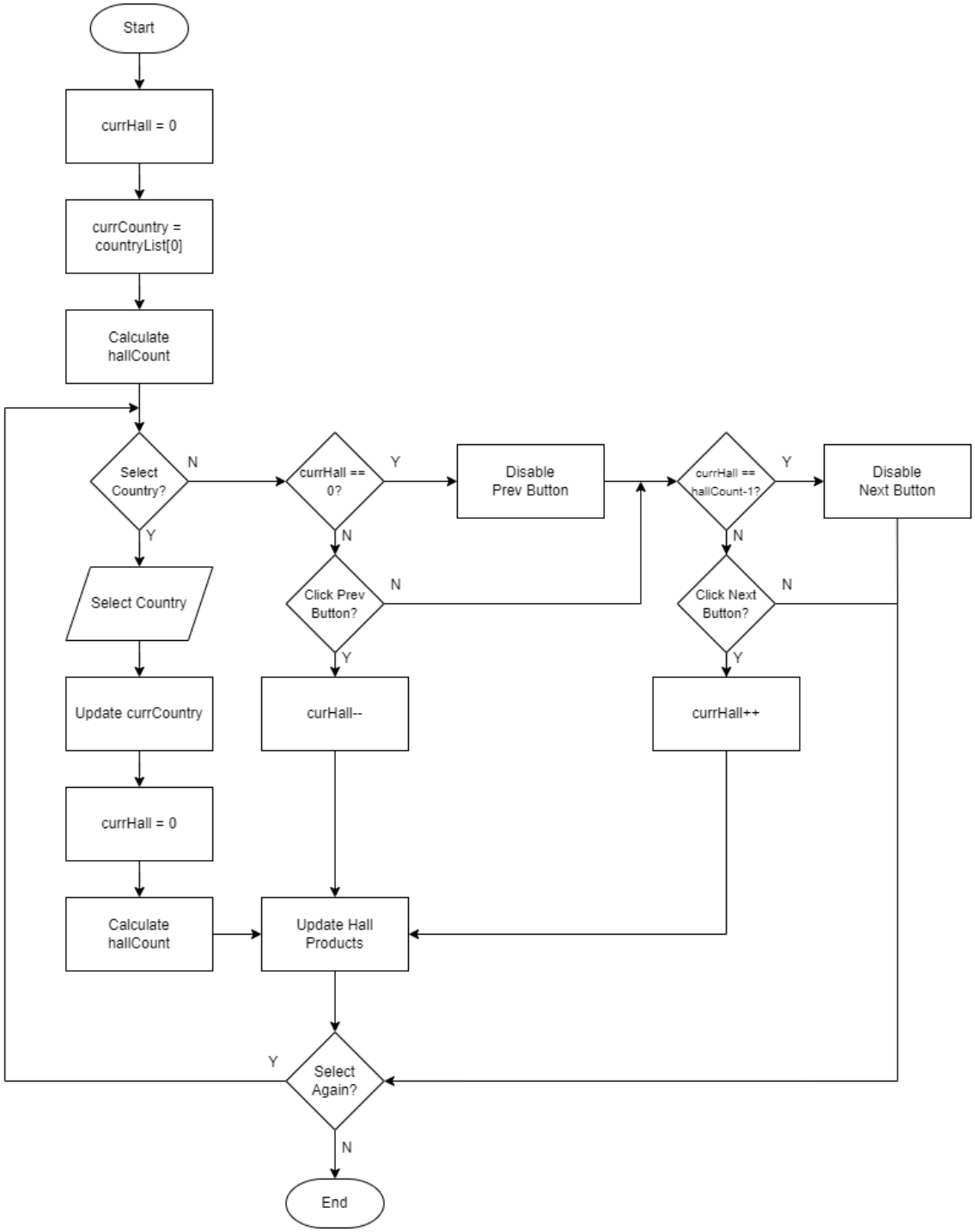

Figure 3: Choose Category Flowchart

The car search flowchart was used to design how players can search for a specific product within the application. Users can use two distinct dropdown lists to look for a specific product. The brand to which the product belongs is chosen from the first list. Selecting a brand from this list will change the second dropdown list's contents to include all of the chosen brand's products. After that, users can view the product by choosing it from the second selection. Figure 4 shows the flowchart for the car search.

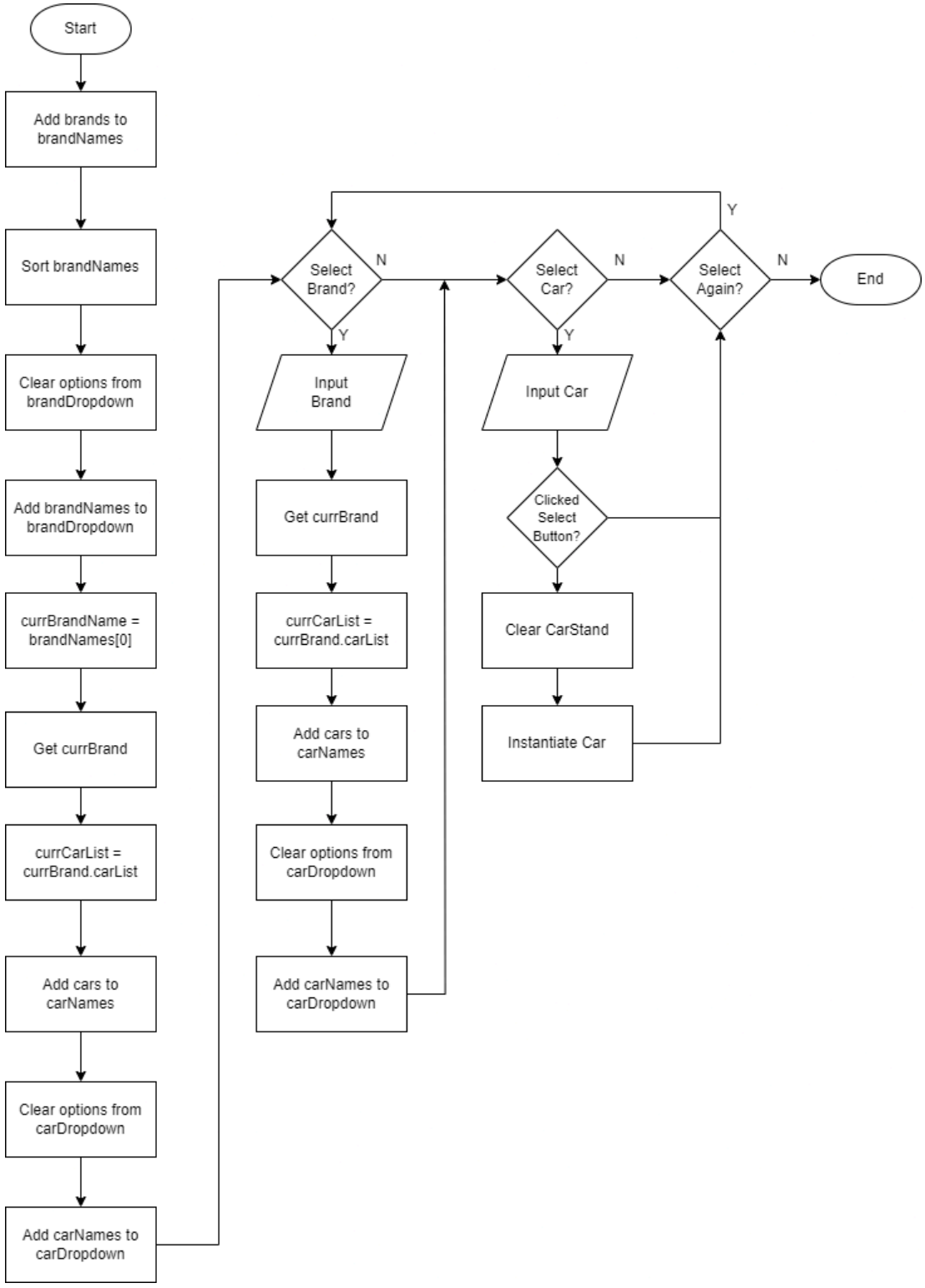

Figure 4: Car Search Flowchart

The purpose of the non-player character flowchart was to map out how non-player characters would behave within the application. It primarily relates to how they move through the virtual environment. The virtual environment contains pre-established checkpoints within it. After selecting one of these waypoints at random, the non-player character can begin moving in its direction. The non-player character's distance from its goal will be continuously measured. The non-player character will select a new one at random after reaching its destination if the distance is low enough. Figure 5 shows the flowchart for the non-player character.

Figure 5: Non-Player Character Flowchart

The Gemini API flowchart was made to represent how the Google Gemini API will be used in the application. The application will first receive a prompt from the user. The response text is then changed to "Running Chat Request" to inform the user that their prompt is being processed. An API call is made using the prompt and the application will wait for the result of the API call. The response string variable is also created with an empty value. The application will then check whether the result of the API call was successful or not. If the API call was successful, the response variable is assigned the value of the API call result. If the API call was unsuccessful, the response variable is assigned the value "An error occurred.". The response text is then replaced with the value of the response variable. The flowchart can be seen in figure 6.

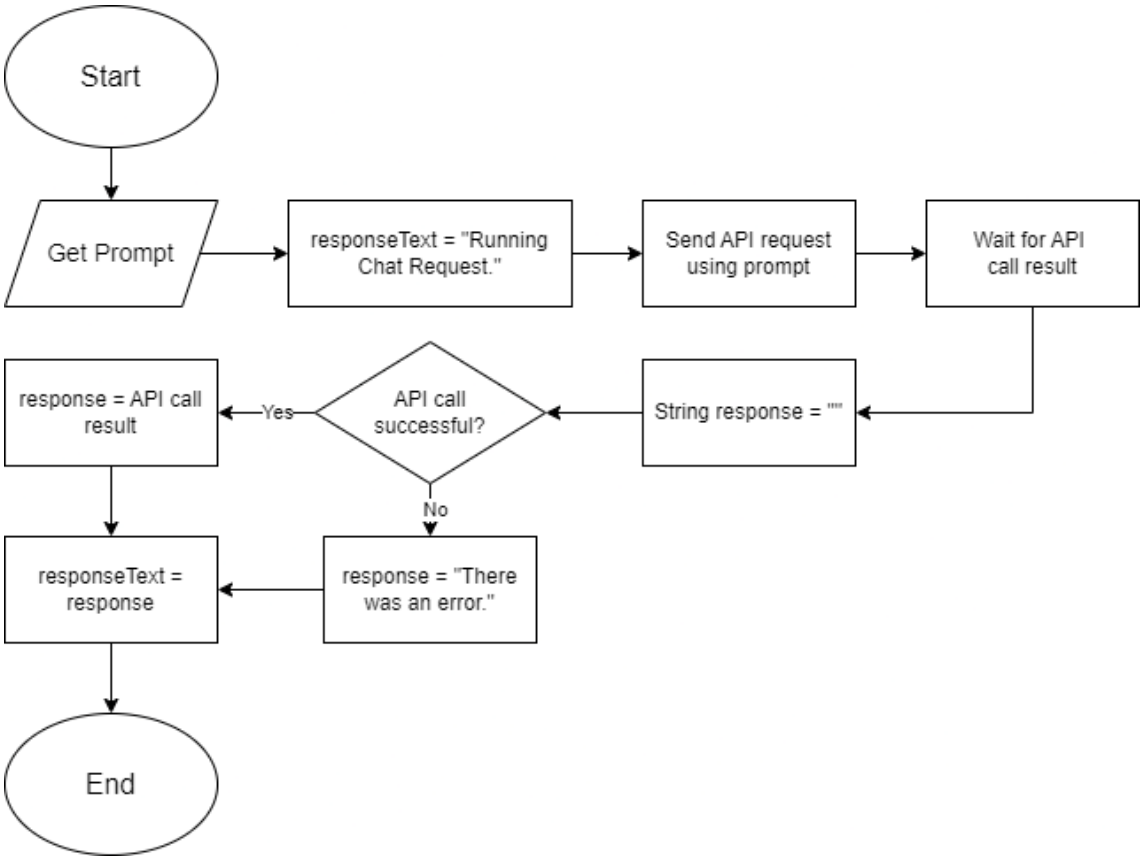

Figure 6: Gemini API Flowchart

Application development was later carried out using the Unity game engine. Development involves implementing the designs that have been made. Various Unity packages were used in the making of the application. The Unity XR Toolkit package was used to create the movement system allowing players to walk, turn and teleport. It was also used to create the interaction system which allowed players to interact with objects and UI using the virtual reality controllers. Other packages such as Probuilder and Terrain Tools were used to create the virtual environment of the application.

The application that was developed took the form of a 3D virtual environment. Users can navigate this virtual space and interact with the objects within it. The application required the use of virtual reality hardware in order to be used. The Oculus Rift headset and controllers were used for development and testing purposes in this research. The virtual reality headset was used in order to display the application to users and to rotate the in-game first-person camera. The

controllers on the other hand were used by users to navigate and move around in the virtual environment of the application.

Evaluation was carried out by having users try the application directly using virtual reality hardware such as headsets and controllers. A brief explanation was be given regarding the application and how to use the hardware. Users will then use the application and try all the features on it. Documentation of the testing process carried out by users can be seen in figure 6. After users have finished trying the application, they will fill out a questionnaire to provide their level of satisfaction with the application. Testing and evaluation was carried out by a total of 5 users.

IV. RESULTS AND DISCUSSION

4.1. Development Results

This research has succeeded in building a virtual exhibition system using virtual technology. Application development was carried out using the Unity game engine. The application created has several main features, namely a movement and interaction system, exhibition features, an audio system, and non-player characters.

The movement and interaction system is how users can interact with the virtual world that has been created in the application. The movement system in the application is what allows users to traverse the virtual environment. Meanwhile, the interaction system facilitates users in interacting, influencing and obtaining information from the application. Because the application is built based on virtual reality technology, users will use a special controller as the main way to enter input into the application.

There are several different methods that can be used to move within the application. The left-hand controller functions to move forwards and backwards. To rotate left and right, users can use the right-hand controller or the virtual reality headset. Apart from that, the right-hand controller can also be used to teleport where users can adjust their position and rotation instantly. Figure 7 shows the use of the teleportation system in the application.

Figure 7: The Teleportation Feature

There are also several ways in which users can interact with objects in the application. Interaction is mainly carried out using the left and right controllers which act as the user's hands. The desired interaction with an object can be done directly, such as holding the object in a user's hand. Users can also use a ray coming out of their hands to interact with objects and the UI. This can be seen in Figure 8. Interaction with objects uses the grip button on the controller while interaction with the UI uses trigger button.

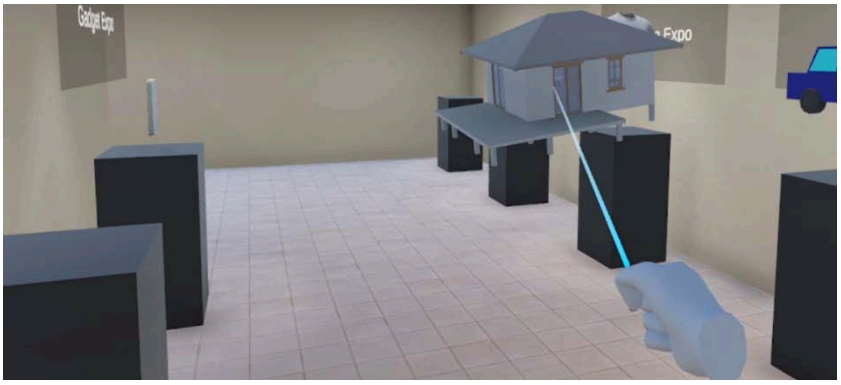

Figure 8: Interacting with Objects using a Ray

The exhibition features discussed are features that can be used by users in virtual exhibitions on the application. The features created are the result of implementing the designs produced at the design stage. They cover how a user can use the application as a virtual exhibition. Included in this is how users can select the exhibition they want, view the desired product, and view information about a product.

The exhibition selection feature is a way for users to select the exhibitions they want to visit. This is done at the main gate section of the exhibition building. The selection is made by taking an object that represents an exhibition and placing it on the selection table. If the selected exhibition can be visited then the button next to the entrance will turn green. If the exhibition cannot be visited then the button will turn red and an error message will appear once the button is pressed. This can be seen in Figure 9. Only the car exhibition can be visited at this time.

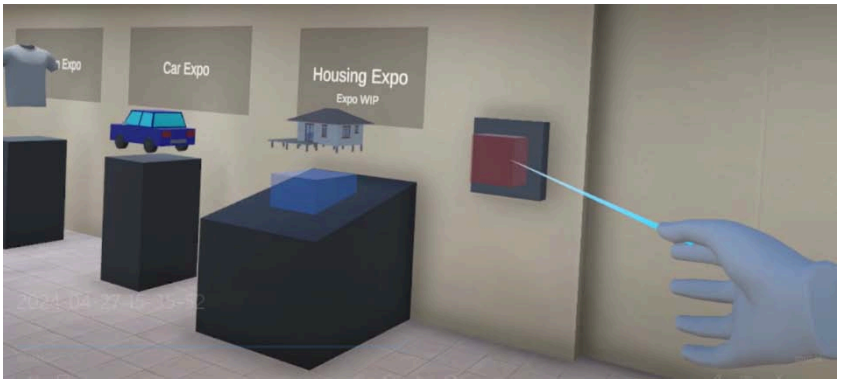

Figure 9: Choosing an Exhibition that is Not Available

The product selection feature is how users can search for the products they want at the exhibition. Users can do this by changing the contents of the exhibition space. The products at the exhibition are divided into several categories that users can choose from. Each category will then have several rooms that can be selected to change the contents of the exhibition space. In the car exhibition, the cars are divided based on their country of origin. After selecting a category, users can select the room or hall they want to view. With this, the contents of the exhibition room will change to show the cars in the selected hall. The category selection table can be seen in figure 10.

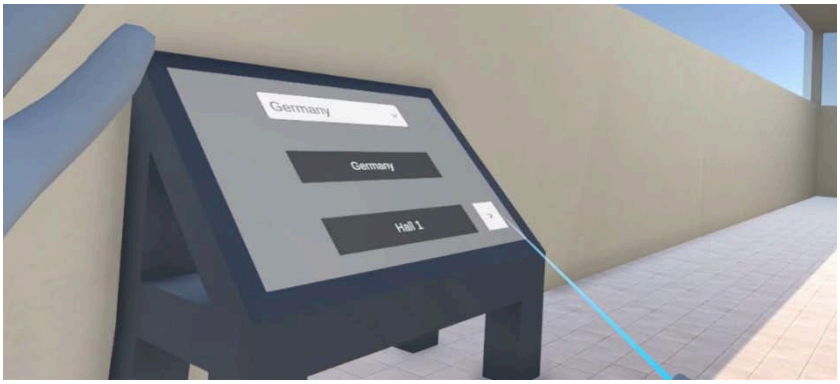

Figure 10: Category Selection Table

Selection can also be done individually with the product search feature which can be seen in figure 11. With this, users can search for products more specifically. In the car exhibition, the search feature functions by using a dropdown list containing all car brands in the application. Users can then select a desired brand. This action will add all products from that brand to the second dropdown list. Users can then select the products they want from the second dropdown list to make them appear.

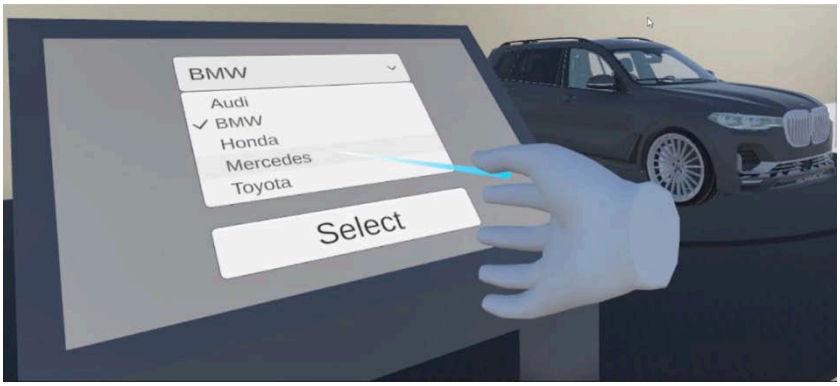

Figure 11: Product Search Feature

Then there is the feature in the exhibition that function to provide information about a product. This feature facilitates users in finding information about the products they are interested in. At the car exhibition, information about a car is shown on a screen on the stand occupied by the car. The screen shows information about the car such as its name, dimensions, price, etc. Users can press buttons at the bottom of the panel to change the information displayed. The information screen display can be seen in figure 12.

Figure 12: Product Information Feature

An audio system was developed in the application to make the application produce sound when used. The sound in the application comes from objects in the environment. Sounds can be played when the user interacts with an object. For example, there will be a sound when the user picks up and releases an object. There are also sounds that play continuously such as the music in an exhibition hall.

The application uses two different types of audio, namely 2D audio and 3D audio. 2D audio is audio that is always played at the same volume. An example of using 2D audio in an application is for UI such as buttons and dropdown lists. 3D audio is audio that is played at a dynamic volume. The volume of 3D audio depends on the distance between the sound source and the user's position in the environment. 3D audio is used for things like the music in the exhibition hall and the sound of footsteps belonging to non-player characters.

The non-player character or NPC feature in the application refers to characters who are controlled by the user. These characters are controlled by the application that will give instructions to regulate their behavior. With this, the movements of non-player characters are carried out independently without input from the user. Non-player characters are used in the app as a way to simulate the presence of other visitors at the exhibition.

Navigation by non-player characters is carried out using the AI navigation system provided by Unity. In this system, a NavMesh is used to mark areas that can be traveled by non-player characters. The shape of NavMesh can be modified using other components such as NavMeshObstacle and NavMeshVolumeModifier. The non-player character can then plan a path to a destination located in the NavMesh. Several destination points are spread across the exhibition room and are chosen by non-player characters at random. All this can be seen in figure 13 where the blue area is the NavMesh and the yellow dots are the destination points. Once selected, the non-player character will start walking towards that point. A new point will then be selected once the non-player character successfully reaches their destination.

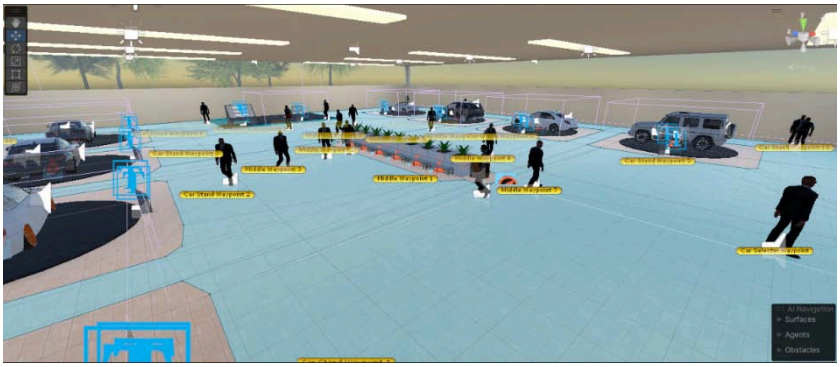

Figure 13: Navigation System for Non-Player Characters

In addition, there are other non-playable characters in the form of guards and salespeople. These non-playable characters serve to provide the users with information. The guard characters' function is to provide the user with information regarding the application. There are two guards within the application. The first guard is located in the main gate room. Users can ask the first guard questions about how to use the application such as how to interact with objects or teleport. The second guard is located in the exhibition room. Users can ask the second guard questions about exhibition features such as the car search feature or interaction with cars. Then there are the salespeople non-playable characters. The salesperson character is located at each car stand that has a product on display. The salesperson is used to ask questions about the cars on the stand. The salesperson starts with the user making a selection using the grip button on their controller. The salesperson will then check if the user also presses the trigger button while the grip button is being held to activate. If not, the salesperson will run the text to speech feature. If the trigger button

is also pressed, the salesperson will display the chat panel if it is not already displayed and close it if it is already displayed. In the chat panel, the user can use the AI Chatbot feature to ask the salesperson questions about the cars displayed on the stand. Figure 14 shows a salesperson character within the application.

In addition, there are other non-playable characters in the form of guards and salespeople. These non-playable characters serve to provide the users with information. The guard characters' function is to provide the user with information regarding the application. There are two guards within the application. The first guard is located in the main gate room. Users can ask the first guard questions about how to use the application such as how to interact with objects or teleport. The second guard is located in the exhibition room. Users can ask the second guard questions about exhibition features such as the car search feature or interaction with cars. Then there are the salespeople non-playable characters. The salesperson character is located at each car stand that has a product on display. The salesperson is used to ask questions about the cars on the stand. The salesperson starts with the user making a selection using the grip button on their controller. The salesperson will then check if the user also presses the trigger button while the grip button is being held to activate. If not, the salesperson will run the text to speech feature. If the trigger button is also pressed, the salesperson will display the chat panel if it is not already displayed and close it if it is already displayed. In the chat panel, the user can use the AI Chatbot feature to ask the salesperson questions about the cars displayed on the stand. Figure 14 shows a salesperson character within the application.

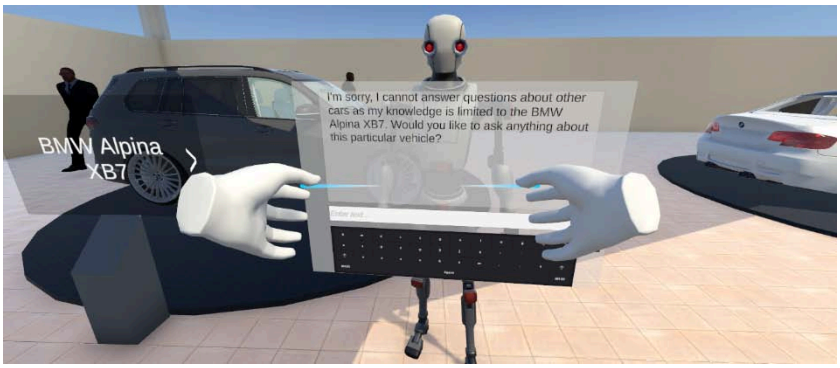

Figure 14: Salesperson Non-Playable Character

An AI Chatbot feature is developed using the Google Gemini API. The resulting AI Chatbot is a table where users can type the desired prompt and get an answer based on what is entered. The AI Chatbot display can be seen in Figure 15. To enter a prompt, the user first needs to select the input column using the virtual reality controller being used. After that, the user can type the desired prompt using the virtual keyboard provided on the AI Chatbot. When the user presses the Enter key, the typed prompt will be sent to the Google Gemini API. Google Gemini will then generate a response using the prompt provided by the user. This response will be sent back to the application and displayed by the AI Chatbot table.

The Google Gemini API is also used to display information about the cars at the exhibition. Each car is stored in the application as a scriptable object. This scriptable object contains data about a car such as the name, make and 3D model of the car. This data is used to send a prompt about the car to the Google Gemini API. The application will prompt about the description and features for each car. The text generated by Google Gemini will then be displayed on each car stand.

Figure 15: AI Chatbot Feature

4.2. Analysis of Evaluation Results

Evaluation results from the questionairre that was filled out by users were analised by calculating the mean values. The mean of the answers given by users is calculated by dividing the total score of all answers by the number of answers. To calculate the total score for an answer, all the values given by users will be added up based on their respective value weights. The final score is then calculated by adding up the means of each answer and dividing it by the number of answers in the questionnaire. The results of the user evaluation can be seen in table 1.

The total score is calculated using the following formula:

$$TotalScore = (answer1Amount * 1) + (answer2Amount * 2) + (answer3Amount * 3) + (answer4Amount * 4) + (answer5Amount * 5)$$

The mean is calculated using the following formula:

$$Mean = \frac{Total\ Score}{Number\ of\ Respondents}$$

The final score is calculated using the following formula:

$$Final\ Score = \frac{\Sigma Mean}{Number\ of\ Questions}$$

Table 1: User Evaluation Results

Questions	Number of Responses					Mean
	1	2	3	4	5	
Is the visual quality of the application good?	0	0	0	2	3	88%
Is the quality of the movement system in the application good?	0	0	0	1	4	96%
Are the interactions with objects and UI in the application good?	0	0	1	3	1	80%
Is the audio quality of the application good?	0	0	1	3	1	88%
Is the quality of the content in the application good?	0	0	0	0	5	100%
Is the information provided on products informative?	0	0	0	0	5	100%
Is the application intuitive and easy to use?	0	0	1	2	2	84%
Is the experience of using the application immersive?	0	0	0	2	3	92%
As a whole, are you satisfied with the application?	0	0	0	1	4	96%
Final Score						91.6%

With this, it can be interpreted that the virtual exhibition that was made had been received well by those who tried it. This is supported by a high final score of 91.6%. Users gave the highest score to the quality of the content and product information in the application with an average score of 100%. Meanwhile, the lowest score was given to the audio quality and user interaction with the objects and UI in the application. It can be concluded that the quality of the content in the form of exhibition products and the implementation of the Google Gemini API to display product information is quite good. However, the quality of the interaction system, UI display, and audio can still be improved.

The results of this research differes from those of the virtual museum tour that had been previously discussed. The application that has been made performs better in terms of interactivity and immersion. This could come down to the less restricitve methods of navigation used as well as the use of virtual reality technology. With these results it can be said that this research has done well in creating a well-functioning virtual exhibition application which implements virtual reality technology and in measuring user satisfaction towards the application. The study is limited however in the users that were collected for evaluation purposes. Only 5 users were able to be found for this research. And, there is a lack of diversity in the types of users with them all being university students within the same age group.

This research aimed to design and build a virtual exhibition system using virtual reality and artificial intelligence technology and to measure the level of user satisfaction towards the virtual exhibition application. With the carrying out of this research, user sentiments towards attending virtual exhibitions using virtual reality and artificial intelligence can be examined. Judging by the results, it would appear that users are open and willing to the idea. There are still questions to be held about the viability of hosting virtual exhibitions in this manner as this research only focused on the visitor side of things. How companies and brands feel about participating in these virtual exhibitions and whether the exhibitions can perform as well as conventional exhibitions still remain unanswered.

V. CONCLUSION

This research has been successful in designing building a virtual exhibition system using virtual reality and artificial intelligence technology. After testing with 5 users using the user acceptance test method and Likert scale, the user satisfaction level was found to be 91.6%, which shows that users are very satisfied with the application that was built. Based on this value, it can be interpreted that users generally accept that the system has been created well. These results support the feasibility of using the virtual exhibition system based on virtual reality technology that has been produced. This provides justification to any interested in carrying out such exhibitions. The virtual exhibition that was produced also performed better in terms of immersion and navigation compared to other exhibitions which do not use virtual reality and artificial intelligence. This suggests that the implementation of virtual reality technologies played a role in enhancing the user experience and that it could perhaps be applied to enhance other virtual experiences. To further test the viability of virtual exhibitions using virtual reality, more research can be done regarding their performance for the businesses who decide to take part in them.This research has been successful in designing building a virtual exhibition system using virtual reality and artificial intelligence technology. After testing with 5 users using the user acceptance test method and Likert scale, the user satisfaction level was found to be 91.6%, which shows that users are very satisfied with the application that was built. Based on this value, it can be interpreted that users generally accept that the system has been created well. These results support the feasibility of using the virtual exhibition system based on virtual reality technology that has been produced. This provides justification to any interested in carrying out such exhibitions. The virtual exhibition that was produced also performed better in terms of immersion and navigation compared to other exhibitions which do not use virtual reality and

artificial intelligence. This suggests that the implementation of virtual reality technologies played a role in enhancing the user experience and that it could perhaps be applied to enhance other virtual experiences. To further test the viability of virtual exhibitions using virtual reality, more research can be done regarding their performance for the businesses who decide to take part in them.

ACKNOWLEDGEMENTS

This research was made possible by the funding and support provided by Universitas Multimedia Nusantara.

REFERENCES

1. K. Hansen, "Measuring performance at trade shows: Scale development and validation," *J Bus Res*, vol. 57, no. 1, pp. 1–13, Jan. 2004, doi: 10.1016/S0148-2963(02)00269-2.
2. C. M. Sashi and J. Perretty, "Do trade shows provide value?," *Industrial Marketing Management*, vol. 21, no. 3, pp. 249–255, Aug. 1992, doi: 10.1016/0019-8501(92)90022-L.
3. S. McCoy and P. J. du Plessis, "The Role of Exhibitions in the Marketing Mix in South Africa SMcCoy Strategy and Business Development," *SAJEMS NS*, vol. 3, no. 3, 2000, doi: 10.10520/AJA10158812_286.
4. A. Shoham, "Selecting and evaluating trade shows," *Industrial Marketing Management*, vol. 21, no. 4, pp. 335–341, Nov. 1992, doi: 10.1016/0019-8501(92)90044-T.
5. P. Herbig, B. O'Hara, and F. Palumbo, "Measuring trade show effectiveness: An effective exercise?," *Industrial Marketing Management*, vol. 23, no. 2, pp. 165–170, Apr. 1994, doi: 10.1016/0019-8501(94)90018-3.
6. U. Gottlieb and C. Bianchi, "Virtual trade shows: Exhibitors' perspectives on virtual marketing capability requirements," *Electron Commer Res Appl*, vol. 21, pp. 17–26, Jan. 2017, doi: 10.1016/J.ELERAP.2016.12.004.
7. Bricken Meredith, "Virtual reality learning environments: potentials and challenges," *ACM SIGGRAPH Computer Graphics*, vol. 25, no. 3, pp. 178–184, Jul. 1991, doi: 10.1145/126640.126657.
8. J. Kim, S. Shin, K. Bae, S. Oh, E. Park, and A. P. del Pobil, "Can AI be a content generator? Effects of content generators and information delivery methods on the psychology of content consumers," *Telematics and Informatics*, vol. 55, p. 101452, Dec. 2020, doi: 10.1016/J.TELE.2020.101452.
9. J. Li, J. W. Nie, and J. Ye, "Evaluation of virtual tour in an online museum: Exhibition of Architecture of the Forbidden City," *PLoS One*, vol. 17, no. 1 January, 2022, doi: 10.1371/journal.pone.0261607.
10. C. L. Lin, S. J. Chen, and R. Lin, "Efficacy of Virtual Reality in Painting Art Exhibitions Appreciation," *Applied Sciences 2020, Vol. 10, Page 3012*, vol. 10, no. 9, p. 3012, Apr. 2020, doi: 10.3390/APP10093012.
11. G. Calin Deac, C. Narcisa Georgescu, and C. Laurentiu Popa, "Virtual Reality Exhibition Platform," pp. 232–0236, 2018, doi: 10.2507/29th.daaam.proceedings.033.
12. C. K. Ramaiah, "Trends in online exhibitions," *DESIDOC Journal of Library and Information Technology*, vol. 34, no. 2, pp. 83–86, 2014, doi: 10.14429/DJLIT.34.6757.
13. S. Foo, "Online Virtual Exhibitions: Concepts and Design Considerations," *DESIDOC Journal of Library & Information Technology*, vol. 28, no. 4, pp. 22–34, Jul. 2008, doi: 10.14429/DJLIT.28.4.194.
14. L. C. Khoon and C. K. Ramaiah, "An Overview of Online Exhibitions," *DESIDOC Journal of Library & Information Technology*, vol. 28, no. 4, pp. 7–21, Jul. 2008, doi: 10.14429/DJLIT.28.4.193.
15. D. A. Guttentag, "Virtual reality: Applications and implications for tourism," *Tour Manag*, vol. 31, no. 5, 2010, doi: 10.1016/j.tourman.2009.07.003.
16. J. Sampoerna, J. Sampoerna, W. Istiono, and A. Suryadibrata, *Virtual Reality Game for Introducing Pencak Silat*, vol. 14, no. 15. International Association of Online Engineering, 2021. doi: 10.3991/ijim.v15i01.17679.
17. T. Parisi, "Learning virtual reality : developing immersive experiences and applications for

desktop, web, and mobile," 2015, Accessed: Mar. 04, 2024. [Online]. Available: https://www.oreilly.com/library/view/learning-virtual-reality/9781491922828/
18. B. L. Ludlow, "Virtual Reality: Emerging Applications and Future Directions," *Rural Special Education Quarterly*, vol. 34, no. 3, 2015, doi: 10.1177/875687051503400302.
19. D. Checa and A. Bustillo, "Advantages and limits of virtual reality in learning processes: Briviesca in the fifteenth century," *Virtual Real*, vol. 24, no. 1, pp. 151–161, Mar. 2020, doi: 10.1007/S10055-019-00389-7/METRICS.
20. M. El Beheiry, S. Doutreligne, C. Caporal, C. Ostertag, M. Dahan, and J. B. Masson, "Virtual Reality: Beyond Visualization," 2019. doi: 10.1016/j.jmb.2019.01.033.
21. G. A. da Silva and M. W. de Souza Ribeiro, "Development of Non-Player Character with Believable Behavior: a systematic literature review," 2022. doi: 10.5753/sbgames_estendido.2021.19660.
22. D. C. Brogan, R. A. Metoyer, and J. K. Hodgins, "Dynamically simulated characters in virtual environments," *IEEE Comput Graph Appl*, vol. 18, no. 5, 1998, doi: 10.1109/38.708561.
23. D. Jagdale, "Finite State Machine in Game Development," *International Journal of Advanced Research in Science, Communication and Technology*, 2021, doi: 10.48175/ijarsct-2062.
24. M. Colledanchise, R. Parasuraman, and P. Ögren, "Learning of behavior trees for autonomous agents," *IEEE Trans Games*, vol. 11, no. 2, 2019, doi: 10.1109/TG.2018.2816806.
25. S. S. Sengar, A. Bin Hasan, S. Kumar, and F. Carroll, "Generative artificial intelligence: a systematic review and applications," *Multimed Tools Appl*, 2024, doi: 10.1007/s11042-024-20016-1.
26. M. Jovanovic and M. Campbell, "Generative Artificial Intelligence: Trends and Prospects," *Computer (Long Beach Calif)*, vol. 55, pp. 107–112, Oct. 2022, doi: 10.1109/MC.2022.3192720.
27. H. Vartiainen and M. Tedre, "Using artificial intelligence in craft education: crafting with text-to-image generative models," *Digital Creativity*, vol. 34, pp. 1–21, 2023, doi: 10.1080/14626268.2023.2174557.
28. I. Goodfellow *et al.*, "Generative adversarial networks," *Commun ACM*, vol. 63, no. 11, 2020, doi: 10.1145/3422622.

Great Britain Journal Press Membership

For Authors, subscribers, Boards and organizations

Great Britain Journals Press membership is an elite community of scholars, researchers, scientists, professionals and institutions associated with all the major disciplines. Great Britain memberships are for individuals, research institutions, and universities. Authors, subscribers, Editorial Board members, Advisory Board members, and organizations are all part of member network.

Read more and apply for membership here:
https://journalspress.com/journals/membership

Author Membership provide access to scientific innovation, next generation tools, access to conferences/seminars/ symposiums/webinars, networking opportunities, and privileged benefits. Authors may submit research manuscript or paper without being an existing member of GBJP. Once a non-member author submits a research paper he/she becomes a part of "Provisional Author Membership".

Society flourish when two institutions Come together." Organizations, research institutes, and universities can join GBJP Subscription membershipor privileged "Fellow Membership" membership facilitating researchers to publish their work with us, become peer reviewers and join us on Advisory Board.

Subscribe to distinguished STM (scientific, technical, and medical) publisher. Subscription membership is available for individuals universities and institutions (print & online). Subscribers can access journals from our libraries, published in different formats like Printed Hardcopy, Interactive PDFs, EPUBs, eBooks, indexable documents and the author managed dynamic live web page articles, LaTeX, PDFs etc.

PRINTED VERSION, INTERACTIVE PDFS, EPUBS, EBOOKS, INDEXABLE DOCUMENTS AND THE AUTHOR MANAGED DYNAMIC LIVE WEB PAGE ARTICLES, LATEX, PDFS, RESTRUCTURED TEXT, TEXTILE, HTML, DOCBOOK, MEDIAWIKI MARKUP, TWIKI MARKUP, OPML, EMACS ORG-MODE & OTHER